UNIVERSITÀ DEGLI STUDI DI PADOVA

Dipartimento di Fisica e Astronomia "Galileo Galilei"
Master Degree in Astrophysics and Cosmology

Final Dissertation

INVESTIGATING NEUTRON STARS THROUGH THEORY AND SIMULATIONS

Thesis supervisor:

Prof. Roberto Turolla

Thesis co-supervisor:

Prof. Tjonnie Guang Feng Li

Candidate:

Alessia Pascoli

Academic Year 2024/2025

ABSTRACT

The tidal deformability encodes crucial information about the internal structure and the equation of state of neutron star matter, and plays a fundamental role in the interpretation of gravitational wave signals from binary neutron star systems. This thesis investigates the tidal deformability of non-rotating, unmagnetised neutron stars under the static response approximation, employing a combined approach based on analytical modelling and numerical simulations.

The core original contribution of this thesis lies in the development of a computational framework for introducing tidal perturbations within general-relativistic hydrodynamic simulations of isolated neutron stars. The perturbation is implemented in a simplified analytical form, with the primary goal of testing and validating the numerical method. This novel approach enables the study of tidal deformations in a controlled setting, avoiding the complexities associated with full binary dynamics. To validate the scheme, a test simulation of a perturbed neutron star is performed and systematically compared to a benchmark unperturbed case. The comparative analysis reveals a quadrupolar deformation pattern in the perturbed configuration, which qualitatively matches the expected geometry of a tidally deformed object. Although the approximated representation of tidal perturbations limits immediate physical interpretability, the results confirm the validity of the proposed method and demonstrate its potential for future extensions. The computational setup developed in this project is readily adaptable to more complex scenarios, including rotation, strong intrinsic magnetic fields, and more realistic equations of state.

Contents

List of Figures

List of Tables

Chapter 1

INTRODUCTION

This thesis project investigates the tidal deformability of stationary neutron stars (NSs) without strong magnetic fields under the static response approximation, using a combined approach of theory and numerical simulations.

The way in which astrophysical compact objects react to external tidal fields carries valuable information on both their internal structure and the nature of their gravitational interactions. In a NS, the tidal deformability measures the quadrupolar response developed by the star configuration as a reaction to an external perturbing tidal field. In astrophysical contexts, this scenario is realized in binary neutron star (BNS) systems, where the tidal perturbation is generated by the gravitational field of the companion star. The induced deformation of each binary component is parametrised by the tidal deformability, which is highly sensitive to the equation of state (EOS) of NS matter. NSs are the most compact astrophysical objects endowed with a solid surface, and, despite considerable observational and theoretical progress, the characteristics and behaviour of matter at the supra-nuclear densities found in their interiors are still poorly understood. Therefore, refining the current models for the EOS of ultra-dense matter remains among the most intriguing challenges of modern nuclear physics and astrophysics. Encoding such information, the tidal deformability emerges as a key quantity, the study of which is pivotal to gain deeper insights into the internal composition of such extreme and complex compact objects as NSs.

Even though this work will not enter into the details of the gravitational wave (GW) data analysis, it is important to mention that the tidal deformability is primarily measured through GW observations of BNS coalescences. The groundbreaking detection of GW170817 has already demonstrated the potential of such measurements to place ever more stringent constraints on the NS EOS Abbott et al. (2017).
The effort in accurately modelling the tidal response of NSs in BNS systems is particularly timely given the advent of next-generation detectors, such as the Einstein Telescope, which are designed to achieve significantly greater sensitivity and a broader frequency range Sathyaprakash et al. (2012). This expanded observation window is expected to allow investigation of previously inaccessible stages of BNS evolution and dynamics.

1.1 Project positioning

The first computation of the tidal Love number for NSs in general relativity (GR) was performed by Hinderer (2008). In this work, the author derived the perturbation equations for a spherically symmetric, static star subject to an external tidal field assuming a polytropic EOS. Despite not being the most realistic description, this choice allowed exploration of a wide range of stellar models that can be reasonably approximated by a polytrope with polytropic index $n \sim 0.5 - 1.0$ Lattimer & Prakash (2007). This formalism was later extended to account for more realistic candidate EOS in Hinderer et al. (2010). Following the innovative work by Hinderer (2008), Damour & Nagar (2009) improved the analytical treatment of the problem by including additional tidal coefficients associated with a self-gravitating body. The results indicate a strong sensitivity on the compactness parameter for all three dimensionless tidal coefficients considered: one of gravito-electric type, one of gravito-magnetic type and the shape Love number h_l.

Many of the first analytical studies based on Hinderer's approach relied on a set of simplifying assumptions, such as restriction to non-rotating and unmagnetised NSs, which were addressed in later research. Pani et al. (2015) first computed the tidal Love numbers of a spinning NS to linear order in the angular momentum. Due to the spin of the object, a new class of rotational tidal Love numbers emerge, which measure the coupling between the object's angular momentum and the external tidal field. The authors showed that these spin-induced Love numbers as functions of the moment of inertia are very sensitive to the EOS and claimed that the spin-tidal coupling could introduce important corrections to the gravitational waveforms of a spinning BNS system. The role of intrinsic magnetic fields was investigated in the innovative work by Zhu et al. (2020), in which magnetically induced corrections to the tidal deformability are computed. In this work, first-order tidal perturbations are analytically treated following the same formalism as Hinderer (2008), assuming a static, spherically symmetric spacetime as the background solution. The magnetic field contribution is treated as an additional first-order perturbation as in Konno et al. (1999), where the field is assumed to be axially symmetric and purely poloidal. Then, a second-order perturbative analysis is performed to capture the coupling between tidal and magnetic effects and determine to which extent the tidal deformability is modified by the presence of an intrinsic magnetic field. Overall, the published results show that magnetically induced corrections are expected to produce detectable variations in the GW evolution of the system only for very strong magnetic fields $B \sim 10^{16}$ G.

Another limitation of many of the first studies on the tidal deformability is that they were conducted under the static response approximation. Indeed, to leading order in the orbital angular velocity of the binary, the tidal deformation induced by the companion is quantified by a set of static tidal Love numbers, the effect of which enters at fifth order in a post-Newtonian expansion (5PN). However, as the system evolves and the orbital separation shrinks, the effect of dynamical tides becomes significant. The next-to-leading conservative effect is a frequency-dependent tidal response, quantified by a set of dynamical tidal Love numbers that first appear at 8PN order in gravitational waveforms. Among the most recent publications that extensively focused on dynamical tidal effects, the work by Katagiri et al. (2024) contributed proposing the calibration of a tidal response function for any compact object in vacuum GR. This allowed for the definition of the dynamical tidal deformability of relativistic stars as the difference from the corresponding black hole (BH) values.

On the computational side, much of the numerical research on the tidal deformability focuses on waveform modelling for BNS systems. One pioneering work in this field is that of Dietrich et al. (2017), in which the authors propose the first closed-form tidal approximant combining post-Newtonian, tidal effective-one-body (EOB) and numerical relativity (NR) information. The resulting phenomenological waveform model is called `NRTidal` and was later refined by Dietrich et al. (2019a) and Dietrich et al. (2019b). In Dietrich et al. (2019b), the updated version `NRTidalv2` was released, which builds upon `NRTidal` by using more accurate NR data for calibration, adding tidal corrections to the GW signal amplitude, and incorporating spin effects. Recent work by Abac et al. (2024) further extended the existing model under the new name of `NRTidalv3`, which also includes dynamical tidal effects. The current effort to improve waveform models is crucial for performing accurate parameter estimation on the considered BNS system and is motivated by the requirement of meeting the enhanced sensitivity limit of next-generation GW detectors.

1.2 AIM AND MOTIVATION

This thesis project lays its foundation on the tidal perturbation formalism first developed by Hinderer (2008) and ultimately aims at its numerical implementation. More specifically, the main scientific objective of this thesis is to develop a solid computational model for the inclusion of tidal effects in the framework of hydrodynamical simulations in GR. The eventual goal is to accurately model the response of the NS configuration to tidal perturbations, enabling cross-validation of theoretical predictions with dynamically evolved quantities.

In order to tackle the complexities of the problem, this project adopts a blended approach that couples theoretical computations, formulated within the framework of metric perturbation theory, with general-relativistic hydrodynamic (GRHD) simulations of NSs. This integrated strategy is designed to take advantage of the complementary strengths of both analytical frameworks and computational methods, ensuring a comprehensive treatment of the problem. The code used for running the numerical simulations is `Gmunu` (`G`eneral-relativistic `mu`ltigrid `nu`merical solver), a parallelised, multi-dimensional curvilinear GRMHD code with an efficient multigrid elliptic solver, which is fully coupled with an efficient adaptive mesh refinement (AMR) module Cheong et al. (2020) Cheong et al. (2021). The initial conditions for the unperturbed NS are generated with the XNS code, which solves for the axisymmetric equilibrium configuration of relativistic stars Bucciantini & Del Zanna (2011) Pili et al. (2014) Pili et al. (2017a).

The novel element in this work lies in the direct numerical implementation of an external static tidal field in simulations of isolated NSs, rather than embedding the problem within the full dynamical evolution of a BNS system. This is achieved by directly encoding the tidal perturbation in the underlying spacetime metric, then allowing the hydrodynamic quantities to evolve in response to the deformed geometry. This setup enables the study of the tidal response of a NS in an isolated and controlled setting. By introducing the effect of an external quadrupolar field without explicitly simulating the companion star, it is possible to significantly reduce the computational cost while preserving the underlying physics of the tidal interaction. This simplification allows for a focused investigation of the structural response of the NS configuration, free from the complexities associated with full binary dynamics.

The use of GRHD simulations is strongly motivated by their extensibility, as they provide the required flexibility to test theoretical models under a wide range of realistic physical conditions. While the current implementation focuses on non-rotating, unmagnetised configurations, the computational setup is designed to be adaptable to more complex scenarios, potentially including magnetic fields, rotation, and more realistic equations of state. In this sense, the present work establishes a methodological foundation suitable to be expanded in future research and sets the stage for more general applications. Moreover, since they do not rely on linearisation, numerical simulations naturally incorporate non-linear effects in the fluid evolution, which may become significant in regimes of high stellar compactness or under strong tidal forces. This allows for a more accurate description of the system compared to the linear perturbative approaches employed in the analytical framework.

In conclusion, this project introduces a controlled approach to tidal interactions in the context of GRHD simulations and lays the foundation for the development of a new method to extract tidal deformability parameters from these simulations.

1.3 THESIS STRUCTURE

Chapter 2 is aimed at summarising the current knowledge on NSs and BNS systems, thereby offering the theoretical and observational background to frame the thesis project and embed it in the broader landscape of contemporary research. Section 2.1 provides a complete overview of the main properties and characteristics of NSs, discussing their formation, main physical features, internal composition, and EOS. Section 2.2 is dedicated to BNS systems and outlines their main formation channels together with their significance in GW astrophysics. Section 2.3 delves into the definition of tidal deformability and clarifies its key role in linking GW observations with the study of the internal composition of NSs. Section 2.4 reviews the relevance of numerical simulations and the main underlying principles.

Chapter 3 contains a comprehensive analytical treatment of the first-order perturbation originating from an external tidal field. The analytical framework follows the structure of the work by Hinderer (2008), reproducing and extending the published results. Section 3.1 lays the foundation for subsequent analytical computations by providing a rigorous definition of the tidal deformability in full GR and introducing the reader to the spherical harmonics decomposition. Section 3.2 reports the main body of the calculation in detail. Section 3.3 presents and discusses the numerical results obtained.

Chapter 4 contains the original computational contribution of this work, with the core objective of developing a numerical scheme to implement tidal perturbations in GRHD simulations of NSs. Section 4.1 introduces the `XNS` code and describes the process of constructing the equilibrium configuration for the simulated NS. Section 4.2 presents the novel computational scheme developed to modify the initial equilibrium configuration, with the goal of implementing a tidal perturbation on the metric functions. Upon completion of the pipeline, the output consists of perturbed initial data, which can then be injected into GRHD simulations within the `Gmunu` code. Section 4.3 is dedicated to the description of the `Gmunu` code and its main features, while Section 4.4 provides an overview of how a numerical simulation is initialised to test the developed methodology. Finally, Section 4.5 discusses the results obtained from the test simulation.

Chapter 5 is primarily focused on offering possible pathways for the interpretation of the results, paying particular attention to the assumptions underlying the computational setup and to other aspects that require careful consideration when drawing conclusions from the simulation outcomes. Section 5.1 focuses on the extraction of tidal deformability, or some related quantities, from the numerical data, and presents two distinct approaches for this purpose. Section 5.2 then examines the conditions under which a direct comparison between numerical results and theoretical predictions, or observational data, can be made in a scientifically valid manner.

Chapter 6 summarises the key steps of the research and presents the main conclusions drawn from the results obtained throughout the study. Section 6.1 includes a detailed discussion of possible future developments of the presented work.

Chapter 2

Binary neutron stars

NSs are the most compact stars observed and represent one of the most extreme states of matter in the Universe. Although NSs are most often paired to normal stars in binary stellar systems, a large amount of information on their properties and structure can be extracted from the evolution of BNS systems. BNS systems, constituted by two NSs orbiting around the common centre of mass, are among the most relevant GW sources for ground-based detectors. This chapter is aimed at summarising the current knowledge on NSs and BNS systems, thereby offering the theoretical and observational background to frame the thesis project and embed it in the broader landscape of contemporary research.

A complete overview on neutron stars' main properties and characteristics is provided in Section 2.1. Their formation, physical features, and internal composition are discussed in Subsections 2.1.1, 2.1.2, and 2.1.3 respectively. In the same Section, Subsection 2.1.4 gives a general outlook of the state-of-the-art knowledge on the NS EOS. Section 2.2 is dedicated to BNS systems and outlines their main formation channels together with their significance in GW astrophysics. Among the most interesting features that characterise NSs is the tidal deformability, which is a critical parameter in the study of BNS systems and is the focus of the present work. Section 2.3 delves into the definition of tidal deformability and clarifies its key role in linking GW observations with the study of the internal composition of NSs. Both isolated NSs and the dynamics of BNS systems have been extensively studied through general-relativistic (magneto)hydrodynamic simulations in numerical relativity. The relevance of numerical simulations and the main underlying principles are reviewed in Section 2.4.

2.1 Neutron stars

The existence of extremely compact stars constituted by closely packed neutrons was hypothesised shortly after the discovery of the neutron, which occurred in February 1932 by Chadwick (1932). The first explicit prediction of NSs dates back to December 1933, when Baade & Zwicky (1934) proposed the existence of NSs as the compact remnants of supernova (SN) explosions, characterised by very small radii and extremely high densities.

A significant contribution to the theoretical understanding of these compact stellar objects was made by Tolman, Oppenheimer and Volkoff, who investigated the conditions for gravitational equilibrium of matter composed predominantly by neutrons. In Tolman (1939), the author developed a general method for treating Einstein's field equation in order to obtain a set of explicit solutions written in terms of known analytic functions. Through this approach, Tolman recovered some already well-known solutions, including: Einstein cosmological solution for a fluid with constant density ρ and constant pressure P; the Schwarzschild interior solution for an incompressible fluid sphere with constant ρ and pressure P that decreases monotonically from the centre to zero at the boundary; the Einstein-de Sitter cosmological solution for an empty, expanding universe; the Schwarzschild exterior solution describing the vacuum surrounding a spherically symmetric mass distribution. In addition to these, Tolman proposed a number of new static solutions for the description of a fluid sphere in hydrostatic equilibrium surrounded by vacuum. This contribution was of great interest for the investigation of stellar structures within GR. The contemporaneous and related article Oppenheimer & Volkoff (1939) discussed the general relativistic treatment of the equilibrium configuration for a spherically symmetric matter distribution, and treated the ideal case of a cold, degenerate neutron gas using the relativistic Fermi EOS. The obtained results were found to be qualitatively in agreement with appropriately chosen particular cases of the analytic solutions previously derived by Tolman.

These complementary works led to the formulation of the Tolman–Oppenheimer–Volkoff (TOV) equations, which describe the condition for hydrostatic equilibrium of a spherically symmetric perfect fluid distribution within the framework of GR. They also showed that no stable NS configuration can exist above a certain critical mass. The so called TOV limit represents the theoretical upper bound to the mass of a stable, non-rotating NS.

The first observational evidence of NSs only came years later in 1967, when Jocelyn Bell and Antony Hewish discovered regular radio pulses from a source in the Crab Nebula that was later identified as belonging to the class of pulsars, rapidly rotating NSs emitting narrow beams of radiation Hewish et al. (1968). From that moment on, many radio observations of astrophysical objects involving NSs followed, which include millisecond pulsars, binary radio pulsars, high-mass X-ray binaries and low-mass X-ray binaries. Throughout the late 20th century, these sources became the subject of extensive study. The advent of ground-based GW detectors in the past decade enabled a great leap in the characterisation of NSs, as Section 2.2 discusses in further detail. In particular, the first joint detection of both a gravitational and an electromagnetic counterpart from the BNS inspiral GW170817 Abbott et al. (2017) opened new avenues for the investigation of such extreme objects, marking the birth of multi-messenger astrophysics.

2.1.1 FORMATION

As foreseen by Baade and Zwicky, NSs are the product of stellar evolution. In particular, they originate at the culmination of the evolutionary path of quasi-massive ($8M_{\odot} \lesssim M \lesssim 10M_{\odot}$) and massive ($M \gtrsim 10M_{\odot}$) stars.

Quasi-massive stars are able to ignite carbon under non-degenerate conditions, developing a degenerate Neon-Oxygen core. If the mass of the degenerate core exceeds the Chandrasekhar limit [1], the evolution proceeds through an electron capture SN. The explosion is triggered by electron captures that, depriving the star of free electrons, decrease the degeneracy pressure support and cause the onset of a dynamical instability. In this scenario, the compact remnant is a low-mass neutron star Kippenhahn et al. (c2012).

NSs can also form as compact remnants of core-collapse SNe, which occur at the terminal stage of the evolution of massive stars. A graphical representation of the explosion mechanism in core-collapse SNe is illustrated in Figure 2.1.

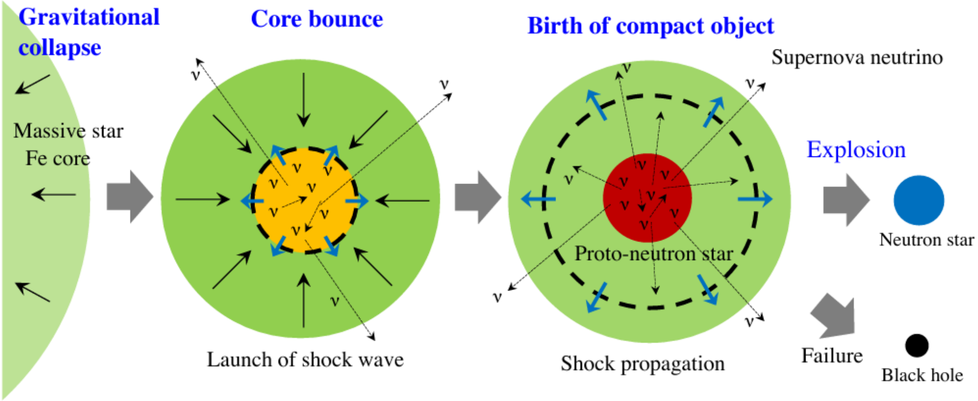

Figure 2.1: Schematic representation of the core-collapse SN process leading to the formation of a compact object Sumiyoshi et al. (2023).

Massive stars are able to complete all the advanced burning stages while never undergoing electron degeneracy, fusing heavier and heavier elements and eventually reaching the formation of a degenerate iron core. The core is surrounded by a series of active nuclear burning shells in a so called *onion-skin* structure. Accreting the products of the Silicon burning taking place in the above shell, the degenerate core grows in mass. As the core mass outgrows the Chandrasekhar limit, the electron degeneracy pressure fails to sustain the core in hydrostatic equilibrium and a dynamical instability sets in. The onset of the collapse is accelerated by two main physical processes: on the one hand, electron captures enrich the chemical composition with neutrons while simultaneously lowering the electron degeneracy pressure support; on the other hand, photo-disintegrations absorb energy from the radiation field, thus decreasing the support by radiation pressure. The gravitational collapse starts from the core and is accompanied by a dramatic increase in the internal density. When nuclear values $\rho \approx 10^{14}$ g cm^{-3} are reached, the EOS becomes stiff and matter turns into almost incompressible. As a result, the collapse is halted and the infalling material is forced to bounce back on the stiff core and reverse its motion. As the rebounding core encounters the infalling layers, an outward-propagating shock wave is formed. However, the shock wave quickly loses energy and is weakened at the point it finally stalls, not being able to eject the entire envelope. Therefore, no prompt explosion can occur. Neutrinos play a central role in revitalising the shock wave, as they carry most of the energy generated in the gravitational collapse of the core and are able to deposit some in the outer layers. In this way, a core-collapse SN is successfully triggered.

---

[1] The Chandrasekhar limit sets the maximum mass that can be sustained by a spherically symmetric configuration in hydrostatic equilibrium supported by degeneracy pressure.

Depending on the initial mass of the star and on the efficiency of the accretion by fallback on the proto-NS, the final compact remnant is either a NS - if the total mass remains below the TOV limit - or a BH if this threshold is exceeded. The remnant type is also influenced by the mass loss rate resulting from stellar winds during the lifetime of the progenitor star. For low mass loss rates, the upper limit of the initial progenitor mass for NS formation is approximately 25 $M_{\odot}$. Above this threshold, the collapse typically results in a BH. In contrast, high mass loss rates during the pre-SN stages reduce the efficiency of fallback accretion, thereby disfavouring BH formation. Under these conditions, only a narrow range of initial progenitor masses - between 25 and 40 $M_{\odot}$ - can lead to BH formation, while more massive progenitors are more likely to produce a NS.

2.1.2 Physical features

Observational constraints indicate that NS masses typically range between $1.1 M_{\odot}$ and $2.3 M_{\odot}$. The heaviest known galactic NS has been estimated to have $M_{\text{PRS J0952-0607}} = (2.35 \pm 0.17)\ M_{\odot}$ Romani et al. (2022). For what concerns NS radii, high-quality datasets from X-ray satellites combined with considerable advancements in theoretical modelling pinpoint the average equatorial radius in the $\sim 10 - 13$ km range Özel & Freire (2016). The simultaneous measurement of both mass and radius of a NS was first performed in 2019 thanks to the X-ray data collected by the Neutron Star Interior Composition ExploreR (NICER) Miller et al. (2019) Riley et al. (2019). The NICER instrument is installed on the International Space Station and detects the soft thermal X-ray emission that originates from the hot polar caps of rotation-powered millisecond pulsars (MSPs). It is by modelling the pulse profile, i.e. the periodic modulation of the X-ray flux as a function of energy and time, that it is possible to jointly infer both the mass and the equatorial radius of the observed object.
The central density inside a NS can reach up to roughly 5 to 10 times the characteristic density of atomic nuclei $\rho_{nuc} \approx 2.7 \times 10^{14}$ g cm^{-3} Lattimer & Prakash (2001). This peculiarity makes the study of NSs pivotal to shed light on the properties and behaviour of matter at supra-nuclear densities.

As a consequence of the magnetic flux conservation during the gravitational collapse of the progenitor massive star, NSs are also highly magnetised objects, displaying magnetic fields of the order $B \sim 10^{12}$ G. The NS class of the so-called *magnetars* is endowed with the strongest magnetic fields known in astrophysics, with surface strengths reaching up to $10^{14} - 10^{15}$ G Duncan & Thompson (1992).

2.1.3 Internal structure

The internal structure of NSs is highly complex and appears to be stratified, featuring a sequence of distinct layers, each characterised by different composition and physical properties. A schematic graphical representation of the internal stratification of a NS is shown in Figure 2.2.

The outermost layer is an extremely thin atmosphere that surrounds the star, typically only a few cm in height. Since the atmospheric scale height is dictated by the pressure scale height, there is no surprise for it being so thin. Despite its minimal size, the atmospheric layer plays a crucial role in modifying the emergent radiation: it absorbs, reprocesses, and re-emits thermal

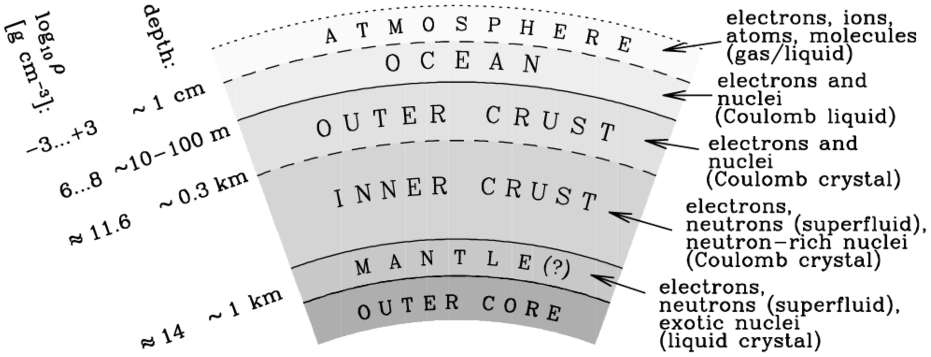

Figure 2.2: Schematic representation of the internal structure of a NS, illustrating its layered composition. The picture provides approximate depth and density ranges for each region, together with a brief description of their main constituents and physical state Chamel & Haensel (2008).

photons emitted from the surface, thereby shaping the observable spectrum. The composition of this layer may vary, but typically reflects stellar atmospheres as it mainly consists of ionised hydrogen.

Beneath the atmosphere, the surface of the NS consists of an ocean of condensed matter, composed primarily of heavy elements such as iron. Already ~ 22 cm below the surface, the density reaches $\rho \sim 2 \times 10^4$ g cm^{-3} and the interatomic distance is comparable to the atomic radius. Ionisation is induced by pressure, leading to fully ionised atoms.

The solid crust of the NS is stratified and can be distinguished into outer and inner layers. The outer layers are formed by a solid Coulomb lattice of neutron-rich nuclei. As the density increases above $\rho \sim 10^7$ g cm^{-3}, the gravitational compression becomes so strong that it forces neutronisation of matter through electron captures. The deeper inside the star, the more neutron-rich matter becomes. The inner crust layer extends roughly between $\rho \sim 10^{11}$ g cm^{-3} and $\rho \sim 10^{14}$ g cm^{-3} and is characterised by a sea of free neutrons in a superfluid state. At the bottom of the crust, matter is predicted to be shaped in various phases of non-spherical nuclei with different specific geometries, the so-called "nuclear pasta" Chamel & Haensel (2008). Even if the crust accounts for only a small fraction of the total mass of a NS, constructing crust models is crucial because the crust's physics is intimately related to many observed NS phenomena Chamel & Haensel (2008). The role of the crust on the tidal deformability of a NS has been investigated assuming a realistic EOS by Perot et al. (2020).

Finally, the core occupies the innermost region of the star, where the density exceeds the nuclear saturation density $\rho_{nuc} \approx 2.7 \times 10^{14}$ g cm^{-3}. Under such extreme conditions, matter could transition from the ordinary nucleonic phase to more exotic forms. Many theoretical phenomenological models include hyperonic matter Oertel et al. (2017) or deconfined quarks Baym et al. (2018), while also other exotic possibilities like color-superconducting phases or boson (e.g. muon, pion, kaon) condensates have been considered.

2.1.4 EQUATION OF STATE

In its most generic form, an EOS is an analytical relation linking together thermodynamic state variables such as pressure, density, temperature, entropy. The construction of an EOS implicitly assumes that local thermodynamic equilibrium holds in the considered system. In the specific case of NSs, the EOS is most often expressed in a barotropic form, which means that the pressure p is given as a function of the density ρ. A very simplified treatment for the EOS of matter inside NSs is provided by the polytropic assumption. A polytropic EOS expresses the pressure p as a power-law function of the density ρ

$$p = K\rho^{\Gamma} \qquad \text{with} \quad \Gamma = 1 + \frac{1}{n} \ , \tag{2.1}$$

where K is the polytropic constant, Γ is the adiabatic index and n is the polytropic index. The fundamental differential equation that governs the stellar structure under a polytropic assumption is the Lane-Emden equation, which, allowing for analytical solutions for particular values of n Chandrasekhar (1939), provides a great simplification of the problem. Despite being a rather crude approximation, the polytropic model is often used because of its flexibility: by varying one single parameter only, it is possible to capture a wide range of stiffness levels for NS matter.

However, as previously discussed, NSs exhibit a diverse set of physical regimes throughout their internal structure. For this reason, applying one single polytropic model to the entire star fails to accurately describe its complexity. One common approach to address this issue is to divide the overall EOS into several segments, each referring to a polytropic relation with unique parameters K_i and Γ_i and only valid over a specific limited density range. The result is called a piecewise polytrope. While piecewise models allow for a more consistent treatment of the outer crust, the inner crust, and the core of the star Suleiman et al. (2022), their main drawback lies in the non-differentiability of quantities, as they are not continuously defined throughout the star's interior. In particular, Suleiman et al. (2022) points out the relevance of fitting piecewise polytropic models to unified (rather than non-unified) equations of state in order to minimise the fit error in retrieving macroscopic parameters like mass M, radius R, moment of inertia I and dimensionless tidal deformability Λ.

Non-unified equations of state are common to find in the literature. They are constructed by matching together an EOS for the crust and one for the core, independently computed using different nuclear models for each sector of NS matter. The matching procedure is a thorny one, and must be handled very carefully to avoid a non-physical behaviour of the thermodynamic quantities and large artificial errors. To allow for more detailed predictions of NS macroscopic parameters and dynamical properties, considerable effort has been put into developing unified equations of state, which describe NS matter from the centre to the surface on the basis of the same nuclear interaction model (see, e.g. Fortin et al. (2016)). Current realistic EOS models are too complex to be expressed in a closed form, so the numerical results for the thermodynamic quantities are sampled over a grid and stored in a table.

2.2 BINARY NEUTRON STAR SYSTEMS

While the study of isolated NSs successfully provides baseline constraints on their physics and EOS, BNS systems offer a much richer setting that unlocks additional layers of information.

The advent of GW detectors and the first joint GW and electromagnetic observation of a BNS coalescence detected on 17 August 2017 by LIGO and Virgo - event GW170817 Abbott et al. (2017) - marked a breakthrough in multi-messenger astrophysics and represented a major leap forward in a number of research areas. Following event GW170817, BNS systems have become an extremely powerful tool for probing NS interiors, as new avenues were opened for the investigation of NSs through multi-messenger astrophysics. In particular, thanks to GW data analysis, it has been possible to narrow the family of acceptable EOS models by ruling out the ones which did not meet the requirements (see, e.g. Annala et al. (2018)). At present, the most stringent constraints on the EOS of NS matter have been inferred through multi-messenger observations that combine electromagnetic data with the detected GW events of binary neutron stars GW170817 and GW190425 (see e.g. Radice et al. (2018), Raaijmakers et al. (2021)). Recent work by Walker et al. (2024) combined simulated observations of BNS mergers as expected by the next-generation detectors Cosmic Explorer (CE) and Einstein Telescope (ET) and determined future plausible constraints on the EOS across a reasonable NS mass range.

2.2.1 FORMATION

Although at present many questions remain open about the stellar origin of BNS systems, a preferred *standard* formation channel can be identified for the vast majority of them Tauris & van den Heuvel (2006) Vigna-Gómez et al. (2018). A graphical representation of its characteristic sequence of events is provided in Figure 2.3.

The *standard* formation channel involves, at its earliest stage, a binary system featuring two massive stars in Zero-Age Main Sequence (ZAMS), at least one of them exceeding $8M_{\odot}$. If the orbital separation between the two binary components is short enough, a mass transfer can occur from the initially more massive star (the so-called *primary* component, acting as the donor) and the initially least massive one (the *secondary* component, being the accretor). In case of stable mass transfer by Roche lobe overflow (RLO), matter flows through the inner Lagrangian point L1 of the system and is efficiently accreted by the companion star. According to most models, the donor star evolves faster and first reaches the latest stage of its evolution, eventually undergoing a core-collapse SN. If the system survives the first SN explosion and remains bound, a high-mass X-ray binary (HMXB) is formed. A HMXB features a NS and a hot, massive, luminous star of the first spectral types (O-B). In this setting, as the massive star evolves, it overfills its Roche lobe and another mass transfer episode sets in. This time, the mass transfer is unstable and leads to the formation of a common envelope (CE) surrounding the entire system. In order for the evolution to proceed towards the formation of a BNS, the common envelope needs to be expelled. This can happen only if the orbital period of the binary is long enough, meaning that the binding energy of the envelope is rather weak. Subsequently to the successful expulsion of the CE, the binary system is constituted by a NS and a bare Helium core deprived of all the outer stellar layers. Depending on the orbital separation of the system and on the mass of the remnant Helium core, the secondary component can undergo one last mass transfer episode, eventually terminating its life in an ultra-stripped SN and producing a young pulsar as a compact remnant. The survival of the system to the second SN explosion depends not only on the orbital separation, but also on the magnitude of the velocity kick received by the newly formed NS at birth. However, once this stage is reached, most of the systems are expected to remain bound and a BNS is eventually created Tauris et al. (2017).

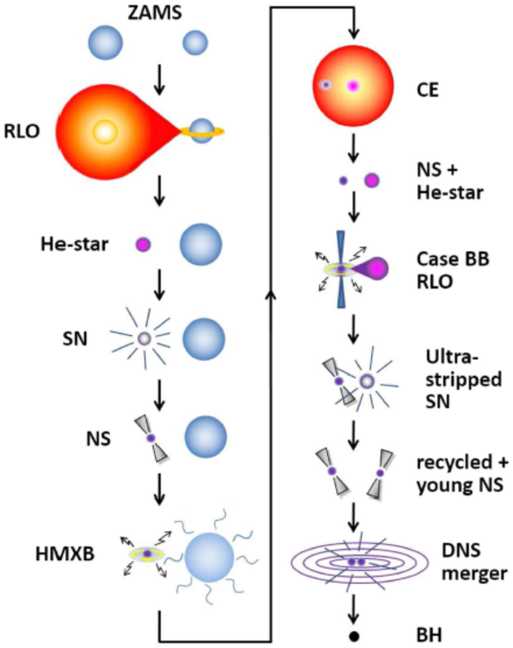

Figure 2.3: Graphical illustration of the birth of a BNS system through the *standard* formation channel. Eventually, the double neutron star (DNS) undergoes a merger event, which leads to the generation of a black hole (BH) as compact remnant Tauris et al. (2017).

An extensive study on the evolution of BNS progenitors and formation scenarios of BNS systems has recently been carried out by Pellouin et al. (2025). Together with the *standard* track, they identified two other dominant evolutionary tracks to form binary neutron stars that reach a merger event within the age of the Universe: the *equal-mass* track, where both progenitors evolve quasi-simultaneously on synchronised timescales and a common envelope is formed around the two giant stars; a track involving the formation of an Oxygen-Neon white dwarf (WD), followed by its accretion-induced collapse due to mass transfer from the companion star.

2.2.2 Evolution and detection

After a BNS is formed, its evolution proceeds through an inspiral phase, during which part of the orbital energy of the system is released in the form of GW radiation with a consequent shrinking of the orbit. As the system evolves, both the amplitude and the frequency of the emitted GWs increase, reaching their peaks at the time of merger. The inspiral process has long been predicted to produce a GW signal that could be observed by ground-based GW detectors Hawking & Israel (1987) Brillet & Giazotto (1989), an outlook that received confirmation with the detection of event GW170817. An overview of the evolution stages of a BNS system and the corresponding emitted GW signal is shown in Figure 2.4.

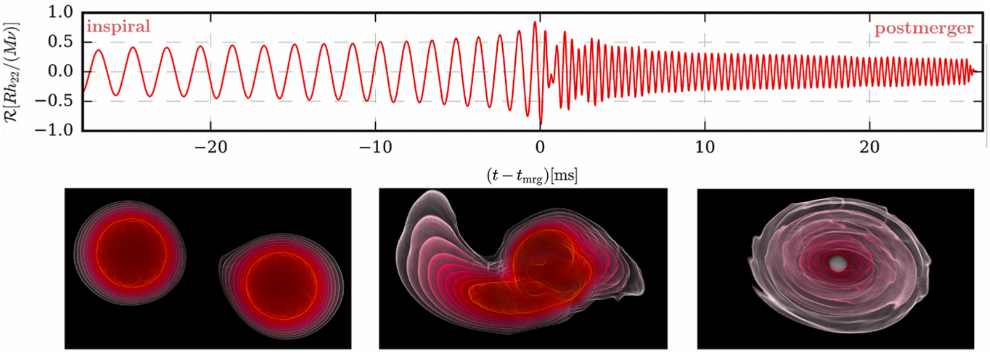

Figure 2.4: Numerical relativity simulation of a BNS coalescence displaying the GW signal and the matter evolution. *Top panel*: gravitational waveform of the signal emitted during the late inspiral phase (the last orbits before the merger) and the post-merger phase. *Bottom panel*: rest-mass density evolution during the inspiral (left-hand panel), the merger (middle panel) and the post-merger (right-hand panel) stages Dietrich et al. (2021).

Depending on the properties of the binary, the GW signal produced during the late inspiral typically reaches frequencies around ∼ 1-2 kHz just before the merger. After the two binary components have merged, the remnant oscillations continue around 2-4 kHz, but with lower amplitude. The frequency sensitivity range of the two Advanced LIGO detectors (Hanford, Washington, and Livingston, Louisiana) and the Advanced Virgo detector (Cascina, Pisa, Italy) covers a broad frequency range between roughly 20 Hz and 5 kHz, with a sensitivity peak around ∼ 100 Hz and decreasing sensitivity at higher and increasing frequencies. This means that current ground-based detectors are the most sensitive to the late inspiral phase, corresponding to the final minutes preceding merger, during which the signal falls within the most sensitive frequency band of the detectors. Instead, the merger event and the post-merger ringdown are much harder to extract from the detector noise and to be detected because at such high frequencies the sensitivity of the Advanced LIGO and Advanced Virgo interferometers is significantly reduced.

Throughout the years, the sensitivity of LIGO and Virgo detectors has been constantly improved and further advancements are predicted prior to the fifth observation run O5, foreseen to start in year 2026. The sensitivity of Advanced Virgo as a function of the GW frequency in terms of the (amplitude spectral density of the) interferometer output noise, expressed in units of GW strain, is represented in the left-hand panel of Figure 2.5. Such incremental improvements in sensitivity are expected to allow a higher detection rate of BNS systems, but will not alone give access to other evolutionary stages than the late inspiral.

The advent of third-generation detectors such as the Einstein Telescope (ET) will open new windows on the study of BNS coalescence. The ET is designed to improve sensitivity by roughly one order of magnitude with respect to Advanced LIGO and Advanced Virgo, while at the same time significantly broadening the observable frequency band. While the extended low-frequency responsiveness will allow observations of the inspiral phase for a longer period previous to merger, the improved high-frequency response could provide detailed information about the merger dynamics and the behaviour of the post-merger remnant. This will enable a comprehensive picture of the coalescence process in all its stages.

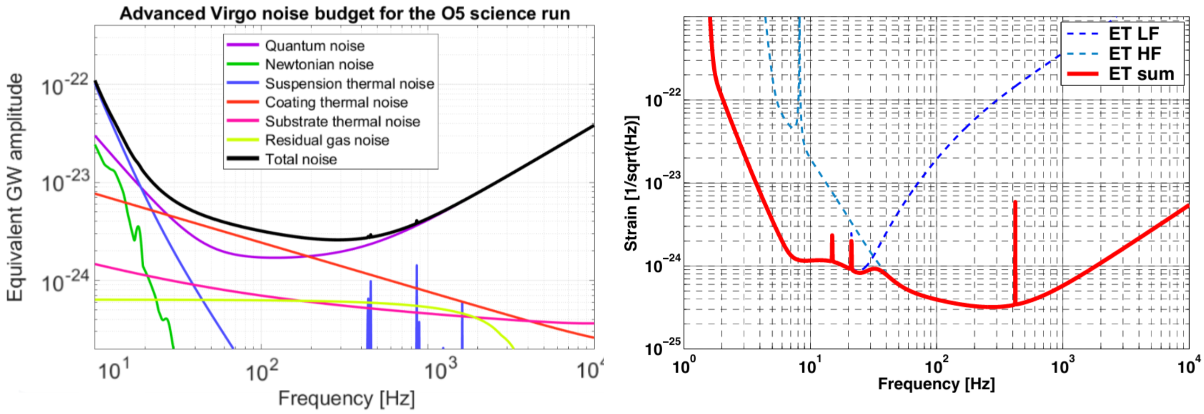

Figure 2.5: *Left-hand panel*: projected sensitivity for Advanced Virgo during the fifth observation period O5, foreseen to start in year 2026. The final expected sensitivity curve (black solid line) results from the sum of the most relevant noise contributions. (https://www.virgo-gw.eu/science/detector/sensitivity/). *Right-hand panel*: sensitivity goal for the Einstein Telescope. The dashed dark blue curve refers to the low-frequency sensitive cryogenic interferometer, while the dashed light blue curve refers to the high-frequency sensitive room-temperature interferometer. The total detector sensitivity is shown as the solid red curve Hild et al. (2011).

The ET baseline design features a triangular configuration composed of three nested detectors arranged in an equilateral triangle, each with 10 km-long arms. This geometry ensures sensitivity to both GW polarizations and is characterised by a uniform antenna pattern, which allows for continuous observation without blind spots. Each arm hosts a pair of interferometers in a *xylophone* configuration: one optimized for low-frequency sensitivity by operating at cryogenic temperatures and the other for high-frequency sensitivity at room temperature. The preferred construction site for this instrumental setup is the Euregio Meuse-Rhine region, situated between Belgium, Germany, and the Netherlands.

An alternative design under consideration, especially in the context of a possible Italian site in Sardinia, involves two L-shaped detectors oriented at 45 degrees with respect to each other. This setup simplifies construction and site requirements while still allowing for polarization disentanglement. However, it is not efficient in source localisation and allows poorer noise diagnostics compared to the triangular design.

The ET is predicted to achieve broad-band sensitivity down to ∼ 1 Hz in the low-frequency limit and up to ∼ 10 kHz in the high-frequency limit Sathyaprakash et al. (2012). The predicted sensitivity curve for ET is shown in the right-hand panel of Figure 2.5. By comparison with the left-hand panel of Figure 2.5, it is immediate to grasp the significant improvement in sensitivity.

2.3 The tidal deformability λ

One of the key quantities that can be extracted from GW observations of BNS systems is the tidal deformability, whose measurements helped setting tighter constraints on the EOS of NSs. When a NS is placed in an external perturbing tidal field, its configuration develops an induced quadrupole moment as a response. The shape of the star suffers from a deformation, the extent of which is parametrised by the tidal deformability parameter λ. BNS systems provide a natural astrophysical setting for this type of tidal interactions, as each component of the binary is subject to and deformed by the gravitational field generated by the companion compact star.

The tidal deformability λ is mathematically defined as the ratio between the induced quadrupole moment Q_{ij} developed by the star and the external perturbing tidal field $\mathcal{E}_{ij}$ causing the perturbation

$$\lambda \equiv -\frac{Q_{ij}}{\mathcal{E}_{ij}} \ . \tag{2.2}$$

Equation (2.2) holds for both the Newtonian and relativistic case. In the relativistic case, this definition assumes a preferred time axis, which is typically defined by choosing to perform the computations in the local asymptotic rest frame of the NS. This allows the decomposition into spatial tensors to be well-defined and the tensor components to be frame-independent. The minus sign captures the opposite directional response of the induced quadrupole moment relative to the external tidal field. It emphasises the restoring tendency of the induced quadrupole moment Q_{ij}, which represents the attempt of the NS configuration to counteract the deformation.

The dimensional analysis of Equation (2.2) suggests a strong dependence of the tidal deformability parameter on the radius of the star. In fact, the quadrupole moment is defined as

$$\begin{aligned} Q_{ij} &\equiv M_{ij} - \frac{1}{3}\delta_{ij} M^{kk} \\ &= \frac{1}{c^2}\int d^3x\ T^{00}(t,\vec{x})\ x_i x_j - \frac{1}{3}\delta_{ij}\frac{1}{c^2}\int d^3x\ T^{00}(t,\vec{x})\ x^k x^k \\ &= \int d^3x\ \frac{T^{00}(t,\vec{x})}{c^2}\ x_i x_j - \frac{1}{3}\int d^3x\ \delta_{ij}\ \frac{T^{00}(t,\vec{x})}{c^2} x^k x^k \ , \end{aligned} \tag{2.3}$$

where M^{ij} is the second-order momentum of $T^{00}(t,\vec{x})/c^2$, defined as

$$M^{ij} \equiv \frac{1}{c^2}\int d^3x\ T^{00}(t,\vec{x})\ x^i x^j \ , \tag{2.4}$$

and T^{00} is the 00 component of the stress-energy tensor $T^{\mu\nu}$ associated to the source. From the definition in Equation (2.3) it is clear why a preferred time direction needs to be specified: without such a choice, one could perform a coordinate transformation to arbitrarily change, for example, T^{00}, thus making the interpretation of λ ambiguous.

In the most generic case, T^{00} includes not only the rest-mass energy of the source, but also other energy contributions, such as the kinetic energy of the particles that constitute the source and their potential energy. When considering sources that generate a strong gravitational field, such as NSs, the gravitational binding energy becomes also important and must be included. However, for the purpose of performing a dimensional analysis, let us restrict to the simpler Newtonian case. For weak-field sources in the non-relativistic limit, T^{00} represents the rest-mass energy of the source, and the T^{00}/c^2 term reduces to the rest-mass density. Under these assumptions, it is true that $\frac{T^{00}(t,\vec{x})}{c^2} = \rho(t,\vec{x})$. Therefore, in the Newtonian limit, the quadrupole moment is related to the rest-mass density perturbation $\rho(t,\vec{x})$ by

$$Q_{ij} = \int d^3x\ \rho(t,\vec{x})\ (x_i x_j - \frac{1}{3}\delta_{ij} x^k x^k) = \int d^3x\ \rho(t,\vec{x})\ (x_i x_j - \frac{1}{3}\delta_{ij} r^2) \tag{2.5}$$

and has units $[Q_{ij}] = \mathrm{kg} \cdot \mathrm{m}^2$ according to the International System. In geometrized units $(G = c = 1)$, the quadrupole moment has dimensions of length cubed $[Q_{ij}] \sim L^3$.

Again in a Newtonian context, the quadrupolar external tidal field is defined as the second derivative of the external gravitational potential ϕ_{ext}

$$\mathcal{E}_{ij} = \partial_i \partial_j \phi_{\mathrm{ext}} = \frac{\partial^2 \phi_{\mathrm{ext}}}{\partial x^i \partial x^j} \tag{2.6}$$

thus $[\mathcal{E}_{ij}] = \mathrm{s}^{-2}$ which in geometrized units becomes $[\mathcal{E}_{ij}] \sim L^{-2}$.

This results in the tidal deformability having dimensions of a length to the fifth power: $\lambda \sim R^5$. Since the length scale of the system in a NS is set by its radius R, the tidal deformability is expected to scale as $\lambda \sim kR^5$ with k a dimensionless constant. To keep up with traditional conventions in literature Hinderer (2008), the tidal deformability is expressed as

$$\lambda = \frac{2}{3} k_2 R^5 \tag{2.7}$$

where k_2 is the gravitational Love number.

Equation (2.7) is historically significant as it directly quantifies the tidal response of the NS configuration. It also highlights the strong dependence of the tidal deformability parameter on the stellar structure, which points to a strong sensitivity on the EOS of NS matter. However, such a strong dependence often hinders a clear picture of EOS effects. To allow for a more immediate interpretation of the numerical results, a commonly used quantity is the dimensionless tidal deformability Λ, defined as

$$\Lambda \equiv \frac{\lambda}{M^5} = \frac{2}{3} k_2 \frac{R^5}{M^5} = \frac{2}{3} k_2 C^{-5}\ , \tag{2.8}$$

where M is the mass of the star and $C \equiv M/R$ is the compactness parameter.
Moreover, most GW observations do not directly constrain the individual dimensionless tidal deformability of each binary component, but rather a combination $\tilde{\Lambda}$ of them, which is defined as

$$\tilde{\Lambda} \equiv \frac{16}{3} \frac{(m_1 + 12 m_2) m_1^4 \Lambda_1 + (m_2 + 12 m_1) m_2^4 \Lambda_2}{(m_1 + m_2)^5}\ , \tag{2.9}$$

where $\Lambda_1 \equiv \lambda_1/m_1^5$ and $\Lambda_2 \equiv \lambda_2/m_2^5$ are the dimensionless tidal deformabilities of the two binary components of masses m_1 and m_2 respectively Favata (2014).

The dependence of the tidal deformability on the EOS of NS matter can be easily understood with the following reasoning. For a stiff EOS, the steep pressure gradient $dP/d\rho$ implies that a substantial increase in pressure is required to produce even the smallest increase in the density, therefore matter resists compression effectively. As a results, for a given mass, NSs with a stiff EOS tend to have larger radii and are less compact Lattimer & Prakash (2001). Since less compact stars deform more easily under an external tidal field, they exhibit a higher tidal deformability. Conversely, a soft EOS features a small pressure gradient $dP/d\rho$, which means that a modest change in pressure is sufficient to produce a comparable variation in density. It follows that matter is easily compressed and, for a given mass, NSs endowed with a soft EOS tend to have smaller radii and be more compact Lattimer & Prakash (2001). A more compact star is less susceptible to tidal deformation, resulting in a lower tidal deformability parameter.

As already pointed out, NS binaries are a natural setting to investigate tidal interactions as each component is subject to the gravitational tidal field of the companion star. The configuration of each NS is adiabatically deformed, deviating from a spherical shape towards an oblate ellipsoid. The timescale over which such deformation occurs is faster than the orbital motion modulating the external perturbing field, so the tidal bulge in each star faces the companion.

To leading order, GW emission is sourced by a time-varying quadrupole moment Maggiore (2007), and changes in time of Q_{ij} produce gravitational radiation according to

$$[h_{ij}^{TT}]_{\text{quad}} \equiv \frac{1}{r}\frac{2G}{c^4}\,\ddot{Q}_{ij}^{TT}(t - r/c)\ . \tag{2.10}$$

In a binary system, the leading contribution to the quadrupole moment comes from the orbital motion, which causes the mass distribution to vary in time. In the specific case of NS binaries, the induced quadrupole moment of tidal origin constitutes a sub-leading contribution that affects the binding energy of the system and its subsequent evolution.

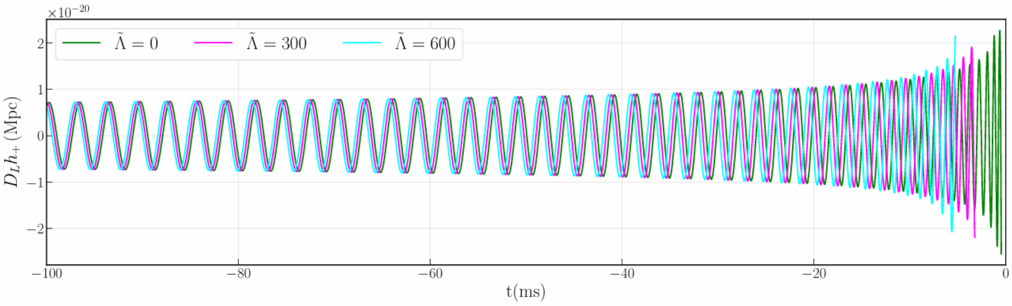

Figure 2.6: Waveform model for the late stages of the coalescence of two equal-mass ($m_1 = m_2 \equiv m = 1.4M_\odot$) non-spinning NSs for different values of $\tilde{\Lambda}$. The used waveform model is `IMRPhenomD_NRTidalv2` Dietrich et al. (2019a) Dietrich et al. (2019b). The major phase correction to the waveform arises during the late inspiral, as the two NSs approach each other. Moreover, larger values of $\tilde{\Lambda}$ lead to enhanced energy emission and hence to a faster overall system evolution Chatziioannou (2020).

During the early stage of the inspiral, the two stars are sufficiently far apart that tidal interactions are negligible. The GW signal emitted in this phase is indistinguishable from that of two inspiraling BHs of equal masses and spins. As the binary evolves, the loss of orbital energy brings the two NSs closer and closer to each other, up to the point where tidal effects become dominant. At this stage, tidal forces effectively enforce a deformation on the two binary components at the expense of the orbital energy of the system. It follows that the additional tidal contribution to the mass quadrupole moment has the effect of extracting orbital energy from the system at a faster rate than it would happen if the stars were perfectly spherical in shape. The overall evolution of the system proceeds faster: the inspiral accelerates and the binary evolves more rapidly towards the eventual merger event. As a result, the emission of GWs is enhanced Peters & Mathews (1963) Peters (1964) Blanchet (2024). In this phase, tidal forces effectively modify the gravitational waveform of the GW signal by introducing a phase shift, and such correction is parametrised by the tidal deformability parameter.

As a result, by affecting the evolution of the system, the tidal properties of NSs leave a direct imprint on the emitted GW signal, as clearly shown in Figure 2.6. In this way, a link is established between the emitted gravitational radiation and the EOS describing matter at supra-nuclear densities.

2.4 NUMERICAL SIMULATIONS

General-relativistic magnetohydrodynamic (GRMHD) simulations have become essential tools for understanding the complex behaviour of NSs, as well as for predicting and interpreting the evolution of BNS systems. The use of numerical simulations is imperative to capture the non-linear behaviour of Einstein field equations in GR. In the strong-field regime, non-linearities naturally arise due to the self-coupling between the spacetime curvature and the energy-momentum content of matter. During the late inspiral and the merger phase, the onset of non-linearities is further complicated by the complex interplay between gravitational interactions, hydrodynamic forces and magnetic fields. The assumption of small perturbations acting on a fixed background spacetime breaks down, therefore perturbative approaches gradually lose accuracy and eventually fail. This means that numerical simulations are the only means to calculate the GW emission from the merger and post-merger phase of a compact binary system, which is crucial for the construction of accurate templates for the gravitational waveforms. Such templates are then used to relate the source properties to the observed GW signal through a matched-filtering procedure. Therefore, detailed knowledge of the expected waveforms is essential for a correct interpretation of the signal and for an accurate inference of the astrophysical properties of their sources. With the advent of next-generation detectors, a significant improvement in waveform models will be required to keep pace with their increased sensitivity and to conduct meaningful GW data analysis.

GRMHD simulations are based on numerical relativity (NR), which involves solving Einstein field equations numerically using computational methods. Unlike analytical approaches, NR does not rely on approximations or perturbative techniques. It applies to the strong-gravitational field case and allows for the full evolution of highly dynamical, non-linear spacetimes. The fully covariant formulation of Einstein field equations is

$$G_{\mu\nu} = 8\pi T_{\mu\nu} \ , \tag{2.11}$$

where $G_{\mu\nu}$ is the Einstein tensor, which contains the derivatives of the metric and is a measure of the curvature of spacetime, while $T_{\mu\nu}$ is the stress-energy-momentum tensor describing the source. Einstein equations are coupled and highly non-linear, and their form as given in Equation (2.11) is not suitable for numerical computations as time and space are treated in the same way. In NR, one would rather cast Equation (2.11) into an initial value problem and evolve that in time.

To do so, the most common approach involves a (3+1) decomposition, also referred to as ADM formalism after its inventors Arnowitt, Deser and Misner Gourgoulhon (2007). This consists in slicing the spatial three-dimensional (3D) geometry along a sequence of steps in a time-like coordinate t. As a result, spacetime is splitted into a mono-parametric family of 3D hypersurfaces separated by differential displacements in the time coordinate t. In the (3+1) formalism, the time-like coordinate is chosen along a normal direction to the space-like hypersurfaces. The time evolution of the metric is expressed as first-order time derivatives, while the Einstein tensor contains second-order time derivatives. Thanks to this approach, it is possible to disentangle the four spacetime dimensions and implement the time evolution of space in a more intuitive and computationally efficient way Wilson & Mathews (2003). In the ADM picture, the spacetime interval between any two points can be written as

$$\begin{aligned} ds^2 &= g_{\mu\nu} dx^\mu dx^\nu = \\ &= -\alpha^2 dt^2 + \gamma_{ij}\ (dx^i + \beta^i dt)(dx^j + \beta^j dt) = \\ &= -(\alpha^2 - \beta_i \beta^i)\ dt^2 + 2\beta_i dx^i dt + \gamma_{ij} dx^i dx^j\ , \end{aligned} \tag{2.12}$$

where α is the lapse function, controlling the rate of time evolution; β^i is the shift vector, which determines how spatial coordinates vary from one 3D hypersurface to the next one; γ_{ij} is the metric associated to the 3D geometry of each slice. A schematic picture of the ADM metric is represented in Figure 2.7.

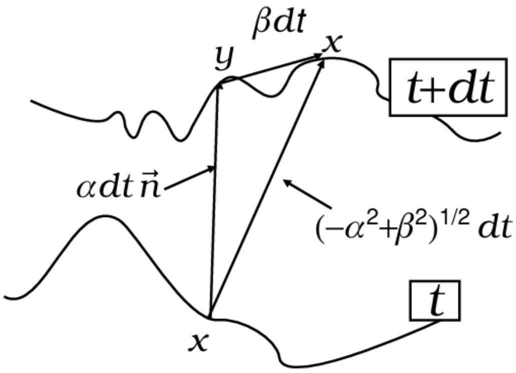

Figure 2.7: Two-dimensional schematic representation of the ADM decomposition for the metric. The vector $\vec{n}$ depicts the normal direction to the spatial hypersurface Wilson & Mathews (2003).

In the framework of (3+1) decomposition, it is possible to reduce the Einstein equations to a set of constraints that must hold at all times, coupled with a system of evolution equations governing the time evolution of the system. This formulation, involving constraints that are solved in parallel with evolution equations, is said to be based on a *constrained evolution*. In this context, the time evolution of constraint equations can be tested to monitor numerical accuracy. After the initial data are set up, the evolution of the system in NR proceeds step by step in the time coordinate via numerical schemes such as the Runge-Kutta (RK) integrator. The most common approach consists of discretising spacetime into a grid and solving differential equations with finite differences. An adaptive mesh refinement (AMR) module is often applied to the grid in order to increase resolution where needed while limiting the computational costs.

The ADM metric can be simplified by imposing an approximate gauge condition referred to as the conformally flat condition (CFC), belonging to the class of fully constrained formulations Pili et al. (2017b). This first involves applying a conformal decomposition to the spatial metric γ_{ij}, which is rewritten in terms of a conformal factor ψ and the conformally related metric $\bar{\gamma}_{ij}$ as

$$\gamma_{ij} = \psi^4 \ \bar{\gamma}_{ij} \ . \tag{2.13}$$

The conformal factor ψ is a positive scalar function of space and time and describes the overall scale of the distance in the curved space compared to the flat space manifold. Additionally, the conformally related metric is required to be flat, so that

$$\gamma_{ij} = \psi^4 \ f_{ij} \ , \tag{2.14}$$

where f_{ij} is a time-independent flat background metric. This gauge choice is physically motivated by the general observation that in BNS systems the amount of energy radiated away in the form of GW emission per orbit during the inspiral only represents a very small fraction of the total orbital energy of the system. It is well applicable to scenarios where the gravitational field is strong, but the loss of energy due to gravitational radiation is negligible, such as in isolated NSs or during the early inspiral of BNS systems.

Applying the CFC approximation to each space-like manifold has the advantage of considerably simplifying the solution to the field equations. In fact, all the constraint equations derived from Einstein field equations in the ADM formalism reduce to effective flat-space elliptic equations, which are tractable in NR through standard numerical techniques. Moreover, the CFC approximation has been proven to yield stable long-term evolutions for compact objects in astrophysical settings (see e.g. Dimmelmeier et al. (2001), Abdikamalov et al. (2009)).

However, as a direct consequence of its definition, the CFC approximation is an inherently waveless approximation, which means that it hinders any explicit manifestation of gravitational radiation. Another issue concerning the CFC approximation and, more in general, constrained formulations, lies in the mathematical non-uniqueness of the solution when dealing with highly compact configurations such as nascent BHs. The uniqueness problem stems from the non-linearity of the constraint equations and has prevented successful application of constrained formulations to a wide range of astrophysical contexts. This obstacle was addressed by Cordero-Carrión et al. (2009), who presented a reformulation of the CFC approximation known as extended CFC (XCFC). In Cordero-Carrión et al. (2009), the revised XCFC scheme is numerically tested and proven to fully heal the uniqueness issue, which appeared in the original CFC formulation as convergence to an unphysical solution or even complete non-convergence.

In recent years, substantial progress has been achieved in simulations of BNS systems, with current models including a detailed description of intrinsic magnetic fields and micro-physics effects such as neutrino transport. In particular, incorporating the treatment of intrinsic magnetic fields shed light on the magnetic stability of NSs. Numerical results provided evidence in support of the hypothesis that any realistic long-lived magnetic field configuration must exhibit a mixed topology, involving a combination of both poloidal and toroidal components Braithwaite & Spruit (2004). Moreover, GRMHD simulations allowed exploration of the accretion process and characterisation of the mechanism behind jet formation for short gamma-ray bursts. A comprehensive overview of the state-of-the-art in BNS simulations is presented in Kiuchi (2024).

Chapter 3

FIRST-ORDER TIDAL FIELD PERTURBATIONS

This chapter contains a comprehensive analytic treatment of the first-order perturbation originating from an external tidal field. The analytical framework follows the structure of the work by Hinderer (2008), reproducing and extending the published results. Section 3.1 lays the foundation for the subsequent analytical computations by providing a rigorous definition of the tidal deformability in full GR and introducing the reader to the spherical harmonics decomposition in Subsection 3.1.1. In Section 3.2 the main body of the calculation is reported in detail. The numerical results obtained are presented and discussed in Section 3.3. Unless otherwise specified, geometrised units are adopted, according to which the speed of light c and the gravitational constant G are set to unity ($c = G = 1$).

3.1 DEFINITION OF λ IN FULL RELATIVITY

Consider a static and spherically symmetric star of mass M placed in an external static field $\mathcal{E}_{ij}$ of quadrupolar nature. As discussed in Section 2.3, the case of major astrophysical relevance is when the external tidal field acting upon the NS is represented by the gravitational field of the companion object in a binary system. Nevertheless, in the most generic situation, the perturbing tidal field can be of any nature: this justifies the choice of investigating isolated NSs before adding further complexity to the system. As a response, the star develops a quadrupole moment Q_{ij}. The induced quadrupolar deformation of the star can be described in terms of the spherical harmonic modes with $l = 2$.

Since we are interested in the treatment of fully relativistic stars, the Newtonian expressions in Equation (2.5) and Equation (2.6) cannot be applied. In the strong-field regime, it is still possible to define the moments Q_{ij} and $\mathcal{E}_{ij}$ through an asymptotic expansion of the metric. In the asymptotically flat region - that is, at large values of the radial coordinate r - in the local asymptotic rest frame of the star, the g_{tt} metric coefficient is given by Thorne (1998) as

$$\begin{aligned} \frac{1+g_{tt}}{2} = \frac{M}{r} + \frac{3Q_{ij}}{2r^3}\left(n^i n^j - \frac{1}{3}\delta^{ij}\right) + O\left(\frac{1}{r^4}\right) \\ - \frac{1}{2}\mathcal{E}_{ij}x^i x^j + O(r^3)\ , \end{aligned} \tag{3.1}$$

where $\vec{n} = (\sin\theta\cos\phi, \sin\theta\sin\phi, \cos\theta)$ is the unit vector in spherical polar coordinates and hence $n^i = x^i/r$. Note that the term $\left(n^i n^j - \frac{1}{3}\delta^{ij}\right)$ is a symmetric trace-free (STF) combination that ensures the resulting tensor to be STF itself. In this case, since Q_{ij} is STF already, the delta function is not actively involved in the computation and can be dropped without consequences.

We are interested in working to linear order in $\mathcal{E}_{ij}$ and in the limit where the source of $\mathcal{E}_{ij}$ is very distant from the star. Under these assumptions, any ambiguity possibly arising from performing an asymptotic expansion of the metric vanishes. It is relevant to notice that assuming the external field to be placed far away from the star corresponds, in the binary evolution picture, to restricting our analysis to the early inspiral phase. At this stage, the orbital separation is not too small and changes in the internal structure occur on timescales much longer than the orbital period. In this context, the static response approximation imposed here is appropriate. However, it is important to mention that as the separation shrinks due to GW emission, the spacetime becomes highly dynamical and the effect of dynamical tides becomes significant. Therefore, accurate modelling of the gravitational waveform emitted during the late inspiral requires the inclusion of higher-order dynamical effects.

From the definition of tidal deformability in Equation (2.2), the quadrupolar response of the star is related to the external perturbing tidal field according to

$$Q_{ij} = -\lambda\mathcal{E}_{ij}\ , \tag{3.2}$$

where the parameter λ is constant and related to the dimensionless $l = 2$ tidal Love number k_2 according to Equation (2.7).

3.1.1 SPHERICAL HARMONICS DECOMPOSITION

Assuming spherical symmetry, the tensor moments Q_{ij} and $\mathcal{E}_{ij}$ can be decomposed using a multipole expansion in a basis of orthonormal tensor spherical harmonics, obtaining

$$Q_{ij} = \sum_{m=-2}^{2} Q_m\ \mathcal{Y}^{2m}_{ij} \qquad\qquad \mathcal{E}_{ij} = \sum_{m=-2}^{2} \mathcal{E}_m\ \mathcal{Y}^{2m}_{ij} \qquad . \tag{3.3}$$

The STF tensor-harmonic basis functions $\mathcal{Y}^{2m}_{ij}$ are defined by Thorne (1980) as

$$Y_{2m}(\theta,\phi) = \mathcal{Y}^{2m}_{ij}n^i n^j\ . \tag{3.4}$$

In Equations (3.3), index l is fixed to $l = 2$, which corresponds to a tensor perturbation of quadrupolar nature. The perturbations associated with the monopole ($l = 0$) and the dipole ($l = 1$) configurations do not show up because the lowest order contribution to GW generation is the quadrupolar one.

In light of Equations (3.3), Equation (3.2) can be rewritten as

$$\begin{aligned}\sum_{m=-2}^{2} Q_m \, \mathcal{Y}^{2m}_{ij} &= -\lambda \sum_{m=-2}^{2} \mathcal{E}_m \, \mathcal{Y}^{2m}_{ij} \\ &= -\sum_{m=-2}^{2} \lambda \, \mathcal{E}_m \, \mathcal{Y}^{2m}_{ij} \qquad (3.5)\end{aligned}$$

and simplifying term by term it is immediate to obtain

$$Q_m = -\lambda \mathcal{E}_m \; . \qquad (3.6)$$

Fixing $l = 2$, the m number could in principle take the values $0, \pm 1, \pm 2$. However, in non-rotating objects there is full degeneracy between all values of m so it is possible to fix $m = 0$ without loss of generality. This choice corresponds to the axially symmetric case, meaning that the system is symmetric along the azimuthal direction. This removes any dependence on the angular coordinate ϕ and for this reason it would be possible to replace $Y_{20}(\theta, \phi)$ with the Legendre polynomial $P_2(\cos\theta)$ in the spherical harmonic decomposition. In fact, in the case of azimuthal symmetry, the two functions differ by a constant factor that does not affect the physics of the system.

3.2 CALCULATION OF THE LOVE NUMBER

This section is dedicated to the calculation of the Love number and is organised as follows. Subsection 3.2.1 outlines the motivation for using `Mathematica` as a computational tool for performing tensorial calculations in GR; Subsection 3.2.2 describes the equilibrium configuration of the NS; Subsection 3.2.3 presents the analytical framework of metric perturbation theory, focusing on the introduction of a first-order tidal perturbation to the background spacetime; Subsection 3.2.4 derives the solution for the perturbation in the external region to the star; Subsection 3.2.5 addresses the numerical computation of the Love number; finally, Subsection 3.2.6 examines the Newtonian limit of the result.

3.2.1 METHOD

The analytical computations reported in this section have been carried on within the framework of `Wolfram Mathematica`. `Mathematica` is a vast software system including over 6000 built-in functions covering all areas of technical computing, such as geometry, statistics, symbolic computation, data science, time series analysis, visualizations, and even machine learning, including neural networks and image processing. It is based on the `Wolfram` language and uses the `Wolfram Notebook` interface, which allows the user to organise and enrich the documents including text, runnable code, and dynamic graphics. The choice of using `Mathematica` is motivated by both its very intuitive and user-friendly interface and its ability to handle large-scale problems with numerical techniques such as parallelism and Graphics Processing Unit (GPU) computing.

Additionally, `Mathematica` is equipped with a modern `O`bject-oriented `G`eneral `Re`lativity (`OGRe`) package for tensor calculus Shoshany (2021). This package is instrumental in performing tensor calculations in a variety of contexts ranging from physics to mathematics and is especially suitable for GR. Possible operations include addition of tensors, multiplication of tensor by scalar, trace, contraction, and both partial and covariant derivatives. Another useful feature in the framework of this project is that `OGRe` allows the direct extraction, for a given metric, of the associated set of Christoffel symbols.

3.2.2 Equilibrium configuration

The background metric associated to a static, spherically symmetric spacetime can be described by the generic line element

$$\begin{aligned} ds_0^2 &= g^{(0)}_{\alpha\beta}\, dx^\alpha dx^\beta \\ &= -e^{\nu(r)}dt^2 + e^{\lambda(r)}dr^2 + r^2(d\theta^2 + \sin^2\theta d\phi^2)\ . \end{aligned} \tag{3.7}$$

The equilibrium stellar model is obtained by numerical integration of the TOV equations Oppenheimer & Volkoff (1939)

$$\frac{dm}{dr} = 4\pi r^2\rho \tag{3.8}$$

$$\frac{dp}{dr} = -(p+\rho)\frac{4\pi r^3 p + m}{r(r-2m)} \tag{3.9}$$

$$\frac{d\nu}{dr} = -\frac{2}{p+\rho}\frac{dp}{dr} \tag{3.10}$$

supplemented with an EOS for NS matter. Here, the EOS is approximated by a polytropic relation linking pressure p and density ρ as in Equation (2.1). For a complete derivation of TOV equations (3.8), (3.9), (3.10), refer to Appendix A.

3.2.3 Static tidal perturbations

Let us consider the first-order perturbation caused by the presence of an external static tidal field and describe its effect on the equilibrium configuration. Analytical computations are performed within the framework of linearised perturbation theory following the method carried out by Thorne & Campolattaro (1967).

The full metric describing the perturbed spacetime is defined as the superposition of a linearised small perturbation to the background metric

$$g_{\alpha\beta} = g^{(0)}_{\alpha\beta} + h_{\alpha\beta}\ . \tag{3.11}$$

The metric perturbation $h_{\alpha\beta}$ incorporates an angular dependence, which is treated according to the spherical-harmonic decomposition as in Regge & Wheeler (1957). As already specified in Subsection 3.1.1, the following analysis is restricted to the quadrupolar perturbation, corresponding to $l = 2$ in the spherical-harmonic expansion, and to the axially symmetric non-rotating case, corresponding to $m = 0$. We also restrict to static (not frequency dependent) and even-parity perturbations treated in the Regge-Wheeler gauge, a choice that reflects the spherical symmetry of the background spacetime Regge & Wheeler (1957). Using letters a, b to denote temporal and radial coordinates $\{t, r\}$, and capital letters A, B for the angular coordinates $\{\theta, \phi\}$, the Regge-Wheeler gauge implies that the even-parity part of h_{aA} and the entire tensorial (trace-free) part of h_{AB} are set to zero. In this way, the perturbation ends up having a simple structure: an even-parity sector with four scalar modes (3 in h_{ab} and 1 in h_{AB}); an odd-parity sector with two vector modes (h_{aA}).

Under these assumptions, the metric perturbation takes the form

$$h_{\alpha\beta} = \begin{pmatrix} -e^{\nu} H_0(r) & 0 & 0 & 0 \\ 0 & e^{\lambda} H_2(r) & 0 & 0 \\ 0 & 0 & r^2 K(r) & 0 \\ 0 & 0 & 0 & r^2 \sin^2\theta K(r) \end{pmatrix} Y_{20}(\theta, \phi) \tag{3.12}$$

In order to assess the effects of the perturbation on the equilibrium configuration we need to construct the Einstein field equations in linearised theory

$$\delta G^{\alpha}_{\beta} = 8\pi \delta T^{\alpha}_{\beta} \ , \tag{3.13}$$

where $\delta G^{\alpha}_{\beta}$ is the linear perturbation to the Einstein tensor G^{α}_{β} while $\delta T^{\alpha}_{\beta}$ is the linear perturbation to the stress-energy-momentum tensor T^{α}_{β}. The mixed index notation is applied to simplify computations. On the right-hand side of Equation (3.13), the source term refers to NS matter, which is described here as a perfect fluid.

The stress-energy tensor for a perfect fluid is defined as

$$T_{\alpha\beta} = (p + \rho) u_{\alpha} u_{\beta} + p g^{(0)}_{\alpha\beta} \ , \tag{3.14}$$

where $u^{\alpha} = (e^{-\nu(r)/2}, 0, 0, 0)$ is the four-velocity of the fluid while p and ρ represent, respectively, the pressure and the density of the fluid. The only non-vanishing components of the first-order perturbation to the stress-energy tensor are $\delta T^0_0 = -\delta\rho = -(dp/d\rho)^{-1}\delta p$ and $\delta T^i_i = \delta p$.

On the left-hand side of Einstein equations, the Einstein tensor is defined as

$$G_{\alpha\beta} = R_{\alpha\beta} - \frac{1}{2} g_{\alpha\beta} R \ , \tag{3.15}$$

where the Ricci tensor $R_{\alpha\beta}$ and the Ricci scalar R are defined by the following contractions of the Riemann tensor $R^{\mu}_{\alpha\nu\beta}$

$$R_{\alpha\beta} \equiv R^{\mu}_{\alpha\mu\beta} \qquad\qquad R \equiv R^{\alpha}_{\alpha} = g^{\alpha\beta} R_{\alpha\beta} \quad , \tag{3.16}$$

$$\tag{3.17}$$

$$\text{where} \quad R^{\mu}_{\alpha\nu\beta} = \partial_{\nu}\Gamma^{\mu}_{\alpha\beta} - \partial_{\beta}\Gamma^{\mu}_{\alpha\nu} + \Gamma^{\mu}_{\nu\lambda}\Gamma^{\lambda}_{\alpha\beta} - \Gamma^{\mu}_{\beta\lambda}\Gamma^{\lambda}_{\alpha\nu} \tag{3.18}$$

$$\text{with} \quad \Gamma^{\sigma}_{\alpha\beta} := \frac{1}{2} g^{\sigma\lambda}(\partial_{\alpha} g_{\lambda\beta} + \partial_{\beta} g_{\alpha\lambda} - \partial_{\lambda} g_{\alpha\beta}) \ . \tag{3.19}$$

The linearised Einstein equations in Equation (3.13) are solved by exploiting convenient combinations of the various components. Solving $\delta G^{\theta}_{\theta} - \delta G^{\phi}_{\phi} = 8\pi(\delta T^{\theta}_{\theta} - \delta T^{\phi}_{\phi}) = 8\pi(\delta p - \delta p) = 0$ yields the constraint

$$H_0(r) = -H_2(r) \equiv H(r) \ . \tag{3.20}$$

By enforcing diagonality with the condition $\delta G^r_\theta = 8\pi\delta T^r_\theta = 0$ it is possible to relate $K'(r)$ to $H(r)$ in the following way

$$K'(r) = -H'(r) - H(r)\nu'(r) \ . \tag{3.21}$$

The combination of the angular components $\delta G^\theta_\theta + \delta G^\phi_\phi = 8\pi(\delta T^\theta_\theta + \delta T^\phi_\phi) = 16\pi\delta p$ can be used to express δp as a function of $H(r)$, $\lambda'(r)$ and $\nu'(r)$. Then, from the subtraction $\delta G^r_r - \delta G^t_t = 8\pi(\delta T^r_r - \delta T^t_t)$ one obtains a second-order differential equation for the function $H(r)$

$$\begin{aligned} H''(r) + H'(r)\left[\frac{2}{r} + e^{\lambda(r)}\left(\frac{2m(r)}{r^2} + 4\pi r(p-\rho)\right)\right] & \\ + H(r)\left[-\frac{6e^{\lambda(r)}}{r^2} + 4\pi e^{\lambda(r)}\left(5\rho + 9p + \frac{p+\rho}{dp/d\rho}\right) - \nu'^{\,2}\right] &= 0 \ . \end{aligned} \tag{3.22}$$

The boundary conditions for Equation (3.22) can be obtained by requiring regularity of $H(r)$ at $r = 0$ and solving for $H(r)$ there. The approach here is to make an ansatz over $H(r)$, decomposing it as the sum of several terms of increasing power of r. Then, in order for Equation (3.22) to be valid, the coefficient of each term must vanish. The asymptotic expansion obtained in this way is

$$H(r) = a_0 r^2 - a_0 r^4\left[\frac{2}{7}\pi\left(11p(0) + \frac{1}{3}\rho(0) + \frac{p(0)+\rho(0)}{(dp/d\rho)(0)}\right)\right] + O(r^5) \ . \tag{3.23}$$

3.2.4 EXTERIOR SOLUTION

Outside the star of radius R, the mass function $m(r > R)$ corresponds to the total mass of the star $m(R) \equiv M$, while the fluid pressure and density go to zero: $p(r > R) = 0$, $\rho(r > R) = 0$. Therefore, the differential equation (3.22) reduces to

$$H''(r) + \left(\frac{2}{r} - \lambda'(r)\right)H'(r) - \left(\frac{6e^{\lambda(r)}}{r^2} + \lambda'(r)^2\right)H(r) = 0 \ . \tag{3.24}$$

Moreover, the background metric outside the star reduces to the exterior Schwarzschild solution

$$ds^2 = -\left(1 - \frac{2M}{r}\right)dt^2 + \left(1 - \frac{2M}{r}\right)^{-1}dr^2 + r^2(d\theta^2 + \sin^2\theta d\phi^2) \ , \tag{3.25}$$

so it is possible to match the two expressions Equation (3.7) and Equation (3.25) to compute the metric function $\lambda(r)$. Outside the star,

$$e^\lambda(r) = \frac{1}{1 - \frac{2M}{r}} \qquad \Rightarrow \qquad \lambda(r) = \ln\left(\frac{1}{1 - \frac{2M}{r}}\right) \ . \tag{3.26}$$

Let us manipulate Equation (3.24) by imposing the change of variables $r \to M(1 + x)$ as in Thorne & Campolattaro (1967). In the new variable, Equation (3.24) takes the form of the associated Legendre equation [1] with $l = m = 2$

$$(x^2 - 1)H''(x) + 2xH'(x) - \left(6 + \frac{4}{x^2 - 1}\right)H(x) = 0 \ . \tag{3.27}$$

---

[1] The general Legendre equation for a function $f(x)$ takes the form:
$(x^2 - 1)f''(x) + 2xf'(x) - \left(l(l+1) + \frac{m^2}{x^2-1}\right)f(x) = 0$.

Equation (3.27) can be solved to retrieve the exterior solution for $H(r)$, which is expressed as a linear combination of the $l = m = 2$ associated Legendre functions $P_2^2(x)$ and $Q_2^2(x)$

$$H(x) = c_1 P_2^2(x) + c_2 Q_2^2(x) \ . \tag{3.28}$$

Restoring the r variable in Equation (3.28) it is immediate to obtain

$$\begin{aligned} H(r) = 3\ c_1 &\left(\frac{r}{M}\right)^2 \left(-1 + \frac{2M}{r}\right) \\ &+ c_2 \left(\frac{r}{M}\right)^2 \left(-1 + \frac{2M}{r}\right) \left[\frac{M(M-r)\left(2M^2 + 6Mr - 3r^2\right)}{r^2(2M-r)^2} + \frac{3}{2}\ln\left(\frac{r}{r-2M}\right)\right] \ . \end{aligned} \tag{3.29}$$

The asymptotic behaviour of Equation (3.29) at large r reads

$$H(r) = -3\left(\frac{r}{M}\right)^2 c_1 + O\left(\left(\frac{r}{M}\right)^3\right) - \frac{8}{5}\left(\frac{M}{r}\right)^3 c_2 + O\left(\left(\frac{M}{r}\right)^4\right) \ . \tag{3.30}$$

The coefficients c_1 and c_2 can be determined by matching the asymptotic solution in Equation (3.30) to the expansion from Equation (3.1) and using Equation (3.6).
Starting from Equation (3.1), focus on its left-hand side

$$g_{tt} = -e^{\nu(r)} - e^{\nu(r)} H(r) Y_{20}(\theta, \phi) \ , \tag{3.31}$$

where, since we are considering the exterior solution,

$$e^{\nu(r)} = \left(1 - \frac{2M}{r}\right) \ . \tag{3.32}$$

Multiplying $e^{\nu(r)}$ with $H(r)$ produces higher-order terms that are absorbed inside $O\left(\frac{1}{r^3}\right)$ and $O(r^3)$. Therefore,

$$\begin{aligned} g_{tt} &= -\left(1 - \frac{2M}{r}\right) - H(r)Y_{20}(\theta, \phi) \\ \frac{1 + g_{tt}}{2} &= \frac{1}{2}\left(1 - 1 + \frac{2M}{r} - H(r)Y_{20}(\theta, \phi) + O\left(\frac{1}{r^4}\right)\right) \\ &= \frac{M}{r} - \frac{1}{2}H(r)Y_{20}(\theta, \phi) + O\left(\frac{1}{r^4}\right) \\ &= \frac{M}{r} - \frac{1}{2}Y_{20}(\theta, \phi)\left[-3\left(\frac{r}{M}\right)^2 c_1 + O\left(\left(\frac{r}{M}\right)^3\right) - \frac{8}{5}\left(\frac{M}{r}\right)^3 c_2 + O\left(\left(\frac{M}{r}\right)^4\right)\right] \ . \end{aligned} \tag{3.33}$$

By comparing Equation (3.1) to Equation (3.33) one obtains

$$\frac{M}{r} + \frac{3}{2}\frac{Q_{ij}n^i n^j}{r^3} - \frac{1}{2}\mathcal{E}_{ij}n^i n^j r^2 = \frac{M}{r} - Y_{20}(\theta, \phi)\left[-\frac{3}{2}\left(\frac{r}{M}\right)^2 c_1 - \frac{8}{10}\left(\frac{M}{r}\right)^3 c_2\right] \ . \tag{3.34}$$

From Equation (3.3) and Equation (3.4)

$$Q_{ij}n^in^j = \sum_{m=-2}^{2} Q_m \ \mathcal{Y}^{2m}_{ij} n^i n^j = \sum_{m=-2}^{2} Q_m \ Y_{2m}(\theta, \phi) \ . \tag{3.35}$$

Assuming axial symmetry and fixing $m = 0$, Equation (3.35) can be rewritten as

$$Q_{ij}n^in^j = Q \ Y_{20}(\theta, \phi) \ . \tag{3.36}$$

Similarly, the external tidal field term can be rewritten as

$$\frac{1}{2}\mathcal{E}_{ij}x^ix^j = \frac{1}{2}\mathcal{E}_{ij}n^in^jr^2 = \frac{1}{2}\mathcal{E}r^2 \ Y_{20}(\theta, \phi) \ . \tag{3.37}$$

Therefore,

$$\frac{M}{r} + \frac{3}{2}\frac{Q \ Y_{20}(\theta, \phi)}{r^3} - \frac{1}{2}\mathcal{E}r^2 \ Y_{20}(\theta, \phi) = \frac{M}{r} - Y_{20}(\theta, \phi)\left[-\frac{3}{2}\left(\frac{r}{M}\right)^2 c_1 - \frac{8}{10}\left(\frac{M}{r}\right)^3 c_2\right] \ . \tag{3.38}$$

By direct comparison between the corresponding terms on the left and right-hand sides of Equation (3.38) it is immediate to retrieve

$$c_1 = -\frac{1}{3}M^2\mathcal{E} \qquad\qquad c_2 = -\frac{15}{8}\frac{1}{M^3}\lambda\mathcal{E} \quad . \tag{3.39}$$

The values here obtained for the coefficients c_1 and c_2 are negative and opposite in sign with respect to the corresponding values reported by Hinderer (2008). However, this does not represent an issue, as it does not reflect any physical discrepancy. In fact, in the linear combination of two linearly independent solutions, the negative common sign can be factored out and absorbed by an appropriate redefinition of the coefficients c_1 and c_2 without changing the physical content of the solution. Moreover, in the framework of tidal deformability computations, physically relevant quantities such as the Love number only depend on the ratio between the two coefficients. Therefore, a global sign variation in both c_1 and c_2 does not affect the final results.

3.2.5 NUMERICAL SOLUTION

At this point, all the necessary ingredients are available to numerically solve the second-order differential equation (3.22) for the metric perturbation $H(r)$. To do so, it is first required to construct numerical functions for the pressure $p(r)$, mass density $\rho(r)$ and mass function $m(r)$ by solving the system of Tolman-Oppenheimer-Volkoff (TOV) equations (3.8), (3.9), (3.10) coupled with a polytropic model for the EOS.

With the aim of solving for $H(r)$, Equation (3.22) is rearranged into a system of two first-order differential equations involving the variables $H(r)$ and $\beta(r) := H'(r)$

$$\begin{cases} \beta'(r) + \beta(r)\left[\frac{2}{r} + e^{\lambda(r)}\left(\frac{2m(r)}{r^2} + 4\pi r(p-\rho)\right)\right] \\ \qquad\qquad +H(r)\left[-\frac{6e^{\lambda(r)}}{r^2} + 4\pi e^{\lambda(r)}\left(5\rho + 9p + \frac{p+\rho}{dp/d\rho}\right) - \nu'^{\,2}\right] = 0 \\ H'(r) = \beta(r) \end{cases} \tag{3.40}$$

The initial conditions are set on the basis of the asymptotic expansion at small r in Equation 3.23 and read

$$H(r_0) = a_0 r^2 \qquad\qquad \beta(r_0) = 2a_0 r_0 \ . \tag{3.41}$$

Then, the first-order system for $H(r)$ and $\beta(r)$ in Equation (3.40) is solved by numerical integration from the centre of the star ($r = 0$) outwards. It is convenient to define the new variable

$$y \equiv \frac{R\ H'(R)}{H(R)} \ . \tag{3.42}$$

The numerical value for the y variable obtained from numerical integration of Equation (3.40) is matched with the corresponding analytical expression computed from the exterior solution (Equation (3.24)). In this way, it is possible to compute the tidal deformability parameter λ. Then, exploiting the relation between the tidal deformability and the Love number expressed in Equation (2.7), it is possible to write an analytical expression for the Love number k_2

$$\begin{aligned} k_2 = &\left[\frac{8}{5}C^5(1-2C)^2[2-y+2C(y-1)]\right] \times \\ &\Bigg\{2C[6-3y+3C(5y-8)] + 4C^3[13-11y+C(3y-2)+2C^2(1+y)] + \\ &+ 3(1-2C)^2[2-y+2C(y-1)]\log(1-2C)\Bigg\}^{-1} \ , \end{aligned} \tag{3.43}$$

where $C \equiv M/R$ is the star's compactness parameter.

3.2.6 NEWTONIAN LIMIT

General relativity reduces to Newton's theory of gravity in the limit of weak gravitational fields and low velocities. Formally, these assumptions correspond to

$$v \ll c \ \Rightarrow \ v \ll 1 \qquad \text{and} \qquad \Phi \ll 1 \ , \tag{3.44}$$

where the speed of light is set to $c = 1$ in geometrised units while Φ represents the gravitational potential in Newtonian theory. It can be shown that in the Newtonian limit (that is, when Equation (3.44) holds), Einstein's field equations reduce to Poisson's equation for gravity

$$\Delta\Phi = 4\pi G_N \rho \ , \tag{3.45}$$

where G_N is the Newtonian gravitational constant and ρ is the matter density. Equation (3.45) is equivalent to Newton's law, which demonstrates that the theory of general relativity correctly reproduces the Newtonian results in the non-relativistic regime.

In particular, it is also true that the first term in the expansion of Equation (3.43) in the compactness parameter M/R reproduces the Newtonian result

$$k_2^N = \frac{1}{2}\left(\frac{2-y}{3+y}\right) \ . \tag{3.46}$$

In the Newtonian limit, the differential equation (3.22) inside the star becomes

$$H''(r) + \frac{2}{r}H'(r) + \left(\frac{4\pi\rho}{dp/d\rho} - \frac{6}{r^2}\right)H(r) = 0 \ . \tag{3.47}$$

Assuming a polytropic index of $n = 1$, Equation (3.47) can be rewritten in the form of a Bessel equation through the following steps.
First, let us recall that for a polytropic EOS

$$p = K\rho^{\Gamma} \qquad \Rightarrow \qquad \frac{dp}{d\rho} = K\Gamma\rho^{\Gamma-1} \ , \tag{3.48}$$

therefore it is possible to rewrite

$$\frac{4\pi\rho}{dp/d\rho} = \frac{4\pi\rho}{K\Gamma\rho^{\Gamma-1}} = \frac{4\pi}{K\Gamma}\rho^{2-\Gamma} = \text{constant} \equiv k \qquad \text{if} \quad n = 1 \ (\Gamma = 2) \ . \tag{3.49}$$

It is also convenient to introduce the dimensionless variable $x = \pi r/R$, where R represents the characteristic length scale of the system, in this case being the NS radius. According to the chain rule, derivatives transform as

$$\frac{dH}{dr} = \frac{dH}{dx}\frac{dx}{dr} = \frac{\pi}{R}\frac{dH}{dx}, \qquad \frac{d^2H}{dr^2} = \left(\frac{\pi}{R}\right)^2 \frac{d^2H}{dx^2} \ . \tag{3.50}$$

Applying these substitutions to Equation (3.47) leads to

$$\begin{aligned}
\left(\frac{\pi}{R}\right)^2 \frac{d^2H}{dx^2} + \frac{2}{r}\frac{\pi}{R}\frac{dH}{dx} + \left(k - \frac{6}{r^2}\right)H(x) = 0 \\
\left(\frac{\pi}{R}\right)^2 \frac{d^2H}{dx^2} + \frac{2\pi}{Rx}\frac{\pi}{R}\frac{dH}{dx} + \left(k - \frac{6\pi^2}{(Rx)^2}\right)H(x) = 0 \\
\frac{d^2H}{dx^2} + \frac{2}{x}\frac{dH}{dx} + \left(\frac{R^2}{\pi^2}k - \frac{6}{x^2}\right)H(x) = 0 \ .
\end{aligned} \tag{3.51}$$

Near the centre of the star ($r \to 0$, or equivalently $x \to 0$), the term $6/x^2$ dominates, so Equation (3.51) simplifies to

$$\frac{d^2H}{dx^2} + \frac{2}{x}\frac{dH}{dx} - \frac{6H}{x^2} = 0 \ , \tag{3.52}$$

which can be rearranged as

$$x^2\frac{d^2H}{dx^2} + 2x\frac{dH}{dx} + (x^2 - 6)H = 0 \ . \tag{3.53}$$

Equation (3.53) is written in the standard form of a Bessel differential equation

$$x^2y'' + xy' + (x^2 - \alpha^2)y = 0 \ , \tag{3.54}$$

where the arbitrary complex number α indicates the order of the Bessel functions $y(x)$ that are canonical solutions of Equation (3.54), and here takes the value $\alpha = \sqrt{6} = 5/2$.
The solution of Equation (3.53) that ensures regularity at the origin is Abramowitz & Stegun (1964)

$$H(x) = A \ J_{5/2}(x) \ , \tag{3.55}$$

where A is a constant. Restoring the original radial coordinate r, the solution for the H function is given by

$$H(r) = A \left(\frac{r}{R}\right)^{1/2} J_{5/2}\left(\frac{\pi r}{R}\right) \ . \tag{3.56}$$

When the $H(r)$ function is written in this form, at $r = R$ the y variable becomes $y \equiv RH'(R)/H(R) = \frac{1}{3}(\pi^2 - 6)$. One can substitute this expression for y in Equation (3.46) to compute the Newtonian value for the Love number, thereby obtaining

$$k_2^N(n=1) = \frac{1}{2}\left(\frac{12-\pi^2}{3+\pi^2}\right) \approx 0.0828 \ . \tag{3.57}$$

3.3 Numerical results

This section is dedicated to the presentation of numerical results obtained for the tidal Love number k_2. The system of TOV equations (3.8), (3.9), (3.10) coupled with a polytropic EOS in the form of Equation (2.1) has been numerically solved for different values of the polytropic index n and the compactness parameter C. In this way, interpolated numerical functions have been constructed for the mass, pressure and internal energy density of the NS as a function of the stellar radius. The numerical method used is described in Subsection 3.3.1, while the behaviour of the resulting interpolated functions is discussed in Subsection 3.3.2.

Inserting the numerically interpolated functions into Equation (3.40) allowed to solve for $H(r)$ and $\beta(r)$. Computing their numerical values at the star radius $H(R)$ and $\beta(R)$ enabled the numerical computation of $y \equiv RH'(R)/H(R)$, which eventually led to a numerical solution for k_2 through Equation (3.43).

Subsection 3.3.3 is dedicated to the analysis of the behaviour of the Love number for a variety of different n and C configurations, while Subsection 3.3.4 discusses the implication that the numerical results of the Love number have on the dimensionless tidal deformability parameter. Finally, Subsection 3.3.5 quantifies and comments on the deviation of general relativistic results from those obtained in a Newtonian framework.

3.3.1 Method

The numerical solution to the first-order differential system in Equation (3.40) has been obtained implementing numerical methods in the `Python` programming language. In order to numerically reconstruct the radial behaviour of the mass function, pressure and energy density of the star, the code solves for the equilibrium configuration of the NS assuming a polytropic EOS. The solver has been built upon the `Rounakrik_TOV_Solver` project[2], a public domain repository providing `Python` scripts for numerically solving the TOV equations coupled with various equations of state including piecewise, tabular and polytropic. The TOV solver exploits a fourth-order Runge-Kutta (RK4) integration scheme and, in this case, it required an auxiliary function to compute the central energy density given the polytropic index n and the target compactness C.

---

[2] The GitHub repository of the mentioned project is available at the following link: https://github.com/Rounakrik/TOV_Solver.

3.3.2 Interpolated functions

Numerical integration of TOV equations coupled with the EOS provides the equilibrium stellar model for the considered NS. The numerically interpolated functions generated in this way describe the radial behaviour of the mass function, pressure and energy density of the star in its equilibrium configuration. In particular, analysing the dependence of the mass function and pressure on the compactness parameter is instructive for inferring global properties on the NS structure. As a test case example, the polytropic index is fixed at $n = 1$.

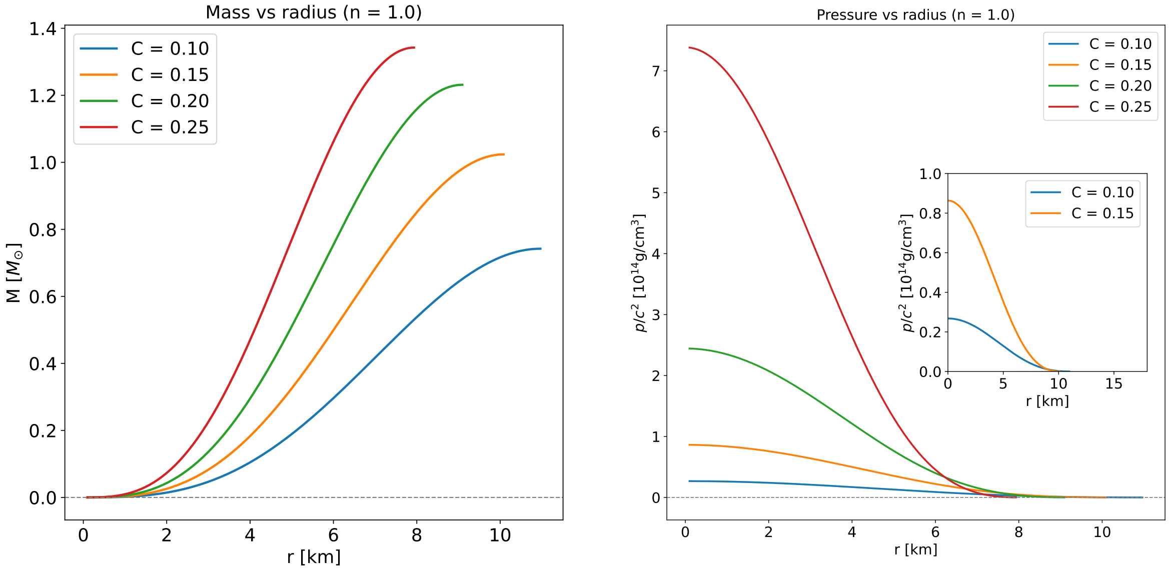

Figure 3.1: *Left-hand panel*: interpolated mass function for fixed polytropic index $n = 1$ and varying compactness C. As C increases, the mass function becomes steeper, implying that more compact NSs reach higher total masses within smaller radii. *Right-hand panel*: interpolated pressure function for fixed polytropic index $n = 1$ and varying compactness C. The inset plot provides a zoomed view along the $y-$axis to allow for a clearer visualisation of the pressure profile behaviour at smaller values of C. More compact NSs reach higher central pressure values and are characterised by a steeper pressure gradient.

The left-hand panel in Figure 3.1 clearly shows that, assuming the same EOS, more compact stars reach higher total masses and exhibit smaller radii. Conversely, less compact stars are less massive and more extended. This is expected, since higher compactness implies stronger gravitational binding and leads to a denser and more centrally condensed configuration. The mass distribution displays a steeper behaviour as the compactness increases, meaning that a larger fraction of the stellar mass is confined in the inner regions. As a consequence, more compact stars pack a larger amount of mass into a smaller volume, eventually leading to an increased central density.

Similarly, more compact stars reach higher central pressure and exhibit a steeper pressure gradient. This is because a more compact star requires a larger pressure gradient to counteract the stronger pull of gravity and maintain the configuration in hydrostatic equilibrium. The right-hand panel in

Figure 3.1 illustrates the behaviour of the pressure profile at varying compactness, and highlights that the central pressure in a NS with $C = 0.2$ can reach values one order of magnitude higher than those of a NS with $C = 0.1$.

3.3.3 Love number

According to Equation (3.43), the Love number k_2 is a function of both the polytropic index n, through the variable y, and the compactness $C = M/R$. These dependencies are illustrated in the three-dimensional surface plot in Figure 3.2, while representative numerical values obtained for k_2 with varying n and C are displayed in Table 3.1.

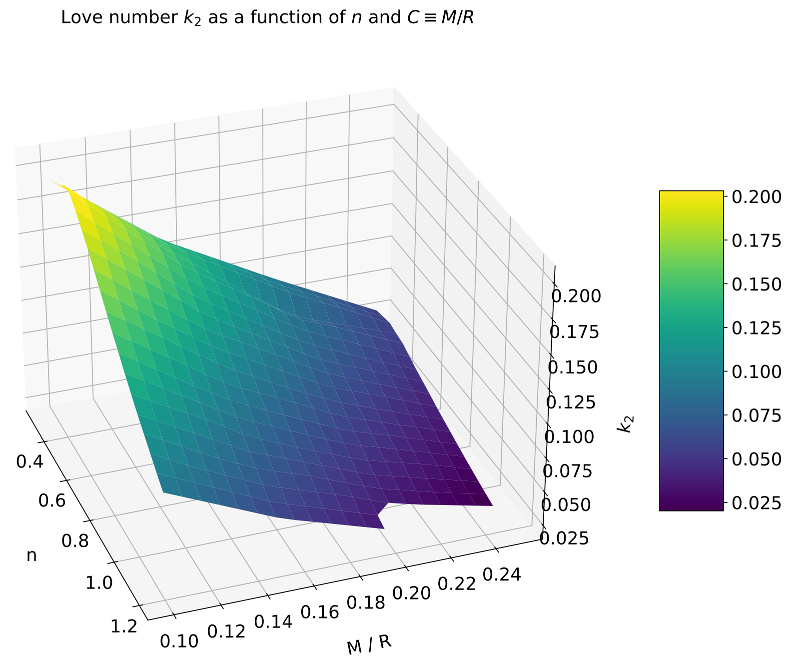

Figure 3.2: Surface plot for the relativistic Love number k_2 as a function of the polytropic index n and the compactness parameter $C = M/R$. The highest values of the Love number occur at low n and low C, implying that NSs endowed with a stiff EOS are the most subject to tidal deformations. Conversely, NSs with high n and high C have the lowest k_2 values and are therefore harder to deform.

Figure 3.2 shows that at high compactness, the Love number is small and variations in n do not significantly affect the final results for k_2. As extensively explained in Section 2.3, the polytropic index affects the internal mass distribution of the NS configuration. Therefore, this feature suggests that in the relativistic regime the gravitational binding dominates in determining the tidal response of the NS and its susceptibility to deformation. Instead, the internal mass distribution affected by n plays a secondary role compared to relativistic effects. Conversely, in less compact stars, the Love number varies significantly with n, meaning that the internal mass distribution has some relevance in governing the reaction of the star to an external perturbing tidal field.

The immediate implication of this feature is that the amount of EOS-related information that is possible to extract from the system is reduced in the case of more compact NSs, which all share a similar behaviour. On the other hand, Love number measurements in less compact stars are more informative about their underlying EOS.

The combined effect of n and C emphasises that the NS configurations that are the most subject to tidal deformation occur at low compactness and low n (stiff EOS), which corresponds to the upper left corner of the parameter space of the surface plot in Figure 3.2. On the other hand, the least deformable NSs occupy the lower right corner of the surface plot, being characterised by high compactness and high n (soft EOS).

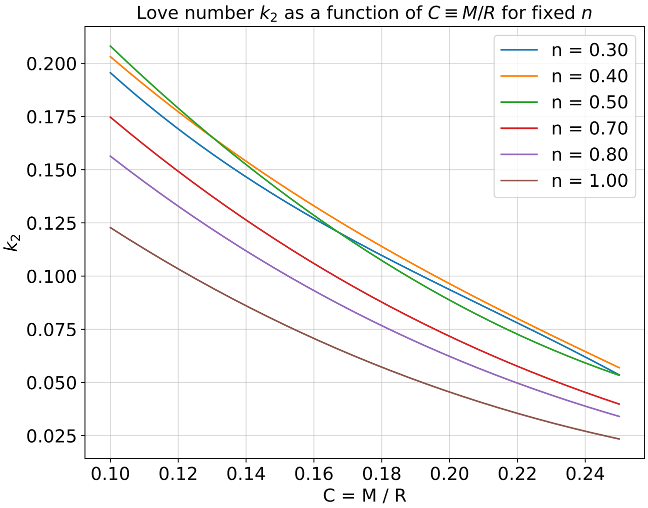

Figure 3.3: Relativistic Love number k_2 as a function of the compactness parameter $C = M/R$ for fixed values of n. All curves show a monotonically decreasing behaviour with C, which confirms that, given the same EOS, more compact stars are less deformable.

For a more immediate visualisation of the numerical results, it is instructive to slice the three-dimensional surface plot along the planes of constant n, thereby obtaining Figure 3.3. For all values of n, the Love number k_2 decreases monotonically with increasing C. This behaviour is expected because, as discussed in Subsection 3.3.2, given the same EOS, more compact stars are more gravitationally bound and therefore less responsive to tidal forces. From the slice plot in Figure 3.3 it emerges that the k_2 curves corresponding to higher n values lie systematically below the curves associated with lower n values. In fact, NSs with a higher polytropic index n are more centrally condensed and more resistant to tidal field perturbations, thereby resulting in overall lower values of the Love number.

It is interesting to note the occurrence of curves crossing for small n values. This behaviour suggests that the effects of the polytropic index n and the compactness C are not completely isolated from each other, but rather interdependent in determining the structure of the star.

However, the crossing of the curves may also be influenced by numerical artifacts inherent in the computational method. Therefore, while the interdependence between n and C is a likely explanation, numerical effects cannot be entirely ruled out and should be considered when interpreting the results.

3.3.4 Tidal deformability

The considerations formulated for the Love number in Subsection 3.3.3 immediately translate into the numerical results for the dimensionless tidal deformability Λ, which are reported in Table 3.1. The observable trends from the obtained Λ values lead to two key conclusions. First, within models that share the same EOS, the tidal deformability decreases significantly with increasing compactness, exhibiting variations up to three orders of magnitude. Second, for fixed compactness, stiff equations of state (smaller n values) are linked to larger deformation power, while NSs endowed with softer equations of state (larger n values), being more centrally condensed, are less prone to deformation. These considerations are consistent with the picture described in Subsection 3.3.3.

n	M/R	k_2	Λ
0.3	0.1	0.1956	13037.2
	0.15	0.1365	1198.57
	0.2	0.0936	195.046
	0.25	0.0536	36.5578
0.4	0.1	0.2031	13541.9
	0.15	0.1432	1257.39
	0.2	0.0964	200.832
	0.25	0.0569	38.8727
0.5	0.1	0.2081	13872.7
	0.15	0.1401	1320.28
	0.2	0.0887	184.795
	0.25	0.0534	36.4414
0.7	0.1	0.1747	11645.3
	0.15	0.1158	1016.97
	0.2	0.0717	149.372
	0.25	0.0398	27.1950
0.8	0.1	0.1563	10423.0
	0.15	0.1022	897.421
	0.2	0.0623	129.860
	0.25	0.0340	23.2780
1.0	0.1	0.1228	8183.92
	0.15	0.0781	685.812
	0.2	0.0455	94.7598
	0.25	0.0234	15.9962
1.2	0.1	0.0935	6236.35
	0.15	0.0577	506.556
	0.2	0.0321	66.8462

Table 3.1: Representative values of k_2 and Λ for different n and $C = M/R$ configurations.

3.3.5 Newtonian limit

Equation (3.46) shows that, in the weak field limit, Newtonian values of the Love number k_2^N only depend on the polytropic index n through the dependence on the y variable and are insensitive to the compactness C. The additional dependence on the compactness parameter exhibited in Equation (3.43) represents a relativistic correction.

As shown in Figure 3.4, Newtonian values are always larger than relativistic values. This can be traced back to the stronger self-gravity experienced by relativistic compact objects, which reduces their ability to deform under an external tidal field. In a relativistic framework, NSs are more gravitationally bound and hence harder to deform, leading to systematically smaller relativistic Love numbers compared to their Newtonian counterparts.

For small compactness, the relativistic correction is less pronounced and is not very sensitive to variations in the polytropic index. This is justified by the fact that the relativistic terms in Equation (3.43) vanish in the low compactness limit, causing the Newtonian and relativistic predictions to converge for $C \to 0$. As compactness increases, relativistic effects introduce substantial corrections that strongly depend on n. The difference between Newtonian and relativistic values becomes dramatic in the corner of the parameter space characterised by large C and small n, where the Newtonian values for the Love number reach up to five times their relativistic counterparts. This analysis confirms that it is crucial to account for relativistic effects in order to accurately model the tidal response of NSs.

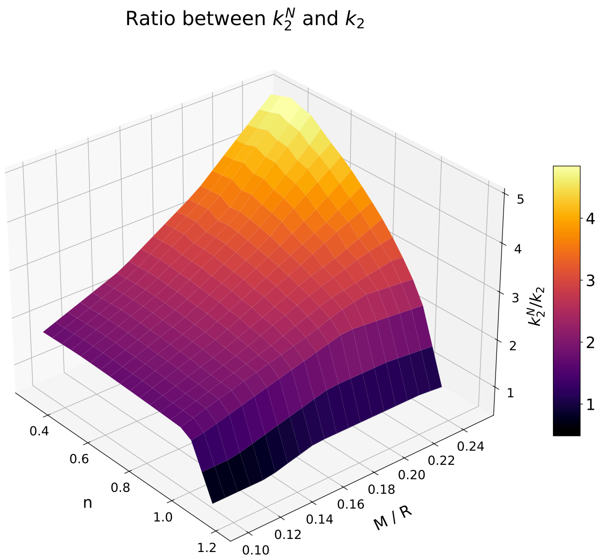

Figure 3.4: Surface plot for the ratio between the Newtonian Love number k_2^N and the corresponding relativistic values k_2 as a function of the polytropic index n and the compactness parameter $C = M/R$. Newtonian values are systematically larger than their relativistic counterparts, an effect that is amplified at small n and large C.

Chapter 4

NUMERICAL SIMULATIONS

In this chapter, the original computational contribution of this work is presented and discussed in detail. The core objective is the development of a numerical scheme to implement tidal perturbations in GRHD simulations of NSs using the `Gmunu` code. This constitutes the primary methodological advancement of the thesis and provides the foundation for future applications involving more complex scenarios.

The simulation setup is designed to reproduce the effect of a static tidal field produced by an external source, allowing the resulting perturbation to be studied in a controlled and isolated environment. The initial equilibrium configuration of the NS is generated with the `XNS` code. However, this equilibrium solution only serves as a starting point and is subsequently modified through the developed computational scheme to incorporate the desired tidal perturbation and initialise a perturbed simulation in `Gmunu`. For simplicity and to ensure consistency with the assumptions of the analytical framework, the simulation setup is restricted to a non-rotating, unmagnetised NS modelled with a polytropic EOS.

Unless otherwise stated, the used formalism assumes geometrised Heaviside-Lorentz units, for which the speed of light c, the gravitational constant G, the solar mass $M_\odot$ as well as the vacuum permittivity ϵ_0 and vacuum permeability μ_0 are all set to one $c = G = M_\odot = \epsilon_0 = \mu_0 = 1$.

The chapter is structured as follows: Section 4.1 introduces the `XNS` code and describes, in Subsection 4.1.1, the process of constructing the equilibrium configuration for the simulated NS. Section 4.2 presents the novel computational scheme developed to modify the initial equilibrium configuration, with the goal of implementing a tidal perturbation on the metric functions. Upon completion of the pipeline, the output consists of perturbed initial data, which can then be injected into GRHD simulations within the `Gmunu` code. Section 4.3 is dedicated to the description of the `Gmunu` code and its main features, while Section 4.4 provides an overview of how a numerical simulation is initialised to test the developed methodology. Finally, Section 4.5 presents the results obtained from the test simulation.

4.1 XNS CODE

Before implementing any perturbation, the NS is initialised using a static equilibrium solution obtained by solving the system of TOV equations coupled with a polytropic EOS for stellar matter. This equilibrium configuration is constructed using the `XNS` code.

The `XNS` code[1] solves for the axisymmetric equilibrium configuration of relativistic stars under the XCFC approximation for the metric. It was developed as a side product of the numerical code `X-ECHO` for GRMHD simulations in dynamical spacetimes, presented by Bucciantini & Del Zanna (2011) as an extension of the `Eulerian Conservative High-Order` (`ECHO`) scheme constructed by Del Zanna et al. (2007). `XNS` uses the same metric solver as `X-ECHO`, in which the Einstein equations are solved in the (3+1) formalism under the assumption of axisymmetry and adopting spherical coordinates for the conformal background metric. Like `ECHO` and `X-ECHO`, also `XNS` is written in the `Fortran90` programming language. The `XNS` code allows the treatment of both rotational and magnetic effects. The first version of `XNS` was specifically designed for polytropic relativistic stars in the presence of differential rotation and a purely toroidal intrinsic magnetic field. Few years later, it was updated to include poloidal and mixed (toroidal-poloidal) configurations for the magnetic field Bucciantini et al. (2014). The most recently released version - `XNS 4.0.0` - has been further extended with the possibility of solving for the structure of rotating, magnetised NSs in massless scalar tensor theories (STTs), that is, in alternative theories to GR. Additionally, support for the use of more realistic tabulated EOS has been introduced. The user has access to a large set of adjustable user parameters, which govern convergence and stabilisation, grid, rotation, magnetic field, initial conditions, equation of state, and more.

4.1.1 EQUILIBRIUM CONFIGURATION

In this work, `XNS` has been used to model the axisymmetric equilibrium configuration of a static, unmagnetised NS in GR described by the piecewise polytropic EOS referred to as `POL2 EOS`, which takes the same form as Equation (2.1). As will be extensively discussed in Section 4.2, the initial data generated in this way only represent the starting point for the development of a computational method that ultimately aims to modify the equilibrium configuration by implementing a tidal perturbation.

Some of the main user parameters in `XNS` and the values they are assigned in this work to compute the equilibrium stellar model are reported in Appendix B. To allow for an immediate visualisation of the features characterising the equilibrium configuration produced by the `XNS` code, it is possible to generate contour plots and graphical representations of the radial profiles for the various hydrodynamic quantities and metric variables.

Figure 4.1 shows a section of the NS in the $x-z$ plane, displaying the density contours (left-hand panel) and pressure contours (right-hand panel). The choice of representing the equilibrium model in the $x-z$ section is motivated by the coordinate convention adopted in the `XNS` code, which assumes axisymmetry about the z axis. In rotating and/or magnetised models, the z axis is conventionally aligned with both the rotation and magnetic axes. As a result, any

---

[1] The GitHub repository of the code including several examples is publicly available at the following link: https://github.com/niccolo-bucciantini/XNS4.0

deformation of the NS configuration induced by spin or magnetic fields, as well as any appreciable variation with respect to the polar angle θ, becomes visible in the $x-z$ plane. More generally, since the $x-z$ section contains the full angular dependence of the model through the polar coordinate θ, it is a representative and informative choice for interpreting the two-dimensional structure of axisymmetric NS models. Clearly, since the equilibrium solution generated by `XNS` is axisymmetric, the choice between the $x-z$ and $y-z$ planes is equivalent, both containing the full angular information. Conversely, a view in the $x-y$ section would collapse the θ dimension, obscuring any axisymmetric distortion.

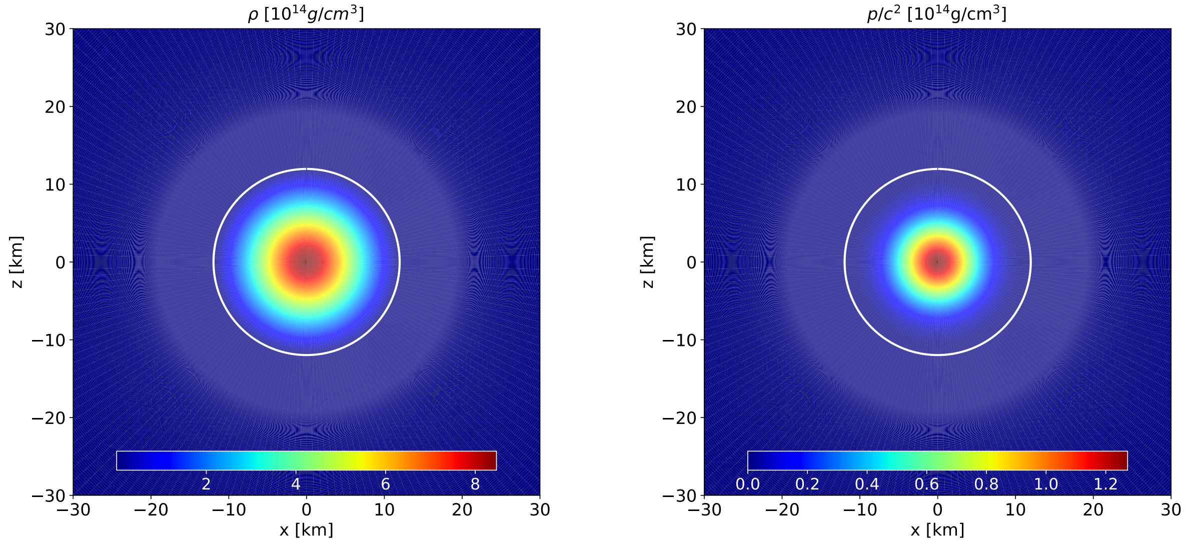

Figure 4.1: *Left-hand panel*: Section of the NS along the $x-z$ plane together with the density contours. *Right-hand panel*: Section of the NS along the $x-z$ plane together with the pressure contours. Both panels refer to the equilibrium configuration generated for the NS by `XNS` with the user parameters specified in Table B.1. The white circle represents the stellar surface, defined in `XNS` as the location where the pressure goes to zero within numerical tolerance.

The circular white contour denotes the stellar surface, which is defined in `XNS` as the location where the pressure drops to zero, within numerical tolerance. For the simulated model, this occurs at $r = 11.97$ km, which can be taken as an estimate for the stellar radius and is in agreement with the characteristic scale for NS radii found in the literature Özel & Freire (2016).

Figure 4.2 presents the radial profiles of density (left-hand panel) and pressure (right-hand panel) across the NS in the top row and complements this information by displaying, in the bottom row, the absolute differences of these quantities computed along the polar axis ($\theta = 0$) and in the equatorial plane ($\theta = \pi/2$).

Overall, the results shown in Figure 4.1 and Figure 4.2 exhibit the characteristic structure for a NS in hydrostatic equilibrium, featuring a dense core and a monotonic decrease of both density and pressure towards the stellar surface. Notably, the pressure gradient near the centre is steeper than that of the density, indicating a relatively stiff EOS in the core region.

The close overlap of the radial profiles along the polar axis and in the equatorial plane, as shown in the top panels of Figure 4.2, suggests an approximately spherically symmetric configuration. This inference is further supported by the plots in the bottom panels of Figure 4.2, which illustrate the absolute difference between polar and equatorial values of density and pressure. The difference curves reveal fluctuations and localized peaks within the star at approximately $r \sim 5$ km for the density and $r \sim 4$ km for the pressure. The absolute difference has magnitude on the order of 10^{-14} g/cm^3 in both cases, which is negligible compared to the typical order of magnitude 10^{14} g/cm^3 for both ρ and p/c^2. Therefore, despite the fact that spherical symmetry was not explicitly enforced during the construction of the equilibrium model, the results strongly support the validity of assuming spherical symmetry in the theoretical treatment of the NS structure.

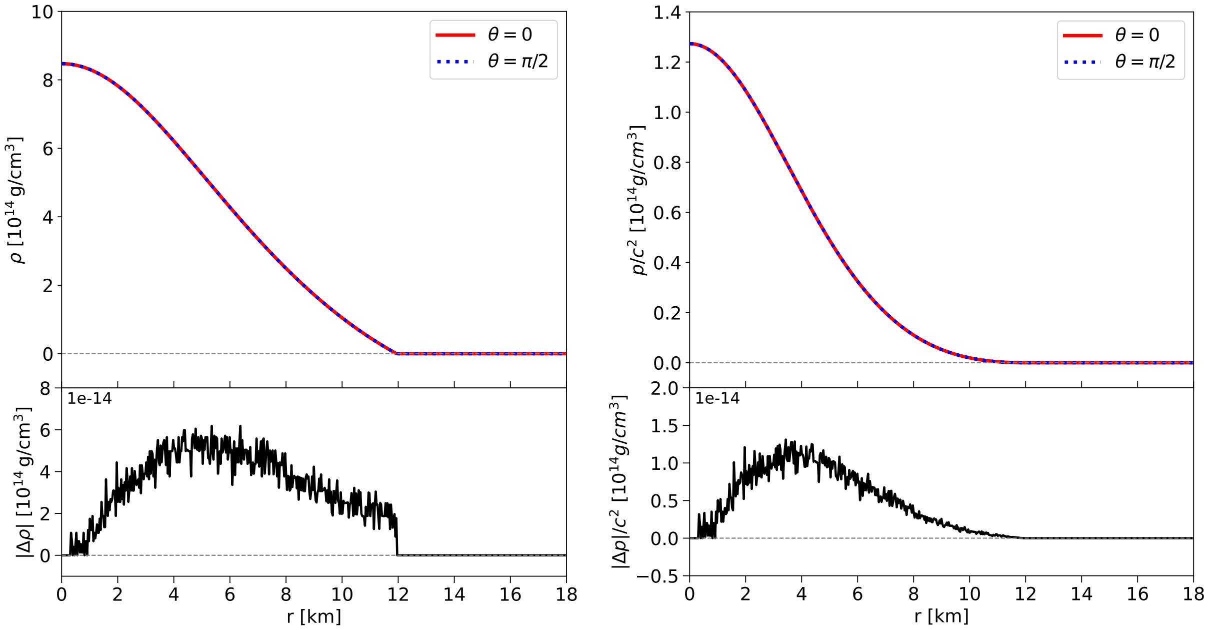

Figure 4.2: *Left-hand top panel*: Radial profile of the NS density at the pole ($\theta = 0$) and at the equator ($\theta = \pi/2$). *Left-hand bottom panel*: Absolute difference between polar and equatorial values of the density. *Right-hand top panel*: Radial profile of the NS pressure at the pole and at the equator. *Right-hand bottom panel*: Absolute difference between polar and equatorial values of the pressure. For both hydrodynamic quantities, the polar and equatorial radial profiles overlap, their absolute difference being of the order of 10^{-14} g/cm^3. This result validates the assumption of spherical symmetry within theoretical calculations.

Similarly, an approximately spherically symmetric behaviour can be observed in the metric functions. This is evident in Figure 4.3 and Figure 4.4, which display respectively the contours and radial profiles of the lapse function α (left-hand side) and the conformal factor ψ (right-hand side). In particular, Figure 4.4 compares the polar and equatorial profiles for the metric functions in the top panels and shows their absolute difference in the bottom panels, which is on the order of 10^{-15}.

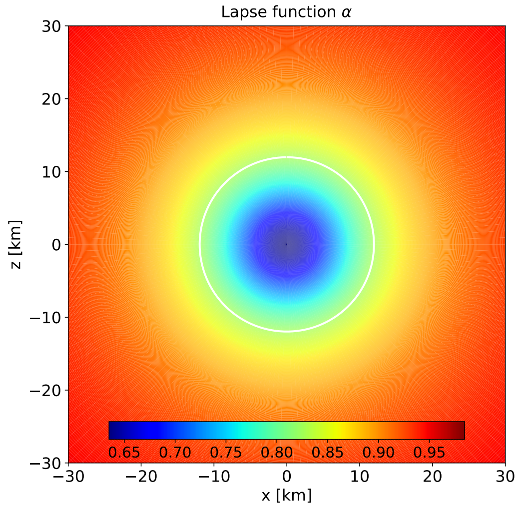

Figure 4.3: *Left-hand panel*: Section of the NS along the $x-z$ plane together with the lapse function contours. *Right-hand panel*: Section of the NS along the $x-z$ plane together with the conformal factor contours. Both metric functions display a spherically symmetric behaviour. The white circle represents the surface of the NS defined as the zero-pressure contour.

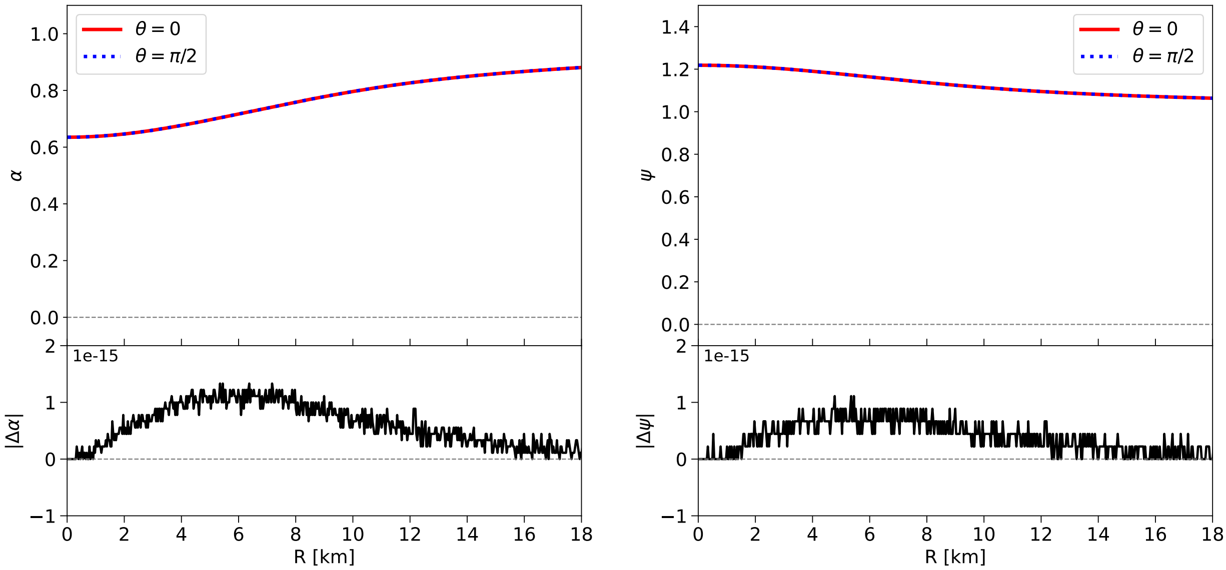

Figure 4.4: *Left-hand top panel*: Radial profile of the lapse function at the pole ($\theta = 0$) and at the equator ($\theta = \pi/2$). *Left-hand bottom panel*: Absolute difference between polar and equatorial values of the lapse function. *Right-hand top panel*: Radial profile of the conformal factor at the pole and at the equator. *Right-hand bottom panel*: Absolute difference between polar and equatorial values of the conformal factor. For both metric functions, the polar and equatorial radial profiles overlap, their absolute difference being of the order of 10^{-15}. This result validates the assumption of spherical symmetry.

4.2 Computational scheme

Initialising the NS with an equilibrium solution ensures a balance between gravitational forces and pressure gradients within the stellar structure. In this scenario, evolving the system over time without any additional external perturbation is not expected to result in any variation in the hydrodynamic quantities describing the star.

Therefore, for a GR(M)HD simulation to yield meaningful results upon evolution, a perturbation must be applied to the NS configuration. Typically, the simulation setup involves providing the `Gmunu` code with the initial data generated by `XNS` describing the equilibrium state of the NS. A subroutine is then introduced in the main script to specify the type of perturbation that the star will experience. For example, a velocity perturbation may be added, which corresponds to imparting a translational velocity kick to the star. In this case, GR(M)HD simulations can be used to study the resulting oscillation modes of the star.

Instead, in the context of the present work, the main interest is to introduce a first-order perturbation of tidal origin. This scenario involves modifying the underlying spacetime metric, which introduces several complexities due to the different formalisms adopted for the definition of the metric in theoretical GR and numerical relativity. As a result, the perturbation cannot be directly implemented in the main `Gmunu` script, and a new and alternative approach must be developed instead. The challenges associated with this operation are discussed in detail in the present section.

Both `Gmunu` and `XNS` adopt the standard ADM formalism, in which the metric takes the form of Equation (2.12). Under the assumptions of stationarity and axisymmetry, all the metric functions defined in the (3+1) metric decomposition depend only on the coordinates r and θ, and the shift vector vanishes $\beta^i = 0$. Conversely, the existence of a non-vanishing component for the shift vector, i.e. $\beta^i \neq 0$ for some spatial coordinate i, would indicate a dragging of the spatial coordinates relative to the slicing of spacetime, which is typically associated with a rotating NS. Therefore, the line element in radial isotropic coordinates in the CFC approximation is given by

$$ds^2_{ADM} = -\alpha^2 dt^2_{ADM} + \psi^4 (dr^2_{ADM} + r^2_{ADM}\ d\Omega^2_{ADM}) \ . \tag{4.1}$$

Instead, in Schwarzschild-like coordinates, the structural form of the metric yields for the line element

$$ds^2_{st} = -A\ dt^2_{st} + B\ dr^2_{st} + r^2_{st}\ d\Omega^2_{st} \ . \tag{4.2}$$

According to Equation (3.12) coupled with the constraint (3.20), the tidal perturbation to the structural metric can be written in the Regge-Wheeler gauge as

$$h_{\mu\nu} = \mathrm{diag}(g^{(0)}_{tt} H(r),\ g^{(0)}_{rr} H(r),\ g^{(0)}_{\theta\theta} K(r),\ g^{(0)}_{\phi\phi} K(r)) \ \cdot\ P_2(\cos\theta) \ , \tag{4.3}$$

which in this case becomes

$$h_{\mu\nu} = \mathrm{diag}(AH(r),\ BH(r),\ r^2_{st} K(r),\ r^2_{st} \sin^2\theta K(r)) \ \cdot\ P_2(\cos\theta) \ , \tag{4.4}$$

and where $P_2(\cos\theta) = \frac{1}{2}(-1 + 3\cos^2\theta)$ is the Legendre polynomial of second order in $\cos\theta$.

The main challenge lies in rewriting the perturbation in Equation (4.4) in a suitable way to be introduced into the ADM formalism for the metric. Since conversion from Schwarzschild-like coordinates to isotropic radial coordinates cannot be performed analytically, it is not possible to reconstruct an analytical counterpart for Equation (4.4) in the ADM formalism. Therefore, if one wants to introduce a perturbation in the numerical code that takes a specific analytical form in Schwarzschild-like coordinates, a different approach needs to be adopted.

The solution proposed in this work consists of developing a computational scheme that involves two conversion steps. First, the numerical data describing the equilibrium configuration obtained by the `XNS` code are mapped to their numerical counterpart referring to the structural metric. This step is straightforward, as analytical relations exist to express r_{st} as a function of r_{ADM}. Once numerical values for the structural metric are available, it is possible to directly incorporate the tidal perturbation, which can be numerically solved in Schwarzschild-like coordinates. Finally, the perturbed metric can be restored in its code-friendly shape. However, this last conversion step is the most challenging, as it can only be performed by numerical integration. The pool of perturbed numerical data obtained in this way is then used as the initial conditions to simulate the NS response in GRHD.

Although this procedure might seem lengthy and complex, it turns out to be the most efficient way to rewrite the perturbed metric in the ADM formalism, as it circumvents the issue of finding a corresponding analytical expression for the tidal perturbation in Equation (4.4). Moreover, this approach is highly extensible and versatile. Any spacetime perturbation that admits a well-defined analytical form in the structural metric can be systematically converted into its numerical counterpart in the ADM formalism using the same procedure. This eliminates the need to manually derive, for each particular case, a corresponding expression adapted to the ADM framework, a task which is often analytically intractable and lacks general guiding prescriptions. Instead of relying on *ad hoc* manipulations or approximations, this method allows for a consistent and robust numerical translation of analytically defined perturbations into ADM coordinates, thus enabling their direct implementation in GR(M)HD simulations.

In the following Subsections: 4.2.1, 4.2.2, 4.2.3; each step of the numerical scheme is presented and discussed in detail, paying particular attention to the imposed assumptions and future improvements.

4.2.1 From ADM formalism to structural metric

Since both the metrics in Equation (4.1) and Equation (4.2) can be used to describe a spherical matter distribution in equilibrium, it is possible to compare the line elements $ds^2_{st} = ds^2_{ADM}$ to obtain a relation between each of the coordinates and metric functions. Setting equal time coordinates $dt_{st} = dt_{ADM} \equiv dt$ and equal solid angles $d\Omega_{st} = d\Omega_{ADM} \equiv d\Omega$, one obtains

$$A = \alpha^2 \tag{4.5}$$

$$r_{st} = \psi^2 \; r_{ADM} \tag{4.6}$$

and, knowing the solution in isotropic coordinates, it is straightforward to derive a simple expression for $r_{st}(r_{ADM})$ from Equation 4.6. From the radial elements, it is possible to retrieve a relation for the radial differentials, which reads

$$\sqrt{B} \; dr_{st} = \psi^2 \; dr_{ADM} \; . \tag{4.7}$$

Starting from the equilibrium configuration generated by `XNS`, Equation (4.5) immediately returns the numerical values for the A coefficient of the structural metric as written in Equation (4.2).

The numerical calculation of the B coefficient from Equation (4.7) is not as straightforward, because it requires computing the numerical derivative of the conformal factor as a function of r_{ADM}. In fact, rearranging Equation (4.7) and substituting the expression for $r_{st}(r_{ADM})$ given in Equation (4.6), one obtains

$$\frac{\psi^2}{\sqrt{B}} = \frac{dr_{st}}{dr_{ADM}} = \frac{d(\psi^2 \; r_{ADM})}{dr_{ADM}} = 2 \; \psi \; \psi' \; r_{ADM} + \psi^2 \; , \tag{4.8}$$

where the prime denotes differentiation with respect to r_{ADM}. It follows that the B coefficient is given by

$$B = \frac{\psi^4}{(2 \; \psi \; \psi' \; r_{ADM} + \psi^2)^2} \; . \tag{4.9}$$

4.2.2 Adding the perturbation

Once the numerical values for the A and B coefficients of the structural metric are available, it is possible to perturb them by introducing a perturbation function describing tidal effects. However, the first-order tidal perturbation expressed in the form of Equation (4.4) presents several challenges when attempting to implement it numerically. In principle, a numerical solution for the perturbation function $H(r)$ can be obtained by solving the differential system in Equation (3.40) under the assumptions specified in Chapter 3. However, this procedure requires careful handling to ensure consistency with the equilibrium model generated by `XNS`.

First, the numerical values for the density and pressure generated by `XNS` are provided on the ADM radial grid, while they need to be mapped onto the structural radial grid. Then the mass function $m(r)$ can be computed using

$$m(r_{st}) = \frac{4}{3}\pi \; r_{st}^3 \; \rho(r_{st}) \; , \tag{4.10}$$

where $\rho(r_{st})$ are the numerical values for the density function computed on the structural radial grid r_{st}. The radius of the star R_{st} can be taken as the value of r_{st} at which the pressure function goes to zero $p(R_{st}) = 0$. With respect to the metric functions, the term $e^{\lambda(r_{st})}$ is immediately obtained once the B coefficient is solved. Instead, recovering $\nu(r_{st})'^{\;2}$ from the A coefficient requires a numerical differentiation operation.

It is also important to recall that while the analytical framework assumes spherical symmetry for the equilibrium configuration, `XNS` generates an axisymmetric model in which both hydrodynamical quantities and metric functions also depend on the angular coordinate θ. Therefore, in principle, to compute the perturbation function $H(r_{st})$ it is necessary to specify all relevant quantities at a fixed value of θ. However, as discussed in Subsection 4.1.1, the angular dependence of the equilibrium model is extremely small, making the deviation from spherical symmetry in the output configuration of `XNS` negligible. Consequently, the equatorial values can be considered representative of the stellar structure across all latitudes. Furthermore, if the goal is to test the specific form of the perturbation in the Regge-Wheeler gauge, the assumption of spherical symmetry does not compromise the validity of the numerical results for comparison purposes.

Another critical aspect of the tidal perturbation as expressed in Equation (4.4) is that it involves two distinct radial perturbation functions: $H(r_{st})$ and $K(r_{st})$. The known analytical relation between these functions links $K'(r_{st})$ to $H(r_{st})$ and is expressed in Equation (3.21). This differential relation makes it non-trivial to derive a numerical solution for $K(r_{st})$.

Given these challenges, I have chosen to first test the computational scheme by introducing a simplified perturbation, written in an analytical form and uniformly applied to all components of the structural metric. This approach allows to focus on the development of the numerical conversion scheme, which can later be refined and adapted to more complex perturbation formalisms.

Under these assumptions and assuming $dt_{st} = dt_{ADM} \equiv dt$ and $d\Omega_{st} = d\Omega_{ADM} \equiv d\Omega$, the perturbed line elements read:

$$ds^{2\ (T)}_{st} = -A\ (1+\mathcal{H})\ dt^2 + B\ (1+\mathcal{H})\ dr^2_{st} + (1+\mathcal{H})\ r^2_{st}\ d\Omega^2 \tag{4.11}$$

and

$$ds^{2\ (T)}_{ADM} = -\alpha^2_T\ dt^2 + \psi^4_T\ (dr^2_{ADM} + r^2_{ADM}\ d\Omega^2)\ , \tag{4.12}$$

where the $^{(T)}$ superscript denotes the tidally perturbed line elements, while the $_T$ subscript denotes the tidally perturbed metric functions in the ADM formalism. To simplify the notation for the following calculations, the letter $\mathcal{H}$ in Equation (4.11) is used to denote the full expression of the perturbation function $\mathcal{H} \equiv H(r_{st})f(\theta)$, which incorporates the angular dependence. This choice is made in continuity with the notation adopted in Chapter 3, where the function $H(r)$ only represents the radial part of the perturbation.

Comparison of the perturbed line elements as done in Subsection 4.2.1 yields

$$\alpha^2_T = A(1+\mathcal{H}) \tag{4.13}$$

$$\psi^2_T\ r_{ADM} = \sqrt{1+\mathcal{H}}\ r_{st}\ . \tag{4.14}$$

The differential relation between radial elements now reads

$$\sqrt{B}\sqrt{1+\mathcal{H}}\ dr_{st} = \psi^2_T\ dr_{ADM} \tag{4.15}$$

and substituting ψ^2_T from Equation (4.14) one obtains

$$\sqrt{B}\sqrt{1+\mathcal{H}}\ dr_{st} = \sqrt{1+\mathcal{H}}\frac{r_{st}}{r_{ADM}}\ dr_{ADM}\ , \tag{4.16}$$

$$\text{therefore}\quad \frac{dr_{ADM}}{dr_{st}} = \sqrt{B}\frac{r_{ADM}}{r_{st}}\ . \tag{4.17}$$

It is important to note that the perturbation terms in Equation (4.16) simplify away only because the same perturbation function is applied uniformly to all metric components. This choice not only enables a more straightforward comparison between the structural and ADM formalisms, but also facilitates the development of the computational pipeline.

The analytical formulation chosen for the perturbation function $\mathcal{H}$ is

$$\mathcal{H} \equiv H(r_{st})f(\theta) = \epsilon\ r^2_{st}\ P_2(\cos\theta)\ , \tag{4.18}$$

where $\epsilon = 10^{-5}$ is an arbitrarily small parameter that determines the strength of the perturbation and $P_2(\cos\theta)$ is the Legendre polynomial of second order in $\cos\theta$

$$P_2(\cos\theta) = \frac{1}{2}(3\cos^2\theta - 1) \ . \tag{4.19}$$

The choice of a quadratic radial dependence $\mathcal{H} \propto r_{st}^2$ reflects the leading-order behaviour of the function $H(r_{st})$ in its asymptotic expansion near the centre of the star, as expressed in Equation (3.23). However, it does not accurately reproduce the full radial profile of $H(r_{st})$. This is evident in the top panel of Figure 4.5, which illustrates the behaviour of the numerical solution for $H(r_{st})$ compared to the quadratic approximation r_{st}^2. The solution for $H(r_{st})$ is obtained by numerically integrating the first-order differential system in Equation (3.40) for a model with polytropic index $n = 1$ and compactness $C = 0.1$. What stands out from the graph is that, while the r_{st}^2 model provides a good approximation for the radial perturbation function at small radii, it fails to represent the behaviour of $H(r_{st})$ at distances greater than $r \sim 4$ km from the centre of the NS. Specifically, the r_{st}^2 curve lies consistently above the actual $H(r_{st})$ and the relative difference, shown in the bottom panel of Figure 4.5, increases with distance. At the stellar surface, the value of R^2 doubles that of $H(R)$, where R denotes the radius of the NS model.

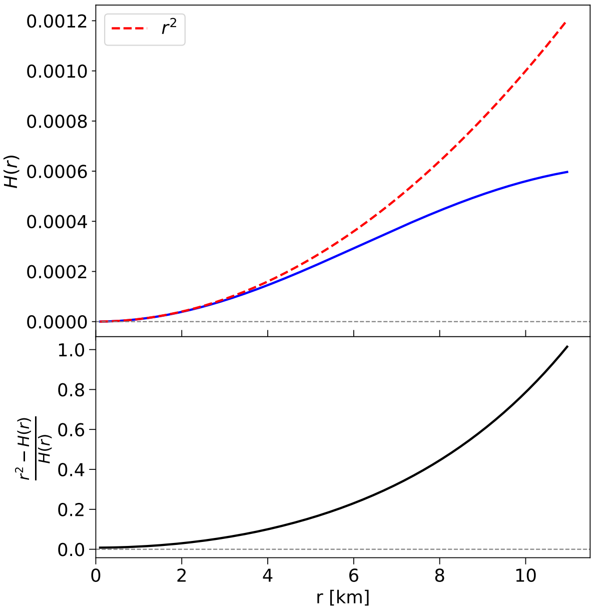

Figure 4.5: *Top panel*: Numerical solution for $H(r)$ obtained by integrating the first-order differential system in Equation (3.40) for a NS model with polytropic index $n = 1$ and compactness $C = 0.1$, compared to the quadratic approximation. *Bottom panel*: Relative difference between the quadratic model and the actual solution for the radial perturbation function $H(r)$. The r^2 approximation well describes the behaviour of $H(r)$ at small radii, but fails to capture its behaviour at larger distances from the centre of the NS. The relative difference increases with r, showing that the quadratic model is not representative of the expected decay of realistic tidal interactions at large distances.

This discrepancy highlights a key limitation: the quadratic form does not capture the physically expected decay of the perturbation at large distances, which is a crucial feature of realistic tidal interactions. Therefore, while the choice $\mathcal{H} \propto r_{st}^2$ facilitates the development and testing of the proposed computational scheme, it does not correspond to a physically accurate profile for the tidal perturbation. Nonetheless, this simplified treatment enables the exploration and validation of a strategy to introduce tidal perturbations into GR(M)HD codes. Therefore, although the resulting simulation does not carry immediate physical significance, the value of this approach lies in establishing the feasibility of the method itself, which can later be refined toward more realistic applications.

With regard to the angular dependence of $\mathcal{H}$, the analytical form in Equation (4.18) is designed to incorporate the characteristic behaviour of tidal deformations through the Legendre polynomial $P_2(\cos\theta)$, which is a natural representation of tidal effects in spherical coordinates. In fact, as mentioned in Subsection 3.1.1, the spherical harmonic $Y_{20}(\theta, \phi)$ appearing in Equation (3.12) can be substituted with the Legendre polynomial $P_2(\cos\theta)$ in case of azimuthal symmetry, the two differing by a constant factor which depends on the normalisation convention for the spherical harmonic.

It is relevant to mention that if the main goal is directly comparing the simulation results with theoretical predictions, the choice of the formalism for representing the perturbation is tied to the specific gauge used in the theoretical framework under testing. However, if the primary objective is to extract quantities related to the tidal deformability from the GR(M)HD simulations regardless of the gauge choice, the requirement to enforce a specific gauge can be relaxed. This allows for more flexibility in the analysis and extraction of meaningful results from the simulation output, provided that the overall physical interpretation remains consistent. Since the primary focus of this work is the development and implementation of the computational scheme, a more precise and accurate treatment to describe the perturbation function is left to be explored in subsequent research stages.

In conclusion, the decision to adopt a simpler, analytical form for the perturbation function allows avoiding additional complexities and is functional to the development of the computational framework. The chosen analytical form provides a simple way of modelling the radial and angular dependencies of the tidal perturbation, providing an acceptable trade-off between complexity and accuracy.

4.2.3 From structural metric to ADM formalism

The last conversion step in the computational pipeline consists in recovering the perturbed metric functions in the ADM formalism. This procedure requires careful handling, because the conversion from standard Schwarzschild-like coordinates to isotropic radial coordinates can only be performed by numerical integration.

The perturbed lapse function α_T is immediately obtained from Equation (4.13). Instead, the computation of the perturbed conformal factor ψ_T from Equation (4.14) is not straight-forward, since to obtain the relation $r_{ADM}(r_{st})$ one needs to numerically integrate Equation (4.17). To facilitate this procedure, Equation (4.17) can be rewritten as

$$\frac{d\ \ln(r_{ADM})}{dr_{st}} = \frac{\sqrt{B}}{r_{st}}\ , \tag{4.20}$$

which can be directly integrated. Once the radial grid in isotropic radial coordinates has been reconstructed, it is possible to compute ψ_T.

Once the computational pipeline reaches its final step, the primary outcome is the set of numerical values for the perturbed metric functions. These values can then be used as initial data for the GRHD simulation within the `Gmunu` code.

4.3 `Gmunu` CODE

The `G`eneral-relativistic `mu`ltigrid `nu`merical (`Gmunu`) code is a multi-dimensional magneto - hydrodynamics code in general relativity, written in the `Fortran90` programming language and available as an open source. `Gmunu` is fully parallelised within the Message Passing Interface (MPI) framework, which is used to distribute the computational load and thereby allows efficient scaling across multiple processors. The code also employs a highly efficient non-linear, cell-centered multigrid elliptic solver, which is fully coupled with a block-based AMR module. The implementation of AMR enables dynamic grid refinement in regions where higher resolution is crucial, such as high-density areas or shock fronts. This approach ensures that computational resources are allocated efficiently, concentrating on regions of interest while maintaining coarser resolutions in less critical areas of the domain.

Using a multigrid approach, `Gmunu` solves the elliptic metric equations using the ADM formalism under the CFC approximation, while the equations of ideal GRMHD are solved using high-resolution, shock-capturing finite-volume methods. The reference metric can be formulated in one, two, or three dimensions, and the code supports Cartesian, cylindrical, and spherical coordinates. This offers great flexibility in setting up simulations that are tailored to the problem at hand. For example, spherical coordinates are ideal for modelling spherically symmetric systems such as NSs or SNe, whereas cylindrical coordinates are advantageous for systems exhibiting axial symmetry such as accretion disks. In the magnetised case, the code ensures that the magnetic field remains divergence-free by employing a divergence cleaning procedure. This is crucial for maintaining the physical accuracy of simulations, as spurious magnetic monopoles can otherwise develop.

In GRMHD, the evolution of the fluid is governed by the conservation laws of rest mass, energy, and momentum, which are formulated in a conservative form. This means that the evolved quantities are not the physical (*primitive*) variables such as density, pressure, and fluid velocity, but rather *conserved* quantities obtained from non-linear combinations of the primitive ones. Conserved quantities are designed to preserve fluxes across cell interfaces and thereby ensure the correct treatment of fluxes throughout the grid. This formulation is particularly well suited for finite-volume methods in numerical relativity, which are also employed in `Gmunu`. The `Gmunu` code evolves the system using a time integration scheme applied to the conservation equations, starting from a set of prescribed initial conditions. After each time step, a recovery procedure is applied to restore the primitive variables from the updated conserved ones. This step is non-trivial, as it involves solving a set of non-linear equations that map the conserved quantities back to the primitive variables.

4.4 SIMULATION SETUP

Using the computational scheme developed in Section 4.2, the initial perturbed data are generated to run a GRHD simulation of a non-rotating, unmagnetised NS within the `Gmunu` code. For the simulation presented in this work, the setup is configured in 3D Cartesian coordinates, a choice that allows for a comprehensive characterization of the NS response to the tidal perturbation.

Metric evolution

When injecting initial data featuring tidally perturbed metric functions, it is crucial to ensure that the perturbation does not decay during the simulation. Since the goal is to simulate the effect of a static and constant tidal field, it is necessary to prevent any evolution of the metric functions during the numerical integration. This is achieved by configuring the relevant parameters within the simulation code, and specifically by setting the boolean flags

```
cfc_evolve = .False.
initialize_metric = .False. .
```

By doing so, the code is instructed to evolve only the hydrodynamic variables, while keeping the perturbed metric functions fixed throughout the simulation. This setup ensures that the tidal field remains constant, effectively representing a static contribution from a fixed external source.

However, freezing the metric inherently limits the physical consistency of the simulation, as it prevents the spacetime geometry from responding dynamically to changes in the matter distribution. In this configuration, the Einstein equations are effectively treated with a one-way approach, where the metric influences the hydrodynamic evolution, but not vice versa. A possible strategy to partially recover this feedback would be to implement an adaptive iterative scheme in which the metric functions are updated after a fixed number of time steps based on the evolving fluid variables.

Equation of state

To ensure consistency with both the theoretical framework and the user-specified parameters in `XNS`, the simulation is initialised using a polytropic EOS with the same values of adiabatic index `eos_gamma` and polytropic constant `eos_adiab` as the `GAMMA` and `K1` parameter values specified in Appendix B. The polytropic EOS is a barotropic relation, meaning that the pressure depends solely on the density, without any explicit dependence on temperature or internal energy. While this is appropriate for modelling cold, static configurations, it becomes a limitation in dynamical simulations, where perturbations, shocks, or compression can generate thermal energy. Since a purely polytropic EOS cannot capture the associated increase in thermal pressure, many GRHD codes, including `Gmunu`, provide an EOS-related flag to enable an approximate treatment of thermal effects. When activated, this option augments the polytropic pressure with an additional thermal component. In the context of this work, the simulation is inherently dynamical due to the imposed perturbation, therefore the thermal effect is activated by specifying

```
thermal_effect = .True. .
```

Stellar surface

The stellar surface is operationally defined as the boundary beyond which the density drops below a user-specified threshold value. In this sense, the NS surface in `Gmunu` does not represent a physical discontinuity but rather a numerical boundary used to truncate the stellar model at a low-density outer envelope. Regions characterised by density values lower than the threshold can be safely considered to be external to the modelled star.

Computational atmosphere

In order to enforce numerical stability in regions outside the NS, the computational domain is filled with an artificial low-density medium referred to as the *atmosphere*. Despite its name, this does not correspond in any way to the thin physical atmospheric layer enveloping the star. Instead, it is a numerical artifact introduced on purpose to prevent divergence issues due to division by zero in flux-conserving schemes. In practice, the hydrodynamic solver requires finite, non-zero values at every grid point across the domain in order to operate correctly. The computational atmosphere follows an ideal gas EOS and is typically assigned density values several orders of magnitude lower than those found in the stellar interior.

Although one might be tempted to draw an analogy with the presence of a physical magnetosphere surrounding realistic NSs, such a comparison is not appropriate. The density of the computational atmosphere remains many orders of magnitude higher than that of a realistic magnetospheric plasma, and the atmosphere itself is not evolved self-consistently as part of the physical system. Therefore, it plays no dynamical role and is not intended to simulate any physical process. In conclusion, despite its presence in the numerical domain, the computational atmosphere has negligible impact on the physical solution for the NS, which is effectively modelled as being in vacuo and can be treated as such.

4.5 Simulation results

This section presents and comments on the results obtained from the numerical simulation that has been initialised as described in Section 4.4. To aid in the interpretation, the perturbed configuration is systematically compared with the outputs of a simulation in which no perturbation was applied. This comparative approach provides a clear benchmark that allows one to directly identify the effects induced by the tidal perturbation. By comparing the perturbed and unperturbed cases, it is possible to ensure that the observed features in the simulation are ascribable to the tidal perturbation. This comparison serves as a crucial validation step, confirming that the introduced perturbation is the primary cause of the observed structural and dynamical changes in the star.

The set up of the unperturbed simulation is identical to the perturbed case described in Section 4.4, with the only difference that the initial data represent the equilibrium TOV solution for the NS, and no perturbation was applied. The interpretation of the outputs is facilitated by the generation of density plots, which represent the structure of the NS and its response to external forces. The contour plots of the density along the various sections of the NS at times t = 0.0 s, 2.0 ms, 4.0 ms, 5.9 ms, 7.9 ms, and 9.9 ms are collected in Appendix C.

Both the perturbed and unperturbed NS models exhibit signs of matter diffusion from their outer layers during the simulation. This effect can be inferred from the time evolution of the central density of the star, shown in the top panel of Figure 4.6. In principle, the unperturbed configuration is expected to remain unchanged over time. In fact, being initialized with a numerical solution of the TOV equations, the hydrodynamic quantities should remain constant in absence of any external perturbation. However, in practice, perfect conservation of the hydrodynamic variables throughout the simulation is not possible due to numerical effects such as grid noise. This refers to small, artificial fluctuations that arise from discretising the equations of motion on a finite grid.

Moreover, the inclusion of thermal effects in the polytropic EOS allows the internal energy to contribute to the pressure, which can cause diffusion of matter from the outer layers of the NS. This thermal contribution is not present in the theoretical cold equilibrium model and can explain the small but measurable decrease in central density over time. The influence of thermal effects on NS configurations has been widely researched, particularly in the context of BNS mergers. For instance, Baiotti et al. (2008) conducted simulations of inspiralling BNS systems comparing polytropic models lacking thermal energy contributions with ideal gas models incorporating thermal effects. The results showed that the impact of thermal pressure produced less compact merger remnants, with lower central densities compared to their colder counterparts. This reduction in compactness can facilitate the shedding of material from the outer layers and the formation of outflows, significantly delaying gravitational collapse and contributing to a redistribution of matter to less dense regions over time. These effects are absent in models where thermal contributions are neglected. Many studies have also investigated how different approaches to incorporate thermal effects influence the remnant evolution and the observed GW signal, further highlighting the importance of including thermal effects in the modelling of NS behaviour Bauswein et al. (2010) Miravet-Tenés et al. (2025).

The relative variation of the rest mass over time is also inspected and monitored as an indicator of the conservation properties of the numerical code. As shown in the bottom panel of Figure 4.6, the rest mass is preserved remarkably well, with its relative variation being on the order of 10^{-7}. This confirms the robustness of the numerical code and validates the reliability of the simulation even in the presence of thermal effects.

One of the most notable outcomes of the simulation comes from studying the effect that the implemented perturbation induces on the NS configuration. In the perturbed case, the matter configuration suffers from a deformation that causes it to deviate from spherical symmetry, while the unperturbed model maintains a spherically symmetric profile. This deformation is particularly evident in the distribution of low-density diffused material surrounding the star. This outer layer does not belong to the physical NS and is likely a numerical artifact arising from the mapping of the perturbed data into the `Gmunu` code. Although it lacks physical significance, it serves as a diagnostic tool to assess how the configuration responds to the perturbation implemented within the code.

Panels (a), (b) and (c) of Figure 4.7 display the radial density profiles along the x, y and z axes respectively, at the final simulation time $t = 9.9$ ms for both the perturbed and unperturbed configurations. In all directions, the density distribution within the stellar interior remains largely unaffected, indicating the strong gravitational binding of the core. Panels (a) and (b) show that the density distribution is affected in the same way along the x and y axes, and particularly the

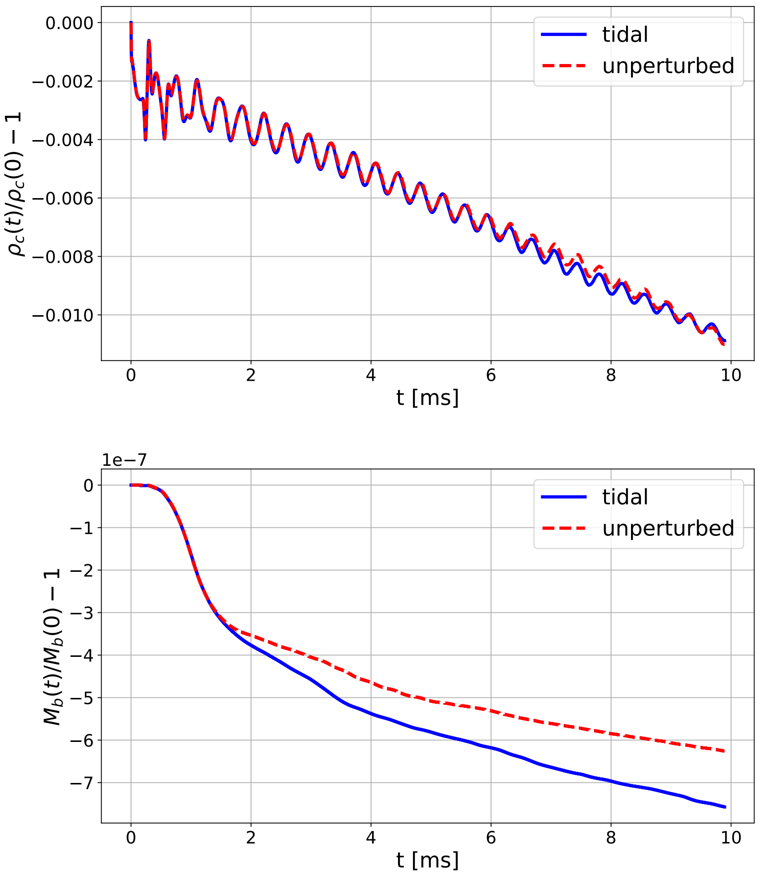

Figure 4.6: *Top panel*: Relative variation of the central density ρ_c in time. Its overall decreasing behaviour can be ascribed to the presence of thermal effects, causing matter to diffuse around the NS. *Bottom panel*: Relative variation of the rest mass M_b in time. The rest mass is preserved remarkably well, with its relative variation being on the order of 10^{-7}.

diffuse matter around the star exhibits a modest elongation in the perturbed case with respect to the equilibrium profile. This symmetric deformation in the $x - y$ plane provides information on the location of the ideal perturbation source, and suggests that the perturbation is effectively distributed as a ring in the equatorial plane around the NS. Such a configuration is consistent with the axisymmetric angular structure of the applied perturbation function. Qualitatively, it resembles the integrated effect of spin, reproducing the quadrupolar deformation that the body would suffer from if it was rotating around the z axis.

Panel (c), illustrating the density profile along the z axis, reveals a more pronounced effect, that is a clear contraction of the extended matter envelope in the polar direction. The maximum extent of the density distribution in this direction reduces from approximately 40 km in the unperturbed case to about 32 km in the perturbed configuration. This asymmetry, characterized by equatorial stretching and polar compression, is a distinctive signature of quadrupolar distortion and directly reflects the angular dependence $\mathcal{H} \propto P_2(\cos\theta)$ imposed in the perturbation model.

In summary, this simulation demonstrates the feasibility of implementing a tidal-like perturbation within the computational framework of GRHD codes, and analysing its effect on a NS configuration. Although the low-density material surrounding the NS lies outside the physically meaningful stellar interior, its deformation pattern provides valuable insight into the effect of the implemented perturbation. Despite the radial dependence of the perturbation was introduced in a simplified form and does not reproduce the full physical behaviour, the accurate treatment of its angular structure led to a deformation that qualitatively resembles the quadrupolar geometry expected for a tidally deformed object. While the model should not be interpreted as physically complete, it represents valuable proof of concept. This successful test case lays a solid foundation for future developments, where the method can be refined and extended to incorporate more realistic perturbation profiles and physical effects.

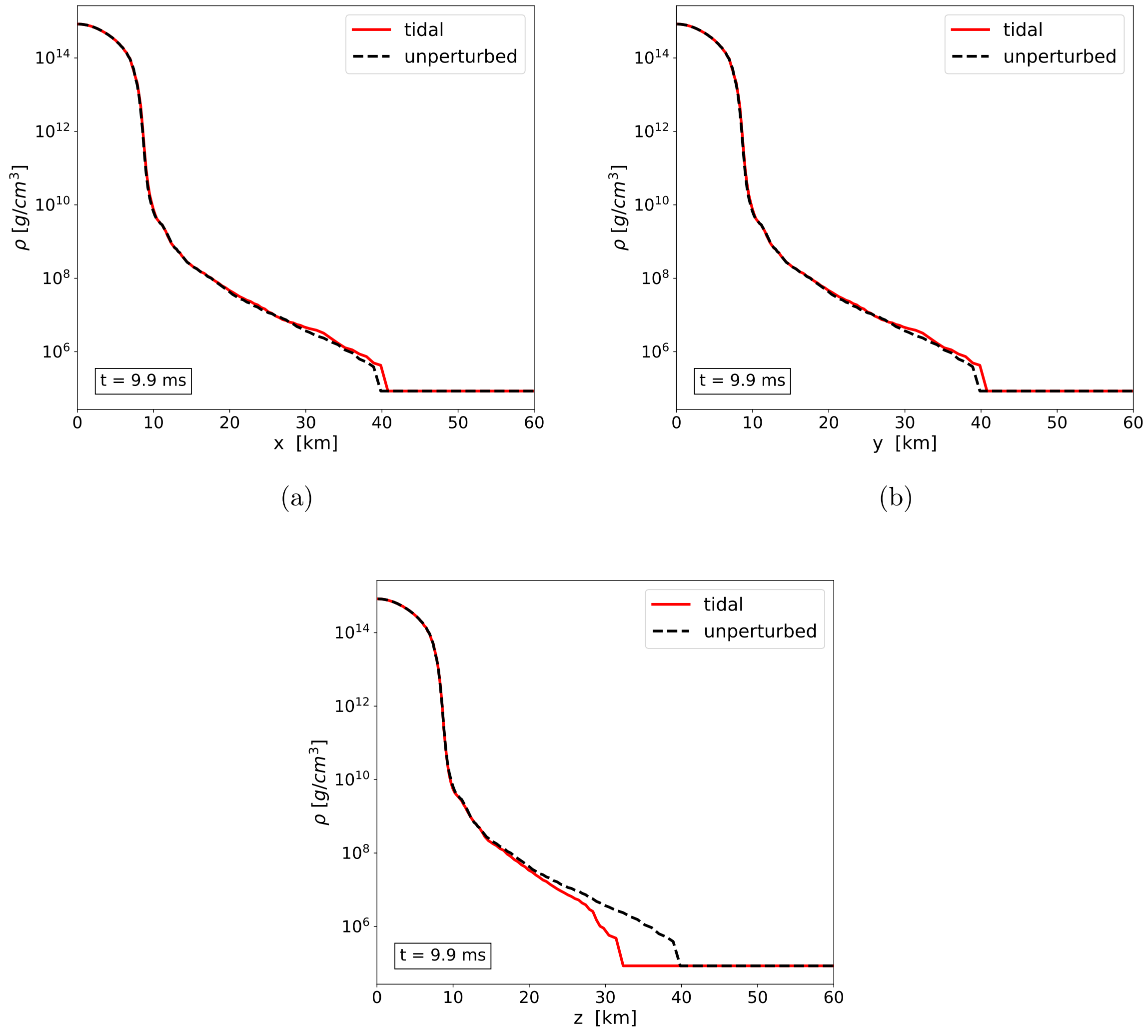

(a)

(b)

(c)

Figure 4.7: Radial profiles of the density along the x (Panel (a)), y (Panel (b)), and z (Panel (c)) axes at the final simulation time $t = 9.9$ ms for both the perturbed and unperturbed configurations. While the inner regions are not significantly affected by the perturbation, the outer layers of diffused material exhibit a slight elongation along both x and y axes and a more consistent contraction along the z axis. This response is consistent with the expected quadrupolar geometry of a tidally deformed object, as it reflects the imposed angular dependence $\mathcal{H} \propto P_2(\cos\theta)$ on the perturbation function.

Chapter 5

DISCUSSION

In Chapter 4, a detailed methodology was presented to consistently introduce tidal perturbations into GR(M)HD simulations of NSs. Additionally, the procedure for initialising simulations that emulate the effect of a static, external tidal field was outlined. However, once the simulation outputs are generated, the challenge arises in interpreting these results, understanding their significance, and extracting meaningful scientific information from them. This chapter is primarily focused on offering possible pathways for results interpretation, paying particular attention to the assumptions underlying the computational setup and to other aspects that require careful consideration when drawing conclusions from the simulation outcomes.

Section 5.1 focuses on the extraction of tidal deformability, or some related quantities, from the numerical data, and presents two distinct approaches for this purpose. Section 5.2 then examines the conditions under which a direct comparison between numerical results and theoretical predictions, or observational data, can be made in a scientifically valid manner.

5.1 EXTRACTING THE TIDAL DEFORMABILITY

Once the simulation outputs have been obtained, the ultimate objective is to extract a quantity related to the tidal deformability of the simulated NS, a knowledge that would lead to a deeper understanding of the tidal response of these extreme compact objects.

To begin with, let us recall the definition of the tidal deformability parameter λ, as expressed in Equation (2.2). The central idea in understanding the quadrupolar response of the star to an external tidal field is to estimate the tidal field strength $\mathcal{E}_{ij}$ and the tidal response Q_{ij}, and then compare these two quantities.

Given the approach used to implement the perturbation in this work, the tidal field $\mathcal{E}_{ij}$ is relatively straightforward to model. In the isolated setup of the simulations, its strength is controlled by a fixed coefficient ϵ of constant value, which is a parameter specified by the user. This coefficient parametrizes the magnitude of the perturbation applied to the star and provides a first estimate of the external tidal field strength.

The most challenging quantity to model in this context is the tidal response Q_{ij} experienced by the test NS, as there exist no unique definition of the quadrupole moment in GR. One approach to address this point is to use the Newtonian definition of Q_{ij} as written in Equation (2.5) as a first estimate.

Then, by comparing the Newtonian estimate of Q_{ij} with the tidal field strength ϵ, one can obtain a rough evaluation of the influence exerted by the tidal perturbation on the NS configuration and structure.

However, this approach relies on several simplifications. First, the use of a Newtonian formula for Q_{ij} contrasts with the relativistic framework in which the simulations, as well as the theoretical computations, are performed. Second, the perturbation itself is modelled using a simplified analytical form. The chosen form in Equation (4.18) provides a reasonable approximation of tidal interactions while at the same time being computationally feasible, but it does not fully capture the complex behaviour of tidal interactions.

An alternative approach for estimating the tidal response Q_{ij} involves using the multipole coefficients c_m extracted from the density distribution of the NS. These coefficients represent the various contributions to the star deformation in the multipolar expansion and are computed by decomposing the star density along the azimuthal direction. This operation is performed by

$$c_m(t) = \int d^3x \ \sqrt{\gamma} u^0 \rho(t, \vec{x}) \ e^{im\phi} \ , \tag{5.1}$$

where γ is the determinant of the spatial metric γ_{ij} as defined in the (3+1) formalism, u^μ is the fluid four-velocity, $\phi = \tan^{-1}(x/y)$ is the azimuthal angle, and $\sqrt{\gamma} u^0 \rho(t, \vec{x})$ is the conserved density, which is preferred to the physical density $\rho(t, \vec{x})$ in the context of flux-preserving methods like those employed in `Gmunu`. The definition in Equation (5.1) then yields a complex number for each azimuthal mode m.

The c_m coefficients are provided in the simulation outputs and listed in the `output.log` file, where the real and imaginary parts are given for each value of $m = 1, 2, 3, 4$. The physical meaning of each c_m is as follows:

- $m = 1$ – Dipole: This mode corresponds to the dipole deformation of the star. In the ideal case of a perfectly spherically symmetric configuration, this contribution is expected to vanish. Therefore, small non-zero values of c_1 indicate deviations from spherical symmetry, pointing to slight asymmetries in the star structure or to the influence of external forces breaking spherical symmetry.
- $m = 2$ – Quadrupole: This corresponds to the quadrupolar component of the oscillation modes, which is the key contribution for studying the tidal deformability. The coefficient c_2 represents the quadrupolar response of the NS to the tidal field, and its amplitude measures the magnitude of the quadrupolar deformation in the star.
- $m = 3$ – Octupole: This mode corresponds to third-order deformations of the star. The coefficient c_3 captures these oscillations.
- $m = 4$ – Hexadecapole: Similarly, this mode is related to fourth-order deformations, with the coefficient c_4 encoding this contribution.

In practice, it is possible to compute the amplitude of each mode using the formula

$$|c_m| = \sqrt{(\mathcal{R}e(c_m))^2 + (\mathcal{I}m(c_m))^2} \,, \tag{5.2}$$

where $\mathcal{R}e(c_m)$ and $\mathcal{I}m(c_m)$ are the real and imaginary part of c_m respectively. The amplitude of each multipole coefficient provides information about the relative contribution of the corresponding modes to the overall deformation. Since the quadrupolar mode is the dominant component in tidal interactions, c_2 is the coefficient of interest in the study of tidal deformability.

After computing the amplitude of the quadrupolar coefficient c_2, it is possible to normalize it by a characteristic quantity of the star, such as the total rest mass, to obtain a dimensionless measure of the deformation. This allows for meaningful comparisons across different simulations of NSs with varying masses and radii.

With this approach, one can compare the amplitude of the quadrupolar deformation, represented by c_2, to the external tidal field strength ϵ in order to estimate the tidal deformability parameter.

The coefficient c_2, exhibiting a time dependence, also contains information about the behaviour of the quadrupolar deformation over time. By tracking the time variation of the normalised values for the amplitude $|c_2|$, it is possible to study how the tidal deformation evolves in time and whether it reaches a steady state or displays oscillations instead.

5.2 COMPARISON OF THE RESULTS

The effort of this work in developing a computational pipeline to consistently implement tidal perturbations in numerical relativity is finalised to enable a meaningful comparison between the simulation results and theoretical predictions. However, in order for such a comparative analysis to be valid, some important aspects need to be considered.

First, if the main goal is to draw parallels between numerical and analytical results, it is essential to ensure that the perturbation is initialised in the computational pipeline using the same gauge as the theoretical framework. The choice of gauge can significantly affect the analytical form of the perturbation, and any gauge inconsistency could result in misleading interpretations when directly comparing the simulation output with the theoretical predictions.

An alternative and promising approach would be to compare the numerical results with the tidal deformability measurements obtained from GW observations. However, for a meaningful comparison, it is crucial to make sure that the considered measurements refer to the early inspiral stage of the BNS system.

Giving thought to this concern is particularly relevant because the approach outlined in this work describes an isolated system scenario, where the source of the external quadrupolar perturbing field is static and remains at a fixed distance from the test NS. Although this setup does not fully capture the dynamic nature of binary interactions, it serves as a reasonable approximation for the early inspiral of BNS systems. During this phase, the orbital separation between the binary components is large enough that the timescale over which the tidal perturbation evolves is much longer than the dynamical timescale of the system. Under these conditions, the time dependence of the tidal field can be neglected and the static field approximation holds. It follows that, in this context, performing simulations of isolated, tidally perturbed NSs such as the one presented in this work retains physical relevance and validity. The extracted information on the NS tidal properties provides a solid basis for comparison with observational data from early BNS inspirals.

It is also important to note that the scenario depicted in the present work represents a simplified model compared to the actual physical conditions found in real BNS systems. For a direct comparison with GW observations, one must carefully estimate the relative contributions of additional factors such as fast rotation and strong magnetic fields, which are not accounted for in this study but can be relevant in realistic systems. These aspects will be discussed in more detail in Section 6.1.

Chapter 6

CONCLUSIONS

This chapter summarises the key steps of the research and presents the main conclusions drawn from the results obtained throughout the study. It also includes a detailed discussion of possible future developments of the presented work, addressed in Section 6.1.

The investigation of tidal deformation in NSs has been carried out through two complementary approaches. First, the problem was examined from a theoretical perspective, establishing a robust analytical framework for understanding tidal interactions in the static response approximation. Second, a simplified description of tidal perturbations was introduced into a GRHD simulation, allowing the perturbation to be studied in an isolated and controlled setting. By combining these two methodologies, this work leveraged the strengths of both analytical and computational techniques, resulting in a comprehensive treatment of the problem. This integrated strategy ensured that the final model was not only grounded in solid theoretical principles, but also adaptable to a variety of plausible physical scenarios. Numerical simulations offer the flexibility to test models under a wide range of physical conditions, allowing for a nuanced understanding of the problem and paving the way for future extensions of the current work.

The first part of the thesis focused on establishing the theoretical framework of metric perturbation theory, with particular emphasis on the implementation of a first-order tidal perturbation to the unperturbed Schwarzschild-like metric. In Chapter 3, the TOV solution for NSs was numerically computed for various combinations of polytropic index n and compactness C. The resulting radial profiles of mass and pressure exhibit the expected behaviour of NS models with varying compactness. In particular, under the assumption of a fixed EOS, more compact stars reach higher total masses and exhibit smaller radii. Conversely, less compact stars are less massive and more extended. The analysis also shows that more compact stars develop higher central pressures and steeper pressure gradients, which are required to balance the stronger gravitational pull and maintain hydrostatic equilibrium.

Next, the Love number and the dimensionless tidal deformability were analytically computed as functions of n and C. The combined effect of these two parameters indicates that the NS configurations most susceptible to tidal deformation occur at low compactness and low polytropic index, conditions typically associated with a stiff EOS. In contrast, the least deformable stars are those with high C and high n, corresponding to a softer EOS. Across all values of n, the Love number exhibits a monotonically decreasing trend with increasing C. This behaviour reflects the fact that, for a fixed EOS, more compact stars are more gravitationally bound and therefore less responsive to external tidal forces. Additionally, higher values of n result in lower Love numbers across all compactness values, indicating that more centrally condensed stars are more resistant to tidal deformation.

Finally, a comparison between the relativistic Love number and its Newtonian counterpart revealed that Newtonian predictions consistently overestimate the tidal response. The relativistic correction becomes more pronounced as the compactness increases, a behaviour that can be attributed to the increased self-gravity in relativistic models. This stronger gravitational binding reduces the NS ability to deform under an external tidal field, highlighting the importance of incorporating relativistic effects when modelling the tidal response of compact objects.

In the second part of the thesis, a computational model was developed to implement spacetime perturbations within the framework of numerical relativity. The approach focused on directly modifying the metric functions that describe the underlying spacetime. One of the main challenges encountered in this process was the mismatch between the theoretical formalism used to describe tidal perturbations and the conventions adopted by numerical relativity codes. To tackle this issue, a computational strategy was devised to ensure that the perturbed metric functions were ultimately expressed in a form compatible with the numerical simulation framework.

The method adopted in this work built upon the equilibrium configuration generated by `XNS` and involved two main conversion steps. First, the metric was converted from the ADM (3+1) formalism to the structural form. This conversion was a necessary step for introducing a perturbation function which retained a well-defined analytical expression in Schwarzschild-like coordinates. To focus on developing and testing the computational scheme, a simplified representation was chosen for the tidal perturbation. Although not of immediate physical significance, this approach enabled the exploration of a novel strategy for introducing tidal perturbations into GRMHD codes. Once the perturbation was applied, the modified structural metric was converted back into the ADM formalism, which is required for use in the numerical evolution scheme. This process allowed the construction of an initial data set describing a perturbed NS, which was then used to initialise a test simulation. The simulation setup was designed to preserve the perturbation over time by freezing the metric evolution throughout the simulation, effectively mimicking the effect of an external, static tidal field. This approach enabled isolating the tidal contribution, allowing a focused study of its impact on the NS structure in a controlled environment. By avoiding the complexities of full binary evolution, this method provided a clean framework to investigate the response of an isolated NS to an external tidal perturbation.

The simulation results were systematically compared to a control case in which no tidal perturbation was applied. This comparative analysis provided a clear benchmark for directly identifying the effects induced by the implemented perturbation. While the unperturbed model preserved its spherical symmetry throughout the evolution, the perturbed configuration exhibited a clear quadrupolar deformation, primarily affecting the low-density material surrounding the star. Although this outer layer lies outside the physical NS and likely originates from a numerical artifact within the data mapping procedure, its deformation pattern served as a useful diagnostic tool for studying the configuration response to the implemented perturbation. In particular, the density profile plots revealed a characteristic contraction along the z axis and a corresponding, though less pronounced, elongation along the perpendicular x and y directions. This deformation pattern directly reflects the angular dependence imposed in the perturbation model and qualitatively matches the expected geometry of a tidally deformed configuration. This outcome validates the feasibility of the developed computational scheme and provides a solid proof of concept for the implementation of tidal-like perturbations in GRHD codes. The results establish a strong foundation for future work, with the aim of refining the perturbation model and incorporating more realistic physical effects, such as rotation or time-dependent tidal fields.

In conclusion, the computational scheme developed in this work has been demonstrated to be functional and represents an initial step toward consistently implementing spacetime perturbations in hydrodynamic simulations. This approach constitutes a novel effort to introduce and model tidal perturbations in a controlled, isolated setting, offering a comprehensive tool for studying the structural response of NSs to external tidal forces. Furthermore, the method provides flexibility for incorporating additional physical effects, such as magnetic fields, rotational effects, and more realistic EOS, which could significantly enhance the investigation of NS tidal deformability.

6.1 FUTURE PROSPECTS

In this exploratory study, a simplified picture has been adopted for the description of NSs and their tidal interactions. Several assumptions were made to streamline the problem and make it computationally feasible. Specifically, the study was limited to non-rotating and unmagnetised NSs, and a unified polytropic model was used to approximate the EOS of stellar matter. Additionally, the analytical formalism chosen to express the tidal perturbation and introduce it into the computational framework was a significant simplification compared to the more complex, theoretically derived form of the tidal perturbation as in Hinderer (2008). Despite being simplifying assumptions, these approximations have been instrumental in constructing a robust numerical method for implementing spacetime perturbations within GR(M)HD simulations of isolated NSs. This simplified approach provided a solid foundation for the initial development of the numerical scheme, reducing computational complexity while still capturing essential tidal effects.

Although the current approach has been proven to be functional, the methodology is well suited for adaptation to more complex and realistic scenarios. By their nature, numerical simulations are flexible and allow for the incorporation of additional physical effects in the picture. The present section will discuss potential future refinements, addressing the limitations of the current model and outlining ways to extend its applicability to a broader range of astrophysical scenarios.

Tidal perturbation formalism

One potential refinement of the current model involves improving the analytical description of the tidal perturbation. The perturbation functions $H(r)$ and $K(r)$ can be solved by numerical integration to resemble more closely the theoretical formalism developed by Hinderer (2008). This would allow for a more accurate description of the first-order tidal effects on the NS structure. Moreover, as discussed in Section 5.2, a faithful implementation of the perturbation according to the analytical formalism outlined in the literature would allow a direct comparison between numerical results and theoretical predictions.

Intrinsic magnetic fields

Another valuable addition would be to include the effects of strong intrinsic magnetic fields in the computational framework. The `XNS` code already supports various magnetic field topologies, ranging from purely poloidal to purely toroidal configurations, as well as mixed twisted torus configurations. Similarly, the `Gmunu` code can accommodate magnetised cases, providing numerical tools for MHD evolution. One relevant feature of `Gmunu` in MHD is the elliptic divergence cleaning approach, which ensures that the magnetic field remains divergence-free. This is important because, in principle, the divergence-free condition for the magnetic field may not be satisfied during direct evolution because of the accumulation of numerical errors. Then, to account for the combined effects of tidal interactions and magnetic fields, an appropriately defined perturbation must be introduced within the computational scheme.

Incorporating magnetic effects is particularly relevant because, as mentioned in Chapter 2, NSs are known to possess some of the strongest magnetic fields in astrophysics, with surface strengths reaching up to $10^{14} - 10^{15}$ G for the class of *magnetars*. These intense magnetic fields influence not only the internal structure and stability of the stars but also the gravitational dynamics in binary systems.

One of the first contributions to the calculation of the magnetically modified tidal deformability was presented by Zhu et al. (2020), who proved that the tidal deformability varies due to magnetic effects. In particular, for weak gravitational fields (i.e., low compactness), the tidal deformability is enhanced in the magnetised case, as the quadrupolar deformation induced by the magnetic field adds up constructively to that of tidal origin. In contrast, for strong gravitational fields (i.e., high compactness), the intrinsic magnetic field counteracts the tidal deformation by exerting additional magnetic pressure and tension. Although the relative change in tidal deformability is generally small and negligible for magnetic fields of the order of $10^{12} - 10^{13}$ G, predictions indicate that it could reach up to approximately $4 - 6\%$ for fields near 10^{16} G Zhu et al. (2020). In these cases, the magnetic field would contribute substantially to the gravitational-wave phase evolution. Although such extreme magnetic field strengths are unlikely to be reached during the inspiral phase, the enhanced sensitivity of next-generation GW detectors is expected to enable the detection of even the subtle effects produced by moderately strong fields. Consequently, incorporating magnetic field contributions into the modelling of tidal effects in the static response approximation, which resembles the inspiral phase, remains a valuable pursuit, as it offers an additional probe into the internal properties of NSs.

Theoretically, both tidal and magnetic effects can be described separately as first-order perturbations to the background metric as

$$g^T_{\alpha\beta} = g^{(0)}_{\alpha\beta} + h^T_{\alpha\beta} \tag{6.1}$$

$$g^B_{\alpha\beta} = g^{(0)}_{\alpha\beta} + h^B_{\alpha\beta} \ . \tag{6.2}$$

However, a second-order perturbative analysis is required to capture the coupling between these two effects. The perturbed metric then reads

$$g^{TB}_{\alpha\beta} = g^{(0)}_{\alpha\beta} + h^T_{\alpha\beta} + h^B_{\alpha\beta} + h^{TB}_{\alpha\beta} \ , \tag{6.3}$$

where $h^{TB}_{\alpha\beta}$ is the second-order perturbation coupling magnetic and tidal effects. In this way, it is possible to assess how the tidal deformability parameter varies in the presence of a magnetic field compared to the non-magnetised case.

In Zhu et al. (2020), the first-order tidal perturbation is defined as

$$h^T_{\alpha\beta} = \begin{pmatrix} -e^{\nu}H_0(r) & 0 & 0 & 0 \\ 0 & e^{\lambda}H_2(r) & 0 & 0 \\ 0 & 0 & r^2K(r) & 0 \\ 0 & 0 & 0 & r^2\sin^2\theta K(r) \end{pmatrix} P_2(\cos\theta) \ , \tag{6.4}$$

according to the formalism developed in Hinderer (2008). The first-order magnetic perturbation reads

$$\begin{aligned} h^B_{\alpha\beta} = \mathrm{diag}(&-2e^{\nu}(h^B_0 + h^B_2 P_2(\cos\theta)),\ 2e^{2\lambda}(m^B_0 + m^B_2 P_2(\cos\theta))/r, \\ &2r^2 k^B_2 P_2(\cos\theta),\ 2r^2\sin^2\theta\ k^B_2 P_2(\cos\theta)\ )\ , \end{aligned} \tag{6.5}$$

where the metric functions $h^B_0(r)$, $h^B_2(r)$, $m^B_0(r)$, $m^B_2(r)$ and $k^B_2(r)$ are obtained by solving Einstein equations together with the conservation equations for the stress-energy tensor $T^{\mu\nu}$ coupled to the Maxwell equations in their covariant formulation

$$\nabla_\nu T^{\mu\nu} = 0 \qquad\qquad \nabla_\nu F^{\mu\nu} = 4\pi J^\mu \quad . \tag{6.6}$$

This formalism for the magnetic perturbation treatment is in agreement with Konno et al. (1999), a work that examined the effects of magnetic fields on the NS structure. By extending the perturbative analysis to second order in the perturbation functions, an analytical form for the second-order perturbation $h^{TB}_{\alpha\beta}$ is derived.

The model in Konno et al. (1999) provides a solid foundation for incorporating magnetic fields into the perturbative analysis. However, it is important to point out that the magnetic field is assumed to be purely poloidal. While this assumption is mathematically tractable due to the preservation of spacetime circularity, it fails to capture the complex magnetic field topologies observed in real NSs.

In reality, evidence suggests that purely poloidal and purely toroidal magnetic fields are unstable. Therefore, any long-lived magnetic field configuration in a NS must necessarily feature a combination of both poloidal and toroidal components. Observations and numerical simulations support this, indicating that realistic magnetic field configurations typically exhibit a mixed poloidal-toroidal structure Braithwaite & Spruit (2004).

In light of these considerations, there are two approaches one can take when implementing the perturbations in the computational framework. The first is to follow the assumption of a purely poloidal magnetic field, as described in Konno et al. (1999), and use this simplified configuration to directly compare the simulation results with theoretical predictions. This approach would provide insights into the effects of a simplified magnetic field topology on the NS tidal deformability. However, the real advantage of numerical simulations lies in their ability to accommodate more complex, realistic configurations, such as mixed poloidal-toroidal magnetic fields, which are analytically intractable. By simulating a NS with such a magnetic field configuration, one can observe the deviations in tidal deformability and other structural properties compared to the results obtained from the simpler poloidal assumption. This would allow for a more comprehensive understanding of the role of magnetic fields in shaping the NS response to tidal forces, offering valuable insights that cannot be captured by purely analytical approaches.

Rotation

Another important aspect to consider for future developments of the inclusion of NS rotation, which is neglected in the present work. Rotation plays a significant role in modifying the tidal deformability of a NS, introducing an additional class of quantities known as rotational tidal Love numbers, which describe the influence of the star's spin on its tidal response.

The impact of spin on tidal deformability was first quantified by Pani et al. (2015), who explicitly computed the rotational Love numbers for a slowly rotating NS. Their study revealed that spin-tidal couplings can introduce substantial corrections to the static tidal deformability, with relative deviations that can exceed 10% compared to the non-rotating case. This effect becomes increasingly relevant for rapidly rotating NSs, where the influence of rotation significantly alters the stellar structure and its tidal response.

From a numerical standpoint, the effect of rotation can be readily incorporated within the framework developed in this work, as both `XNS` and `Gmunu` support simulations of spinning NSs. These codes provide flexible control over the rotation profile, allowing for both uniform rotation, where the angular velocity is constant throughout the star, and differential rotation, where different regions of the NS rotate at different rates. Implementing rotation in this context primarily involves configuring the relevant user parameters, generating the corresponding equilibrium model, and initializing the hydrodynamic evolution accordingly.

The main challenge lies in the extension of the theoretical formalism proposed in this work. Incorporating rotation in the study of tidal deformability requires a complete reformulation of the perturbative framework, as the coupling between spin and tidal fields leads to an extended set of spin-induced tidal Love numbers. These involve complex couplings between different multipole moments that must be treated consistently within a rotational perturbation scheme.

Despite these theoretical complications, extending the simulations to include rotation is a promising next step. The inclusion of rotation in future simulations would significantly broaden the scope of the current work, allowing for a more comprehensive understanding of tidal deformation in rotating NSs and improving the predictive power of simulations in realistic astrophysical environments.

Equation of state

A further potential improvement to the current work involves the use of more complex and physically realistic EOS for the initialization of NSs in the numerical simulations. In fact, although the polytropic assumption employed in this study provides a reasonable approximation of the EOS, it is by nature a simplified model. This simplification makes it an ideal choice for analytical computations, but does not allow to characterise the complex behaviour of NS matter in the stratified internal structure typical of NSs.

Theoretical work has shown that different EOS models can lead to significant differences in the predicted mass-radius relationship. Consequently, the EOS determines the compressibility of the star and how it responds to external tidal fields. The ability to test various EOS models within the same simulation framework presents a unique opportunity to explore a wide range of astrophysical scenarios, and could help identify key signatures to constrain the NS EOS from GW observations.

Numerical codes like `XNS` and `Gmunu` offer the required flexibility by supporting the use of tabulated EOS, that can be directly incorporated into the model. These EOS can account for various phenomena, including the presence of phase transitions (e.g., from hadronic to quark matter) at high densities. Incorporating such detailed models could provide a more accurate description of the NS internal structure, particularly at extremely high densities, where the polytropic approximation fails to represent the true EOS realistically.

In conclusion, the mentioned improvements would enhance the accuracy of the model and broaden its applicability, making it a powerful tool for investigating tidal interactions in more general and realistic astrophysical environments.

ACKNOWLEDGEMENTS

I would like to sincerely thank Professor Tanja Hinderer from Utrecht University for her valuable feedback on the results I obtained building upon her foundational work. My heartfelt gratitude extends to Patrick Chi-Kit Cheong from the University of California, Berkeley, who is one of the principal developers of the `Gmunu` code, and Anson Ka Long Yip from the Chinese University of Hong Kong. Their expertise in numerical relativity was instrumental in guiding me through the development of the computational scheme, especially during my initial encounters with the code's structure. A special and profound thank you is owed to Simon Maenaut from KU Leuven. Simon's generosity with his time and knowledge has been invaluable throughout my thesis journey. When I first started using `Mathematica`, he provided patient support and practical tips that greatly facilitated my learning process. His guidance in metric perturbation theory clarified complex concepts and helped me develop a deeper theoretical understanding. Each discussion with Simon was a source of inspiration and clarity, offering valuable perspectives and concrete suggestions that helped me overcome obstacles and advance my work with renewed confidence and motivation. Beyond his mentorship, I am deeply grateful for his meticulous review of sections of this thesis and his constructive suggestions.

Appendix A

TOLMAN-OPPENHEIMER-VOLKOFF EQUATIONS

The line element describing a static, spherically symmetric spacetime can be written in its most general form as

$$\begin{aligned} ds^2 &= g_{\alpha\beta}\; dx^\alpha dx^\beta && \text{(A.1)} \\ &= -e^\nu dt^2 + e^\lambda dr^2 + r^2 d\theta^2 + r^2 \sin^2\theta d\phi^2 \ , && \text{(A.2)} \end{aligned}$$

where $\nu \equiv \nu(r)$ and $\lambda \equiv \lambda(r)$ are the metric functions. The non-vanishing Christoffel symbols associated to the corresponding metric $g_{\mu\nu}$ can be easily computed from the definition

$$\Gamma^\sigma_{\alpha\beta} := \frac{1}{2} g^{\sigma\lambda}(\partial_\alpha g_{\lambda\beta} + \partial_\beta g_{\alpha\lambda} - \partial_\lambda g_{\alpha\beta}) \tag{A.3}$$

and take the form

$$\begin{aligned} \Gamma^t_{tr} &= \Gamma^t_{rt} = \frac{1}{2}\nu' \\ \Gamma^r_{tt} &= \frac{1}{2} e^{(\nu-\lambda)}\nu' \\ \Gamma^r_{rr} &= \frac{1}{2}\lambda' \\ \Gamma^r_{\theta\theta} &= -e^{-\lambda} r \\ \Gamma^r_{\phi\phi} &= -e^{-\lambda} r \sin^2\theta \\ \Gamma^\theta_{r\theta} &= \Gamma^\theta_{\theta r} = \Gamma^\phi_{r\phi} = \Gamma^\phi_{\phi r} = \frac{1}{r} \\ \Gamma^\theta_{\phi\phi} &= -\cos\theta \sin\theta \\ \Gamma^\phi_{\theta\phi} &= \Gamma^\phi_{\phi\theta} = \cot\theta \ , \end{aligned} \tag{A.4}$$

where primes denote differentiation with respect to r.
Under the assumption of perfect fluid, the stress-energy-momentum tensor $T_{\alpha\beta}$ is defined as

$$T_{\alpha\beta} = (p + \rho) u_\alpha u_\beta + p g_{\alpha\beta} \ , \tag{A.5}$$

where $u^\alpha = (e^{-\nu/2}, 0, 0, 0)$ is the four-velocity of the fluid while p and ρ are the pressure and the density of the fluid respectively. It is convenient to express the stress-energy tensor in the mixed tensor form, so that its non-vanishing components become

$$T_0^0 = -\rho \qquad T_i^i = p \quad . \tag{A.6}$$

Einstein field equations in the mixed form read

$$G^\alpha_\beta = 8\pi T^\alpha_\beta \ . \tag{A.7}$$

Solving the tt component of Equation (A.7) one obtains

$$8\pi\rho = \frac{1}{r^2} + e^{-\lambda}\left(\frac{\lambda'}{r} - \frac{1}{r^2}\right) \tag{A.8}$$

while from the rr component one obtains

$$8\pi p = -\frac{1}{r^2} + e^{-\lambda}\left(\frac{\nu'}{r} + \frac{1}{r^2}\right) \ . \tag{A.9}$$

By equating $G^r_r = G^\theta_\theta = 8\pi p$ and multiplying both sides by $2/r$ one gets

$$\frac{2}{r^3} - \frac{2e^{-\lambda}}{r^3} - \frac{e^{-\lambda}\lambda'}{r^2} - \frac{e^{-\lambda}\nu'}{r^2} - \frac{e^{-\lambda}\lambda'\,\nu'}{2r} + \frac{e^{-\lambda}\nu'^{\,2}}{2r} + \frac{e^{-\lambda}\nu''}{r} = 0 \ . \tag{A.10}$$

Differentiating Equation (A.9) with respect to r yields an expression for the pressure gradient

$$8\pi\frac{dp}{dr} = \frac{2}{r^3} - \frac{2e^{-\lambda}}{r^3} - \frac{e^{-\lambda}\lambda'}{r^2} - \frac{e^{-\lambda}\nu'}{r^2} - \frac{e^{-\lambda}\lambda'\,\nu'}{r} + \frac{e^{-\lambda}\nu''}{r} \tag{A.11}$$

and plugging Equation (A.11) into Equation (A.10) gives

$$8\pi\frac{dp}{dr} = -\frac{e^{-\lambda}\nu'}{2r}(\lambda' + \nu') \ . \tag{A.12}$$

The right-hand side in Equation (A.12) can be rewritten noticing that

$$\frac{e^{-\lambda}\nu'}{2r}(\lambda' + \nu') = \left(-G^t_t + G^r_r\right)\frac{\nu'}{2} = 8\pi(\rho + p)\frac{\nu'}{2} \ , \tag{A.13}$$

therefore

$$\frac{dp}{dr} = -(\rho + p)\frac{\nu'}{2} \quad \Rightarrow \quad \nu' = -\frac{2}{p+\rho}\frac{dp}{dr} \ . \tag{A.14}$$

Let's now introduce the mass function $m(r)$, representing the total mass contained inside a shell of radius r

$$\frac{dm}{dr} = 4\pi r^2\rho \quad \Rightarrow \quad m(r) = \int_0^r 4\pi r^2 \rho \; dr \ . \tag{A.15}$$

Equation (A.8) can be rewritten as

$$\begin{aligned} 8\pi\rho &= \frac{1}{r^2}\left(1 - \frac{d}{dr}(re^{-\lambda})\right) \\ 8\pi r^2\rho &= 1 - \frac{d}{dr}(re^{-\lambda}) \\ \Rightarrow 4\pi r^2\rho &= \frac{1}{2} - \frac{1}{2}\frac{d}{dr}(re^{-\lambda}) \end{aligned} \tag{A.16}$$

and now integrating Equation (A.16) from the centre outwards yields

$$\int_0^r 4\pi r^2 \rho \, dr = \frac{1}{2} r - \frac{1}{2} r e^{-\lambda} \tag{A.17}$$

$$\Rightarrow m(r) = \frac{1}{2} r (1 - e^{-\lambda}) \; , \quad \text{which means} \;\; e^{-\lambda} = 1 - 2m/r \; . \tag{A.18}$$

In Equation (A.9) it is now possible to replace $e^{-\lambda}$ with it expression from Equation (A.18) and ν' with its expression from Equation (A.14) to eventually obtain

$$\frac{dp}{dr} = -(p + \rho) \frac{4\pi r^3 p + m}{r(r - 2m)} \; . \tag{A.19}$$

In conclusion, the system of Tolman-Oppenheimer-Volkoff equations can be constructed as

$$\frac{dm}{dr} = 4\pi r^2 \rho \tag{A.20}$$

$$\frac{dp}{dr} = -(p + \rho) \frac{4\pi r^3 p + m}{r(r - 2m)} \tag{A.21}$$

$$\frac{d\nu}{dr} = -\frac{2}{p + \rho} \frac{dp}{dr} \; . \tag{A.22}$$

The TOV equations (A.20), (A.21) and (A.22) coupled with an equation of state relating the pressure p to the density ρ determine the mechanical equilibrium of the matter distribution.

Appendix B

`XNS` parameters

This appendix contains a list of some of the main user parameters in `XNS`. The values they are assigned in this work to compute the equilibrium stellar model are presented in Table B.1. The numerical values associated with the fluid variables and the metric variables that describe the output equilibrium stellar model are listed in Table B.2.

- `STRETCH` - logical flag that controls the stretching of the grid. If set to `TRUE`, the radial grid is regular up to `RREG` with `NRREG` grid points, then it is stretched from `RREG` to `RMAXSTR` with `NR - NRREG` grid points.
- `NR` - number of points in the radial grid. Since the radial grid is stretched in this case, it is defined from $r =$ `RMIN` to $r =$ `RMAXSTR`. Because of the specific boundary conditions implemented in the metric solver, the lower boundary in the radial direction must always be set to `RMIN=0`.
- `NTH` - number of points in the angular grid, which is defined between $\theta = 0$ and $\theta = \pi$.
- `NRREG` - number of points for the regular grid if the grid is stretched.
- `RMAXSTR` - upper boundary of the radial grid in the case of grid stretching.
- `RREG` - maximum radius of the regular grid.
- `EOSINT` - logical flag to set the equation of state. If `TRUE`, a tabulated EOS is used, that needs to be specified in the `FILEEOS` file. If `FALSE`, a polytropic EOS is used.
- `K1` - polytropic coefficient K of the polytropic EOS.
- `GAMMA` - adiabatic index Γ of the polytropic EOS.
- `RHOINI` - central density for the starting guess.
- `GR` - logical flag related to the underlying gravitational theory. If `TRUE` the solution is computed in the framework of general relativity.
- `DIFFERENTIAL` - logical flag for the star's rotation. If `TRUE`, the model is differentially rotating. If `FALSE`, the model is uniformly rotating with angular velocity `OMG`.

- `OMG` - angular velocity for uniform rotation.
- `IMAG` - logical flag that specifies whether the model is magnetised (if set to `TRUE`) or not (if set to `FALSE`).

Grid parameters	EOS/fluid parameters	Other flags
`STRETCH = TRUE`	`EOSINT = FALSE`	`GR = TRUE`
`NR = 900`	`K1 = 110.0`	`DIFFERENTIAL = FALSE`
`NTH = 100`	`GAMMA = 2.0`	`OMG = 0.0`
`NRREG = 600`	`RHOINI = 1.37E-03`	`IMAG = FALSE`
`RMAXSTR = 100`		
`RREG = 13`		

Table B.1: Values associated to some of the main user parameters for the generation of the equilibrium stellar model with `XNS`.

Fluid variables	Metric variables
$\rho_{max} = 8.47 \times 10^{14}$ g cm^{-3}	$\alpha_{min} = 0.635$
$p_{max} = 1.27 \times 10^{14}$ g cm^{-3}	$\psi_{max} = 1.22$
$v_{\phi,max} = 0.00$	$\beta_{min} = 0.00$

Table B.2: Numerical results for the hydrodynamic and metric variables describing the output equilibrium configuration for the neutron star simulated with `XNS` using the parameter values specified in Table B.1.

Appendix C

SIMULATION RESULTS

This appendix contains the density contour plots generated from the GRHD simulation of a tidally perturbed unmagnetised, non-rotating NS, initialised as described in Section 4.4. The perturbed results are systematically compared to the density contour plots generated by a similarly initialised unperturbed simulation.

These plots illustrate snapshots of the star's internal structure during its evolution throughout the numerical simulation, at times t = 0.0 s, 2.0 ms, 4.0 ms, 5.9 ms, 7.9 ms, and 9.9 ms

The density plots are presented as follows: Figure C.1 and Figure C.2 illustrate the $x - y$ section of the NS together with the density contours; Figures C.3 and C.4 show the density contours on the $x - z$ section of the NS; Figure C.5 and Figure C.6 represent show the density contours on the $y - z$ section of the NS. In all figures, the panels on the left column (panels (a), (c), and (e)) refer to the unperturbed simulation, while the panels on the right column (panels (b), (d), and (f)) refer to the tidally perturbed case. For each series along the different NS sections, the time evolution of the simulation can be read along the vertical sequence throughout each column. Such a disposition in the presentation of the results has been chosen to facilitate the eye comparison between the perturbed and the unperturbed case.

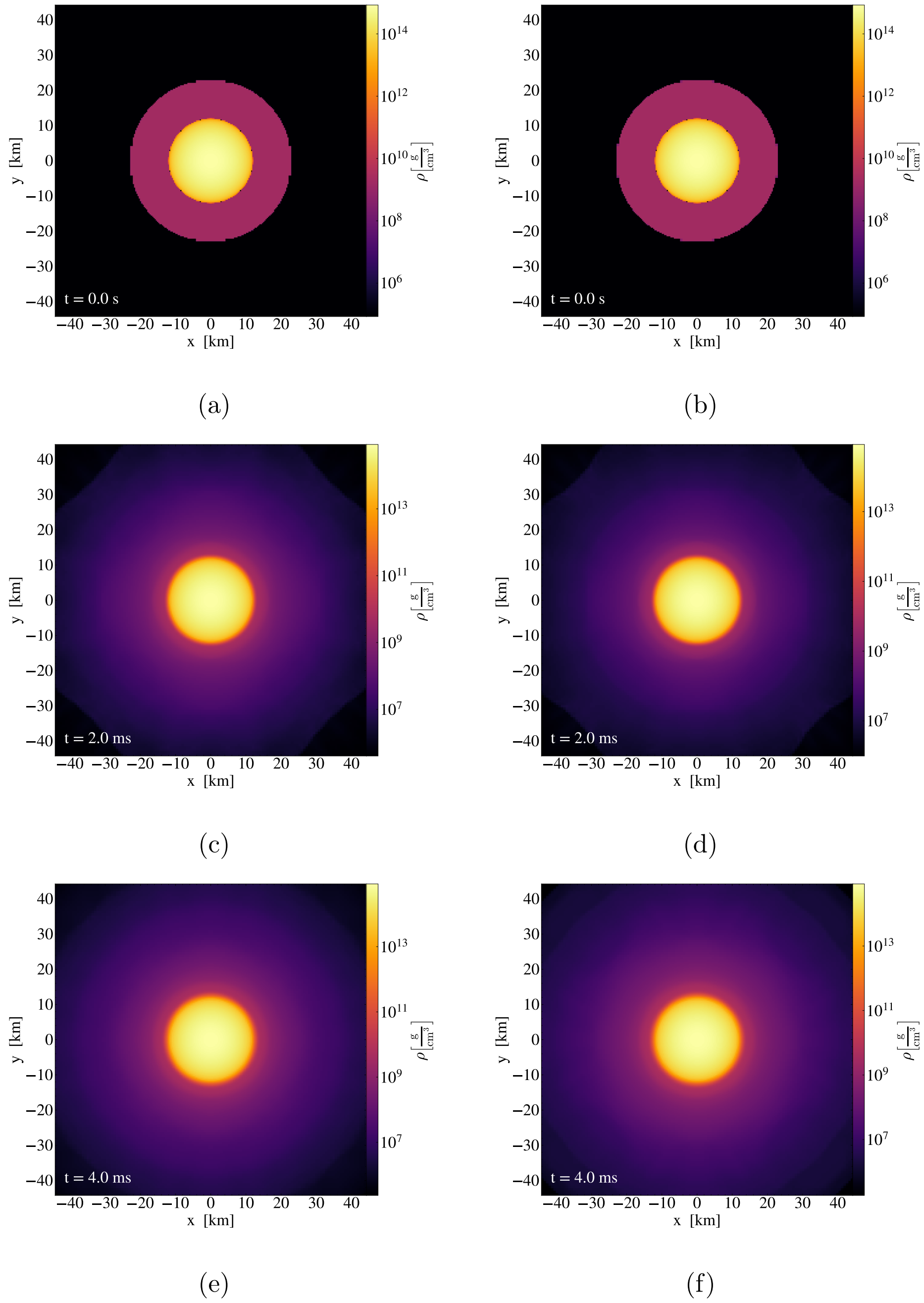

(a) (b)

(c) (d)

(e) (f)

Figure C.1: Section of the neutron star along the $x - y$ plane together with the density contours and the velocity streamlines. Panels (a), (c) and (e): plots obtained from the unperturbed simulation at times t = 0.0 s, 2.0 ms and 4.0 ms respectively. Panels (b), (d) and (f): plots obtained from the perturbed simulation at times t = 0.0 s, 2.0 ms and 4.0 respectively. The observed diffusion of matter around the NS can be ascribed to thermal effects. In the $x - y$ plane, the perturbation does not affect significantly the density distribution around the NS.

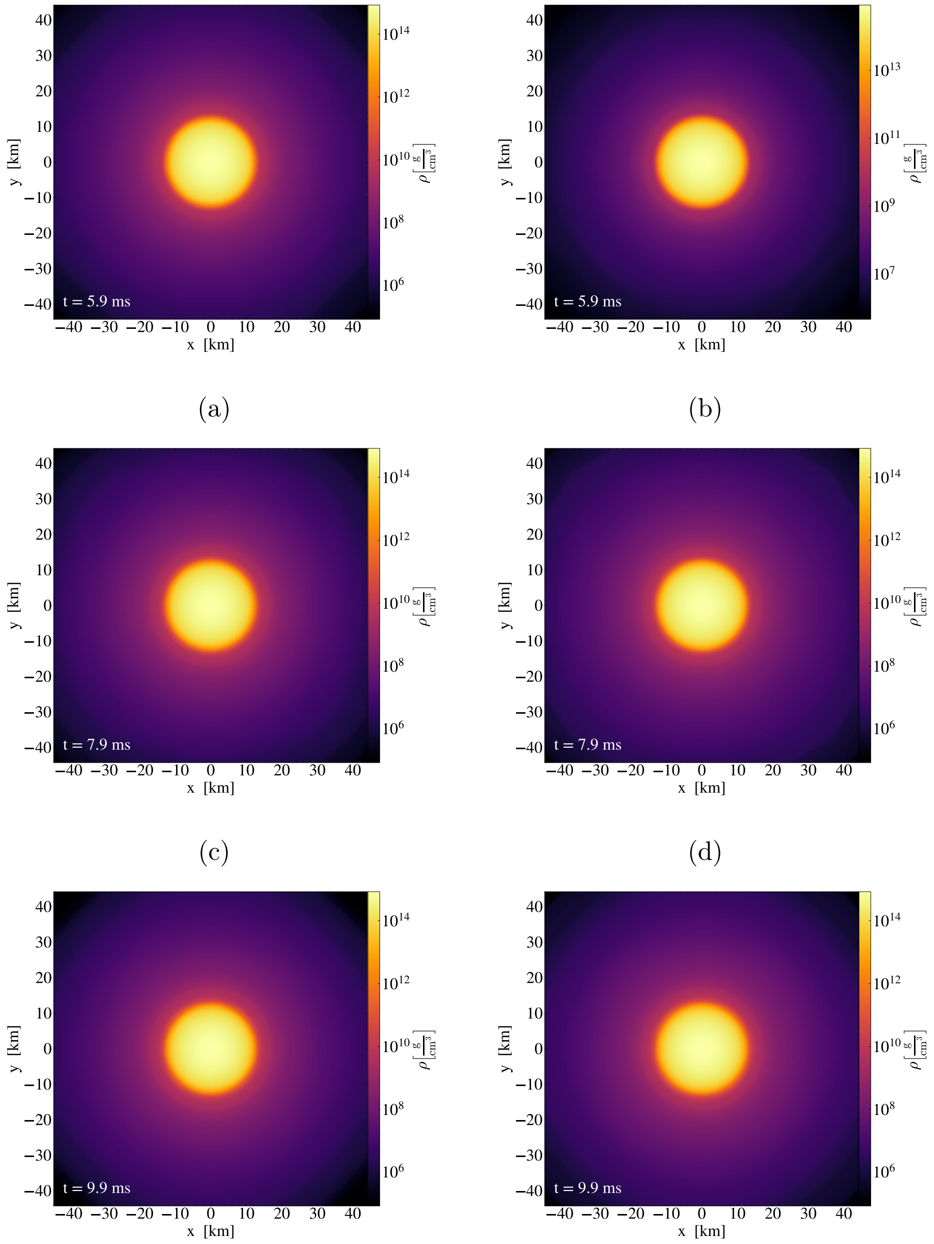

(a) (b)

(c) (d)

(e) (f)

Figure C.2: Section of the neutron star along the $x - y$ plane together with the density contours and the velocity streamlines. Panels (a), (c) and (e): plots obtained from the unperturbed simulation at times t = 5.9 ms, 7.9 ms and 9.9 ms respectively. Panels (b), (d) and (f): plots obtained from the perturbed simulation at times t = 5.9 ms, 7.9 ms and 9.9 ms respectively. The observed diffusion of matter around the NS can be ascribed to thermal effects. In the $x - y$ plane, the perturbation does not affect significantly the density distribution around the NS.

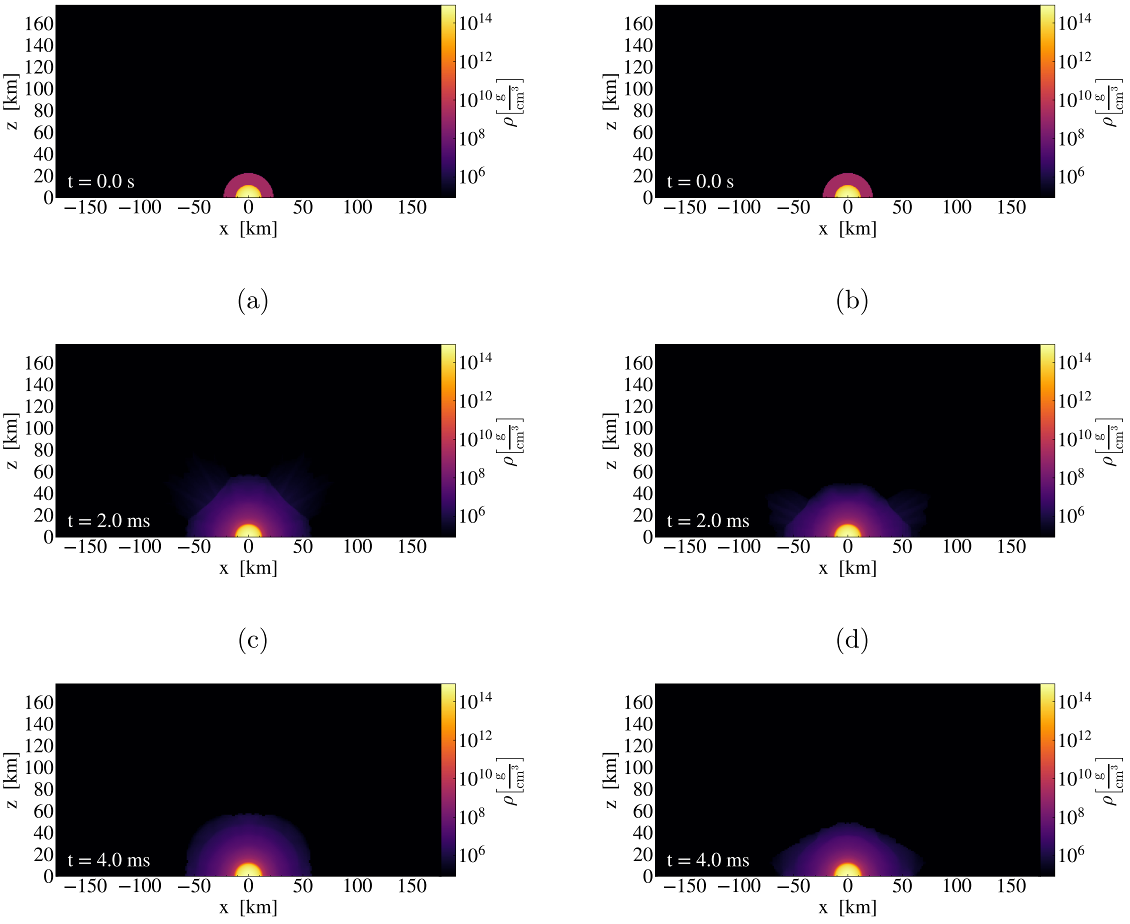

(a) (b)

(c) (d)

(e) (f)

Figure C.3: Section of the neutron star along the $x - z$ plane together with the density contours and the velocity streamlines. Panels (a), (c) and (e): plots obtained from the unperturbed simulation at times t = 0.0 s, 2.0 ms and 4.0 ms respectively. Panels (b), (d) and (f): plots obtained from the perturbed simulation at times t = 0.0 s, 2.0 ms and 4.0 respectively. The observed diffusion of matter around the NS can be ascribed to thermal effects. As the simulation evolves, the perturbed profile shows a contraction along the z direction and the configuration relaxes to an oblate shape, while the unperturbed model maintains spherical symmetry.

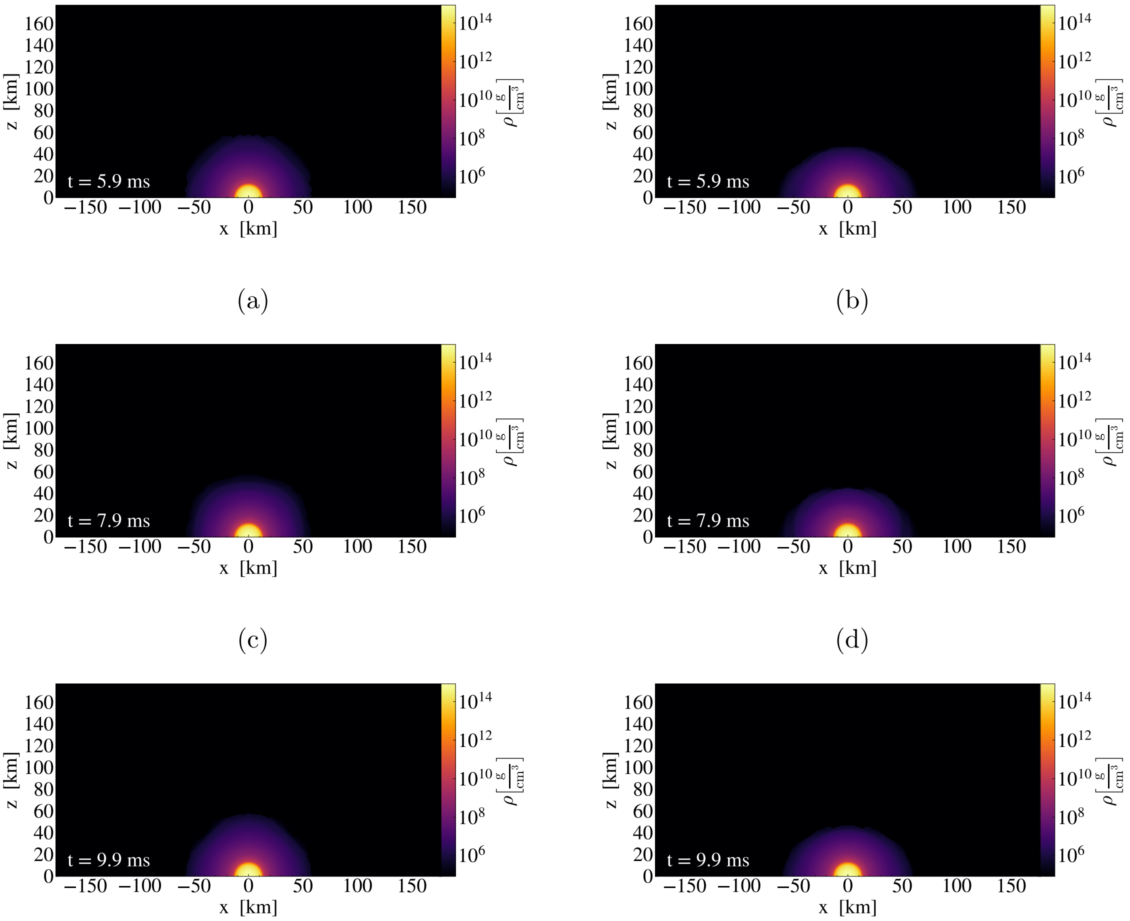

(a) (b)

(c) (d)

(e) (f)

Figure C.4: Section of the neutron star along the $x - z$ plane together with the density contours and the velocity streamlines. Panels (a), (c) and (e): plots obtained from the unperturbed simulation at times t = 5.9 ms, 7.9 ms and 9.9 ms respectively. Panels (b), (d) and (f): plots obtained from the perturbed simulation at times t = 5.9 ms, 7.9 ms and 9.9 ms respectively. The observed diffusion of matter around the NS can be ascribed to thermal effects. As the simulation evolves, the perturbed profile shows a contraction along the z direction and the configuration relaxes to an oblate shape, while the unperturbed model maintains spherical symmetry.

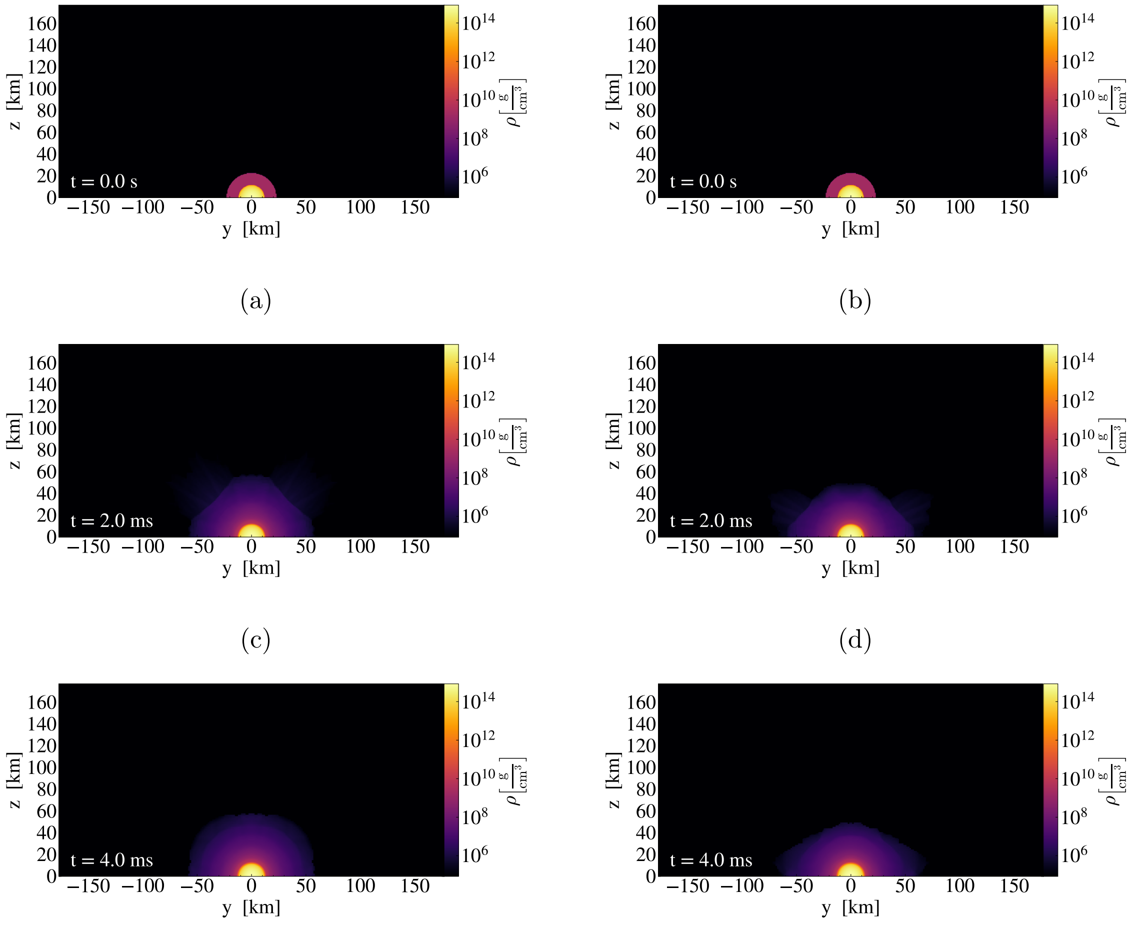

(a) (b)

(c) (d)

(e) (f)

Figure C.5: Section of the neutron star along the $y - z$ plane together with the density contours and the velocity streamlines. Panels (a), (c) and (e): plots obtained from the unperturbed simulation at times t = 0.0 s, 2.0 ms and 4.0 ms respectively. Panels (b), (d) and (f): plots obtained from the perturbed simulation at times t = 0.0 s, 2.0 ms and 4.0 respectively. The observed diffusion of matter around the NS can be ascribed to thermal effects. As the simulation evolves, the perturbed profile shows a contraction along the z direction and the configuration relaxes to an oblate shape, while the unperturbed model maintains spherical symmetry.

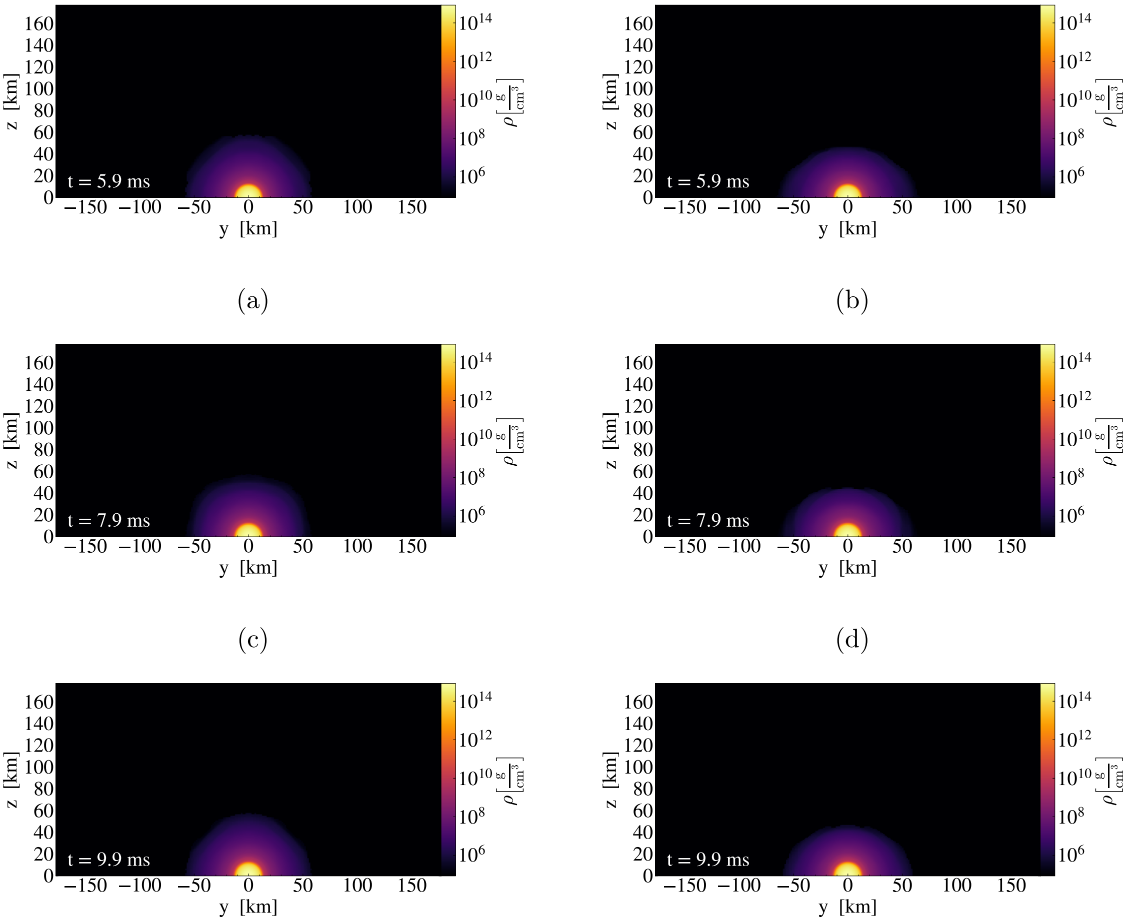

(a) (b)

(c) (d)

(e) (f)

Figure C.6: Section of the neutron star along the $y - z$ plane together with the density contours and the velocity streamlines. Panels (a), (c) and (e): plots obtained from the unperturbed simulation at times t = 5.9 ms, 7.9 ms and 9.9 ms respectively. Panels (b), (d) and (f): plots obtained from the perturbed simulation at times t = 5.9 ms, 7.9 ms and 9.9 ms respectively. The observed diffusion of matter around the NS can be ascribed to thermal effects. As the simulation evolves, the perturbed profile shows a contraction along the z direction and the configuration relaxes to an oblate shape, while the unperturbed model maintains spherical symmetry.

Bibliography

Abac, A., Dietrich, T., Buonanno, A., Steinhoff, J., & Ujevic, M. 2024, *Physical Review D*, 109

Abbott, B., Abbott, R., Abbott, T., et al. 2017, *Physical Review Letters*, 119

Abdikamalov, E. B., Dimmelmeier, H., Rezzolla, L., & Miller, J. C. 2009, *Monthly Notices of the Royal Astronomical Society*, 392, 52–76

Abramowitz, M. & Stegun, I. A. 1964, Handbook of Mathematical Functions With Formulas, Graphs, and Mathematical Tables, National Bureau of Standards

Annala, E., Gorda, T., Kurkela, A., & Vuorinen, A. 2018, *Physical Review Letters*, 120

Baade, W. & Zwicky, F. 1934, *Phys. Rev.*, 46, 76

Baiotti, L., Giacomazzo, B., & Rezzolla, L. 2008, *Phys. Rev. D*, 78, 084033

Bauswein, A., Janka, H.-T., & Oechslin, R. 2010, *Physical Review D*, 82

Baym, G., Hatsuda, T., Kojo, T., et al. 2018, *Reports on Progress in Physics*, 81, 056902

Blanchet, L. 2024, Post-Newtonian Theory for Gravitational Waves

Braithwaite, J. & Spruit, H. C. 2004, *Nature*, 431

Brillet, A. & Giazotto, A. e. a. 1989, Technical report VIR-0517B-15, Tech. rep., Virgo Collaboration

Bucciantini, N. & Del Zanna, L. 2011, *Astronomy amp; Astrophysics*, 528, A101

Bucciantini, N., Pili, A. G., & Zanna, L. D. 2014, Solving the 3+1 GRMHD equations in the eXtended Conformally Flat Condition: the XNS code for magnetized neutron stars

Chadwick, J. 1932, *Nature*, 129

Chamel, N. & Haensel, P. 2008, *Living Reviews in Relativity*, 11

Chandrasekhar, S. 1939, An introduction to the study of stellar structure, University of Chicago Press

Chatziioannou, K. 2020, *General Relativity and Gravitation*, 52

Cheong, P. C.-K., Lam, A. T.-L., Ng, H. H.-Y., & Li, T. G. F. 2021, *Monthly Notices of the Royal Astronomical Society*, 508, 2279–2301

Cheong, P. C.-K., Lin, L.-M., & Li, T. G. F. 2020, *Classical and Quantum Gravity*, 37, 145015

Cordero-Carrión, I., Cerdá-Durán, P., Dimmelmeier, H., et al. 2009, *Physical Review D*, 79

Damour, T. & Nagar, A. 2009, *Physical Review D*, 80

Del Zanna, L., Zanotti, O., Bucciantini, N., & Londrillo, P. 2007, *Astronomy amp; Astrophysics*, 473, 11–30

Dietrich, T., Bernuzzi, S., & Tichy, W. 2017, *Phys. Rev. D*, 96, 121501

Dietrich, T., Hinderer, T., & Samajdar, A. 2021, *General Relativity and Gravitation*

Dietrich, T., Khan, S., Dudi, R., et al. 2019a, *Physical Review D*, 99

Dietrich, T., Samajdar, A., Khan, S., et al. 2019b, *Physical Review D*, 100

Dimmelmeier, H., Font, J. A., & Müller, E. 2001, *The Astrophysical Journal*, 560, L163–L166

Duncan, R. C. & Thompson, C. 1992, *ApJ*, 392, L9

Favata, M. 2014, *Physical Review Letters*, 112

Fortin, M., Providência, C., Raduta, A. R., et al. 2016, *Phys. Rev. C*, 94, 035804

Gourgoulhon, E. 2007, 3+1 Formalism and Bases of Numerical Relativity

Hawking, S. W. & Israel, W. 1987, Three hundred years of gravitation

Hewish, A., Bell, S. J., Pilkington, J. D. H., Scott, P. F., & Collins, R. A. 1968, *Nature*, 217

Hild, S., Abernathy, M., Acernese, F., et al. 2011, *Classical and Quantum Gravity*, 28, 094013

Hinderer, T. 2008, *The Astrophysical Journal*, 677, 1216–1220

Hinderer, T., Lackey, B. D., Lang, R. N., & Read, J. S. 2010, *Physical Review D*, 81

Katagiri, T., Yagi, K., & Cardoso, V. 2024, On relativistic dynamical tides: subtleties and calibration

Kippenhahn, R., Weiss, A., & Weigert, A. c2012, Stellar structure and evolution / Rudolf Kippenhahn, Alfred Weigert, Achim Weiss, 2nd edn., Springer

Kiuchi, K. 2024, General relativistic magnetohydrodynamics simulations for binary neutron star mergers

Konno, K., Obata, T., & Kojima, Y. 1999, Deformation of relativistic magnetized stars

Lattimer, J. & Prakash, M. 2007, *Physics Reports*, 442, 109–165

Lattimer, J. M. & Prakash, M. 2001, *The Astrophysical Journal*, 550, 426–442

Maggiore, M. 2007, Gravitational Waves: Volume 1: Theory and Experiments, Oxford University Press

Miller, M. C., Lamb, F. K., Dittmann, A. J., et al. 2019, *The Astrophysical Journal Letters*, 887, L24

Miravet-Tenés, M., Guerra, D., Ruiz, M., Cerdá-Durán, P., & Font, J. A. 2025, *Physical Review D*, 111

Oertel, M., Hempel, M., Klähn, T., & Typel, S. 2017, *Rev. Mod. Phys.*, 89, 015007

Oppenheimer, J. R. & Volkoff, G. M. 1939, *Phys. Rev.*, 55, 374

Pani, P., Gualtieri, L., & Ferrari, V. 2015, *Physical Review D*, 92

Pellouin, C., Dvorkin, I., & Lehoucq, L. 2025, *Astronomy amp; Astrophysics*, 693, A283

Perot, L., Chamel, N., & Sourie, A. 2020, *Physical Review C*, 101

Peters, P. C. 1964, *Phys. Rev.*, 136, B1224

Peters, P. C. & Mathews, J. 1963, *Phys. Rev.*, 131, 435

Pili, A. G., Bucciantini, N., & Del Zanna, L. 2014, *Monthly Notices of the Royal Astronomical Society*, 439, 3541–3563

Pili, A. G., Bucciantini, N., & Del Zanna, L. 2017a, *Monthly Notices of the Royal Astronomical Society*, 470, 2469–2493

Pili, A. G., Bucciantini, N., & Del Zanna, L. 2017b, *Monthly Notices of the Royal Astronomical Society*, 470, 2469

Raaijmakers, G., Greif, S. K., Hebeler, K., et al. 2021, *The Astrophysical Journal Letters*, 918, L29

Radice, D., Perego, A., Zappa, F., & Bernuzzi, S. 2018, *The Astrophysical Journal Letters*, 852, L29

Regge, T. & Wheeler, J. A. 1957, *Phys. Rev.*, 108, 1063

Riley, T. E., Watts, A. L., Bogdanov, S., et al. 2019, *The Astrophysical Journal Letters*, 887, L21

Romani, R. W., Kandel, D., Filippenko, A. V., Brink, T. G., & Zheng, W. 2022, *The Astrophysical Journal Letters*, 934, L17

Sathyaprakash, B., Abernathy, M., Acernese, F., et al. 2012, Scientific Potential of Einstein Telescope

Shoshany, B. 2021, *Journal of Open Source Software*, 6, 3416

Suleiman, L., Fortin, M., Zdunik, J. L., & Providência, C. 2022, *Physical Review C*, 106

Sumiyoshi, K., Kojo, T., & Furusawa, S. 2023, Equation of State in Neutron Stars and Supernovae (Springer Nature Singapore), 1–51

Tauris, T. M., Kramer, M., Freire, P. C. C., et al. 2017, *ApJ*, 846, 170

Tauris, T. M. & van den Heuvel, E. P. J. 2006, in Compact stellar X-ray sources, Vol. 39, 623–665

Thorne, K. S. 1980, *Rev. Mod. Phys.*, 52, 285

Thorne, K. S. 1998, *Physical Review D*, 58

Thorne, K. S. & Campolattaro, A. 1967, Non-Radial Pulsation of General-Relativistic Stellar Models. I. Analytic Analysis for L >= 2

Tolman, R. C. 1939, *Phys. Rev.*, 55, 364

Vigna-Gómez, A., Neijssel, C. J., Stevenson, S., et al. 2018, *MNRAS*, 481, 4009

Walker, K., Smith, R., Thrane, E., & Reardon, D. J. 2024, Precision constraints on the neutron star equation of state with third-generation gravitational-wave observatories

Wilson, J. R. & Mathews, G. J. 2003, Relativistic Numerical Hydrodynamics, Cambridge Monographs on Mathematical Physics, Cambridge University Press

Zhu, Z., Li, A., & Rezzolla, L. 2020, *Physical Review D*, 102

Özel, F. & Freire, P. 2016, *Annual Review of Astronomy and Astrophysics*, 54, 401–440